Efficiency Enhancement Techniques for Free-Electron Lasers

Mak, Alan

2017

Efficiency Enhancement Techniques for Free-Electron Lasers

Alan Mak

Doctoral Thesis
2017

Lund University

EFFICIENCY ENHANCEMENT TECHNIQUES FOR FREE-ELECTRON LASERS

Printed in Sweden by Media-Tryck, Lund, 2017

MAX IV Laboratory
Lund University
P. O. Box 118
SE–221 00 Lund
Sweden

http://www.maxiv.lu.se

ISBN 978-91-7753-305-4 (Printed version)
ISBN 978-91-7753-306-1 (Electronic version)

CONTENTS

Abstract v

Popular science summary vii

Acknowledgements ix

List of publications xi

Additional publications xiii

Abbreviations xv

1 Introduction and motivation 1
- 1.1 Free-electron laser . . . 1
- 1.2 Compare and contrast . . . 2
  - 1.2.1 With conventional laser . . . 2
  - 1.2.2 With electron storage ring . . . 3
- 1.3 Efficiency enhancement . . . 4
- 1.4 Thesis outline . . . 5

2 Basic free-electron laser theory 7
- 2.1 Working principle in a nutshell . . . 7
- 2.2 Coherence and intensity . . . 8
- 2.3 Definition of parameters . . . 10
  - 2.3.1 Radiation . . . 10
  - 2.3.2 Undulator . . . 10
  - 2.3.3 Electrons . . . 11
  - 2.3.4 Other parameters . . . 12
- 2.4 One-dimensional model . . . 13
- 2.5 Resonant energy . . . 14
- 2.6 Simplified equations of motion . . . 14
- 2.7 Phase space trajectories . . . 15
- 2.8 Simplified equations of the optical field . . . 16
- 2.9 Numerical integration . . . 17
- 2.10 Saturation and efficiency . . . 21

3 Undulator tapering 23
- 3.1 What is undulator tapering? . . . 23
- 3.2 Approaches to taper optimization . . . 24
- 3.3 The KMR model . . . 24
- 3.4 Motion around the resonant particle . . . 25
- 3.5 Phase space trajectories . . . 26
- 3.6 Potential well . . . 28
- 3.7 Bucket deceleration . . . 29
- 3.8 Bucket size . . . 29

3.8.1 Bucket width . . . 30
3.8.2 Bucket height . . . 31
3.8.3 Bucket area . . . 31
3.9 Modification to the KMR model . . . 32
3.10 The KMR methods . . . 32
3.11 Departure from the ideal case . . . 33
3.12 Empirical optimization at FLASH2 . . . 34

4 Phase jump method 37
4.1 What is the phase jump method? . . . 37
4.2 Phase definitions . . . 38
4.3 Role of the phase shifter . . . 39
4.3.1 Without the phase shifter . . . 39
4.3.2 With the phase shifter . . . 40
4.4 Analysis of a phase shifter . . . 40
4.5 Overview of the phase jump model . . . 42
4.6 Comparison with undulator tapering . . . 43

5 Summary and outlook 47

References 49

Papers

Comments on the papers 55

I Model-based optimization of tapered free-electron lasers 57

II Further studies of undulator tapering in x-ray FELs 71

III Empirical optimization of undulator tapering at FLASH2 and comparison with numerical simulations 79

IV Phase jump method for efficiency enhancement in free-electron lasers 97

V FEL operation modes of the MAX IV Short Pulse Facility 117

ABSTRACT

The central question addressed in this thesis is how to make the free-electron laser (FEL) more efficient. In recent years, coherent diffraction imaging provides an important motivation for efficiency enhancement. This is because a more efficient FEL process enables converting a larger fraction of the electron beam's power into optical power. By increasing the average optical power to the terawatt level, an x-ray FEL will open the door to single-shot, single-molecule imaging with a sufficiently high signal-to-noise ratio.

This thesis examines two techniques for efficiency enhancement, namely, undulator tapering and the phase jump method.

For undulator tapering, the well-established analytical model by Kroll, Morton and Rosenbluth (KMR) is revisited and modified. With the aid of numerical simulations, it is demonstrated that the modified model results in a further enhancement in FEL efficiency beyond the original model.

For the phase jump method, a new physics model is developed to describe the energy extraction mechanism in the longitudinal phase space. The model reveals the possibility to extract energy from electrons outside the ponderomotive bucket, as well as the potential to increase the spectral purity by suppressing the synchrotron sidebands.

POPULAR SCIENCE SUMMARY

This thesis concerns a special type of laser, known as the free-electron laser (FEL). It produces light of excellent quality, making it useful for a variety of applications in physics, chemistry, biology and medicine. The development of FELs is a part of the long-term strategic plan of the MAX IV Laboratory here in Lund, Sweden.

In this context, the word "light" does not refer exclusively to visible light, whose wavelength ranges from 400 to 700 nanometres (1 nanometre = 1 billionth of a metre). It also includes invisible light, such as microwave, infrared, ultraviolet and x-ray.

An FEL differs from a conventional laser in its working principle. While a conventional laser uses a gas, liquid or crystal as the medium for producing light, an FEL uses a beam of electrons travelling at close to the speed of light. The electron beam is produced by a particle accelerator, and is injected into a magnet device known as the undulator. The undulator can be tens, or even hundreds, of metres long.

As the electrons pass through the undulator, they are deflected by the magnetic field, and are forced to move in a zig-zag path. The zig-zag motion causes the electrons to emit light. Along the undulator, the electrons can interact collectively with the light emitted by themselves such that the light is amplified (i.e. made stronger).

An important merit of the FEL is that its wavelength of operation can be tuned over a wide range, reaching even the x-ray range (around 0.01 to 10 nanometres). In contrast, a conventional laser using a gas, liquid or crystal medium simply cannot reach the x-ray range. As the x-ray wavelength is roughly the size of an atom, an x-ray FEL enables scientists to, for example, probe the atomic structure of viruses and proteins.

Furthermore, the x-ray pulses delivered by an FEL can be as short as 10 femtoseconds (1 femtosecond = 1 quadrillionth of a second), which is roughly the duration of a molecular vibration. This enables scientists to, for example, "film" a chemical reaction.

Other than the FEL, there is currently no light source capable of producing such short and intense x-ray pulses. However, the efficiency of the FEL is typically only about 0.1%. This means that only

one thousandth of the electron beam's power can be converted into the power of the light.

An important goal for the FEL community, therefore, is to overcome this efficiency limit, getting as much light out of the electron beam as possible. To this end, the thesis investigates two techniques for enhancing the FEL efficiency: (i) undulator tapering and (ii) the phase jump method. The thesis aims to improve the understanding of the underlying physics, so that the two techniques can be optimized for the maximum possible FEL efficiency.

ACKNOWLEDGEMENTS

The completion of the doctoral degree is a major milestone in my education. First and foremost, I would like to take this occasion to thank my parents for their love and support throughout the past three decades. In addition, I am grateful to my grandmother, who was an important figure in the earlier years of my life.

Next, I wish to express my gratitude to my thesis supervisors, Sverker Werin and Francesca Curbis, for their guidance during my years as a doctoral student.

I wish to give thanks to the scientists at MAX IV, especially Erik Mansten, Sara Thorin, Simon Leeman and Åke Andersson, for the helpful exchanges of ideas at meetings and seminars. I would also like to thank the members of the MAX IV staff, especially Carolina Ingvander and Elisabeth Dahlström, for their help with all sorts of administrative tasks.

Besides, I wish to thank the colleagues at DESY, especially Bart Faatz, for the good collaboration at the FLASH2 facility, from the beam-based alignment of the machine to the experimental work on undulator tapering.

Finally, I wish to thank my fellow students at MAX IV for their good company on my journey towards the doctoral degree. They include Christian Stråhlman, Galina Skripka, Joel Andersson, Jonas Björklund Svensson, Jonas Breunlin, Mihai Pop, Olivia Karlberg, Teresia Olsson and Walan Grizolli.

LIST OF PUBLICATIONS

This thesis is based on the following papers, which I will refer to by their Roman numerals.

I **Model-based optimization of tapered free-electron lasers**
A. Mak, F. Curbis, S. Werin.
Phys. Rev. ST Accel. Beams **18**, 040702 (2015).

II **Further studies of undulator tapering in x-ray FELs**
A. Mak, F. Curbis, S. Werin.
Proceedings of FEL 2015, Daejeon, Korea, TUP002.

III **Empirical optimization of undulator tapering at FLASH2 and comparison with numerical simulations**
A. Mak, F. Curbis, B. Faatz, S. Werin.
DESY Report 16-168 (2016).

IV **Phase jump method for efficiency enhancement in free-electron lasers**
A. Mak, F. Curbis, S. Werin.
Phys. Rev. Accel. Beams (under 3rd review as of May 2017).

V **FEL operation modes of the MAX IV Short Pulse Facility**
A. Mak, F. Curbis, S. Werin.
Proceedings of FEL 2015, Daejeon, Korea, MOP083.

ADDITIONAL PUBLICATIONS

I am also an author of the following papers, which were published during my time as a doctoral student.

1 **Sensitivity study of a tapered free-electron laser**
A. Mak, F. Curbis, S. Werin.
Proceedings of FEL 2014, Basel, Switzerland, TUP018.

2 **Methods for the optimization of a tapered free-electron laser**
A. Mak, F. Curbis, S. Werin.
Proceedings of IPAC 2014, Dresden, Germany, THPRO023.

3 **Simulation studies for an x-ray FEL based on an extension of the MAX IV linac**
F. Curbis, N. Čutić, O. Karlberg, F. Lindau, A. Mak, E. Mansten, S. Thorin, S. Werin.
Proceedings of FEL 2013, New York, USA, WEPSO07.

4 **The MAX IV linac and first design for an upgrade to 5 GeV to drive an x-ray FEL**
S. Thorin, F. Curbis, N. Čutić, M. Eriksson, O. Karlberg, F. Lindau, A. Mak, E. Mansten, S. Werin.
Proceedings of FEL 2013, New York, USA, TUPSO80.

5 **Extension of the MAX IV linac for a free-electron laser in the x-ray region**
F. Curbis, N. Čutić, S. Werin, O. Karlberg, A. Mak, S. Thorin, E. Mansten, F. Lindau, M. Eriksson.
Proceedings of IPAC 2013, Shanghai, China, TUPEA050.

ABBREVIATIONS

DESY	Deutsches Elektronen-SYnchrotron
FEL	Free-Electron Laser
FLASH	Free-electron LASer in Hamburg
FWHM	Full Width at Half Maximum
GMD	Gas-Monitor Detector
IPAC	International Particle Accelerator Conference
iSASE	Improved Self-Amplified Spontaneous Emission
KMR	Kroll, Morton and Rosenbluth
LCLS	Linac Coherent Light Source
linac	Linear accelerator
MAX	Microtron Accelerator for X-rays
MCP	Micro-Channel Plate
PAL	Pohang Accelerator Laboratory
rms	Root Mean Square
SACLA	SPring-8 Angstrom Compact free-electron LAser
SASE	Self-Amplified Spontaneous Emission
SLAC	Stanford Linear Accelerator Center
SPF	Short Pulse Facility
SPring-8	Super Photon ring – 8 GeV
SVEA	Slowly Varying Envelope Approximation
XFEL	X-ray Free-Electron Laser

CHAPTER 1

INTRODUCTION AND MOTIVATION

1.1 Free-electron laser

The free-electron laser (FEL) is a type of coherent light source. This type of facility uses a relativistic beam of electrons provided by a particle accelerator. The electron beam is made to propagate through a magnetic device known as the undulator. During the propagation, electromagnetic radiation is emitted and amplified. The radiation has a number of distinctive properties:

(i) high power (typically higher than 1 GW),

(ii) short pulse duration (typically shorter than 1 ps),

(iii) tunable wavelength (from infrared to hard x-ray),

(iv) narrow bandwidth ($\Delta\lambda/\lambda \sim 0.1\%$),

(v) good transverse and longitudinal coherence.

These optical properties make the FEL useful for a wide range of applications in condensed matter physics [1], photochemistry [2], structural biology [3], medicine [4] and other research disciplines.

The FEL principle was first conceived by John M. J. Madey [5] at Stanford University in 1971. The theoretical work led to the first experimental demonstration of the FEL amplification [6] in 1976, as well as the first FEL operation [7] in 1977. A full historical account of the development of the FEL is given in Ref. [8].

As of early 2017, examples of FEL facilities in operation are the FLASH in Germany, the LCLS in the United States, and the SACLA in Japan. Meanwhile, examples of FEL facilities under commissioning are the European XFEL in Germany, the Swiss FEL in Switzerland, and the PAL-FEL in South Korea.

The development of x-ray FELs is also in the long-term strategic plan [9] of the MAX IV Laboratory here in Lund, Sweden. According

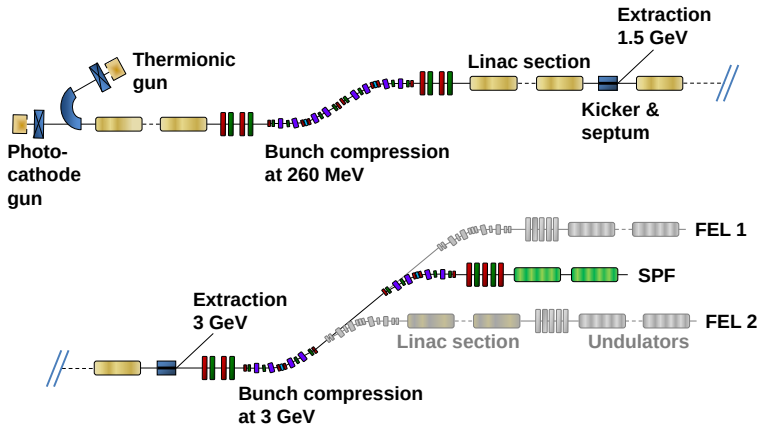

Figure 1.1. *Schematic diagram of the injector at the MAX IV Laboratory. Electrons are extracted at 1.5 GeV and 3 GeV, and injected into two storage rings. The Short Pulse Facility (SPF) situated at the end of the injector is a single-pass, incoherent light source. The total length of the injector is about 300 m. Two potential FELs forseen in the long-term strategic plan of the laboratory are shown in grey.*

to the plan, future FELs at MAX IV can utilize the existing injector. A schematic diagram of the injector is shown in Fig. 1.1.

The injector is capable of delivering an electron energy of 3 GeV. It is used for the top-up of two storage rings operating at 1.5 GeV and 3 GeV. In addition, it provides electron bunches for the Short Pulse Facility (SPF) [10].

The SPF is a single-pass light source. It consists of two undulator modules, each with a length of 5 m. It was designed to produce incoherent x-ray pulses as short as 100 fs.

While the SPF is *not* an FEL, future FELs can be constructed as branch lines parallel to the SPF (shown in grey in Fig. 1.1). Additional linear accelerator (linac) sections can also be installed in the branch lines for higher electron energies.

1.2 Compare and contrast

1.2.1 With conventional laser

The word “laser” is an acronym for “light amplification by stimulated emission of radiation”. As lasers, both the free-electron laser and the conventional laser rely on stimulated emission to amplify the radiation. In both types of light sources, the output radiation is coherent, meaning that the electromagnetic waves maintain a fixed phase relation in time and space.

A major difference between the FEL and the conventional laser is the gain medium. For the conventional laser, the gain medium is a gas, liquid, crystal or semiconductor, in which electrons are bound to atoms or molecules. For the FEL, the gain medium is replaced by a beam of free electrons propagating through a magnetic field in vacuum. The free electrons are free in the sense that they are not bound to atoms or molecules.

In the conventional laser, the wavelength of the output radiation is determined by the transitions of bound electrons between quantum states. As the quantum states have fixed energy levels, there is very little room for altering the radiation wavelength. In the FEL, the wavelength of the output radiation is determined by the electron energy and the undulator parameter, which can generally be adjusted with relative ease. This gives the FEL a higher tunability over the conventional laser. The wavelength range of the FEL spans from the microwave regime to the hard x-ray regime.

Besides, the optical resonator is an essential component of the conventional laser. However, there is a lack of mirrors with sufficient reflectivity in the x-ray regime, making it difficult to construct high-power x-ray conventional lasers. In contrast, a single-pass FEL does not require any optical resonator, thus circumventing the need for mirrors. In other words, the FEL principle makes it possible to construct x-ray lasers with exceedingly high power.

1.2.2 With electron storage ring

While the electron storage ring is a so-called "third-generation" light source, the free-electron laser is a "fourth-generation" one. A major difference is that the FEL has generally got a higher degree of transverse and longitudinal coherence. Furthermore, the FEL offers a higher power, a narrower bandwidth and a shorter pulse duration than the storage ring.

A figure of merit for light sources is the peak brilliance, which is also known as the spectral brightness. It is defined as the number of photons emitted per unit time, per unit area, per unit solid angle, within the spectral bandwidth of 0.1%. Figure 1.2 shows the peak brilliance as a function of photon energy for various FEL and storage ring facilities around the world. In terms of the peak brilliance, the FEL facilities surpass the storage ring facilities by at least five orders of magnitude.

With its excellent optical quality, the FEL opens up the door to new scientific experiments beyond the limits of the storage ring. For instance, the structures of proteins [11] and viruses [12] can be studied at x-ray FEL facilities by means of single-shot coherent diffraction imaging. The short wavelength of the x-ray offers a high spatial resolution. The large number of photons within the short pulse makes it possible to collect enough photons for a diffraction image with only a single pulse before the sample is damaged by radiation.

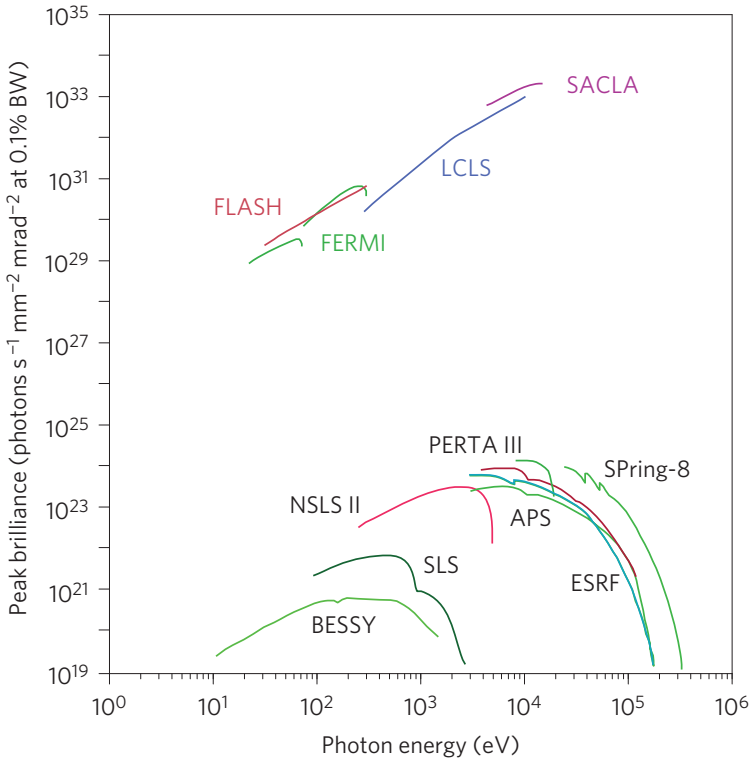

Figure 1.2. *Peak brilliance versus photon energy for a selection of x-ray light sources worldwide. In the plot, FERMI (Italy), FLASH (Germany), LCLS (United States) and SACLA (Japan) are free-electron laser facilities, while all the other ones are storage ring facilities. The figure is adapted from L. B. Fletcher et al., "Ultrabright x-ray laser scattering for dynamic warm dense matter physics", Nature Photonics* ***9****, 274 (2015).*

1.3 Efficiency enhancement

In the FEL process, power is extracted from the injected electron beam, and converted into the power of the output radiation. The FEL efficiency can therefore be defined as

$$\text{Efficiency} = \frac{\text{Power of the output radiation}}{\text{Power of the injected electron beam}}. \tag{1.1}$$

The central theme of this thesis is the enhancement of the FEL efficiency, and there are two main reasons why this is important.

The first reason is an obvious one. Efficiency is a figure of merit for all kinds of machines, and the FEL is no exception. The FEL uses a relativistic electron beam as the gain medium, and it usually requires a large-scale accelerator system (such as the one shown in Fig. 1.1)

to provide such an electron beam. Thus, cost-effectiveness is an important concern. A more efficient FEL process makes it possible to extract more power from the electron beam, thus making better use of the electron beam.

The second reason is the demand by certain experiments conducted at x-ray FEL facilities, such as the single-shot coherent diffraction imaging of single molecules. To improve the quality of the image, these experiments call for a larger number of photons within a shorter x-ray pulse, which translates to a higher average radiation power. According to Eq. (1.1), for a given power of the injected electron beam, a higher average radiation power corresponds to a higher efficiency.

The FEL efficiency is limited by the saturation of the FEL process. At the saturation, the FEL efficiency is typically on the order of 0.1%. In order to enhance the FEL efficiency, we have to overcome this limit. The limit can be overcome by a number of techniques, which sustain the power transfer from the electrons to the radiation beyond the saturation point. In this thesis, we discuss two of such techniques: (i) *undulator tapering* and (ii) the *phase jump method*.

1.4 Thesis outline

The five papers in the last part of this book constitute the core of the thesis, and the preceding chapters provide the necessary background knowledge for the papers.

Chapter 2 introduces basic concepts pertaining to the FEL, and explains the working principle of the FEL up to the saturation point.

Chapter 3 introduces the technique of undulator tapering. It also puts into perspective the research presented in Papers I, II and III.

Chapter 4 introduces the phase jump method. It overviews and supplements the research presented in Paper IV. This chapter concludes by comparing and contrasting the phase jump method with undulator tapering.

Paper V concerns the SPF at the MAX IV Laboratory. While the SPF is not an FEL, the paper explores the possibility to operate the SPF as a simple FEL, so as to utilize the SPF as a test bed for a future full-fledged FEL at MAX IV. The paper also touches on the topic of single-step undulator tapering.

CHAPTER 2

BASIC FREE-ELECTRON LASER THEORY

2.1 Working principle in a nutshell

The main components of a single-pass free-electron laser are the electron beam and the undulator, as shown in Fig. 2.1(a). The electron beam contains bunches of relativistic electrons produced by an electron accelerator. The undulator is an array of permanent dipole magnets with alternating polarity along its length.

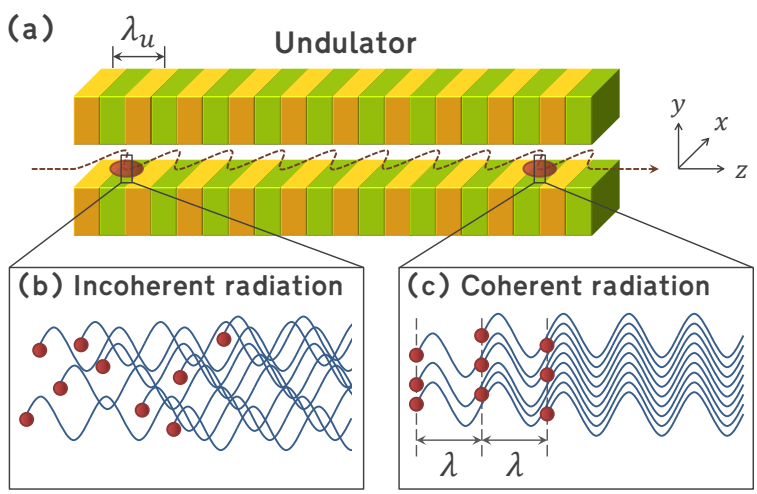

Figure 2.1. *The working principle of a free-electron laser. (a) The electron beam oscillates transversely and radiate, as it propagates down a long undulator. (b) In the first section of the undulator, the random distribution of electrons within a bunch leads to incoherent radiation. (c) In the subsequent section of the undulator, the formation of microbunches within the electron bunch leads to coherent radiation.*

Using the coordinate system in Fig. 2.1(a), the static magnetic field in the undulator is parallel to the y axis, and is periodic along the z axis. The *undulator period* λ_u is typically in the order of a few centimetres.

Upon entering the undulator, the electron beam travels down the z axis, and is deflected repeatedly by the periodic magnetic field. This causes the electrons to oscillate in the x direction, and emit synchrotron radiation at some wavelength λ.

Initially, the electrons are randomly distributed within a bunch, and the optical waves emitted by individual electrons have random phases with respect to one another. This process is known as *spontaneous emission*, and is depicted by Fig. 2.1(b). The resultant radiation is largely *incoherent*, as in an electron storage ring.

However, the undulator of an FEL is typically much longer than that in a storage ring. As the electron bunch continues to travel down the z axis, it can interact collectively with the co-propagating radiation, such that the radiation is significantly amplified.

During the interaction, the electrons in the bunch gradually organize themselves into a series of thin disks along the z axis, as depicted by Fig. 2.1(c). These thin disks, known as *microbunches*, are equally spaced at the optical wavelength λ. The thickness of each thin disk is small compared to λ. The formation of microbunches will be examined in greater detail in Section 2.9.

With the formation of microbunches, the optical waves emitted by individual electrons are correlated in phase, and interfere constructively. The resultant radiation is *coherent*, as in a conventional laser. The radiation intensity grows exponentially during the interaction, and saturates when the microbunches are fully developed.

In this mechanism, the spontaneous emission in the first section of the undulator is amplified in the subsequent section. The mechanism is known as *self-amplified spontaneous emission* (SASE).

In some cases, an external laser is used in place of the spontaneous emission as the seed radiation to be amplified. The FEL is then said to be *seeded*.

The undulator shown in Fig. 2.1(a) is a *planar undulator*, as the trajectory of the electron beam is confined within the x-z plane. In a *helical undulator*, however, the trajectory of the electron beam is a helix. While the radiation produced in a planar undulator is linearly polarized, the radiation produced in a helical undulator is elliptically polarized. In this thesis, we consider only planar undulators.

2.2 Coherence and intensity

The coherence of the FEL radiation has an important implication on its intensity. Consider a total of N electrons, and suppose that the optical field emitted by each electron has an amplitude E_j and a phase ϕ_j, where $j \in \{1, 2, ..., N\}$.

Due to the superposition principle, the amplitude of the resultant optical field can be expressed as

$$E_{\text{tot}} = \left| \sum_{j=1}^{N} E_j e^{i\phi_j} \right|. \tag{2.1}$$

The total intensity (i.e. total power per unit area) is then given by

$$\mathscr{I}_{\text{tot}} = \frac{1}{2} c \epsilon_0 E_{\text{tot}}^2, \tag{2.2}$$

where c is the speed of light, and ϵ_0 is the vacuum permittivity.

Substituting Eq. (2.1) into Eq. (2.2), we have

$$\begin{aligned} \mathscr{I}_{\text{tot}} &= \frac{1}{2} c \epsilon_0 \left| \sum_{j=1}^{N} E_j e^{i\phi_j} \right|^2 \\ &= \frac{1}{2} c \epsilon_0 \left(\sum_{j=1}^{N} E_j e^{i\phi_j} \right) \left(\sum_{k=1}^{N} E_k e^{-i\phi_k} \right). \\ &= \frac{1}{2} c \epsilon_0 \left[\sum_{j=1}^{N} E_j^2 + \sum_{j=1}^{N} \sum_{\substack{k=1 \\ k \neq j}}^{N} E_j E_k e^{i(\phi_j - \phi_k)} \right]. \end{aligned} \tag{2.3}$$

If we assume that the optical fields emitted by all the individual electrons have the same amplitude E_1, then the intensity due to a single electron is

$$\mathscr{I}_1 = \frac{1}{2} c \epsilon_0 E_1^2, \tag{2.4}$$

and Eq. (2.3) can be written as

$$\mathscr{I}_{\text{tot}} = N \mathscr{I}_1 + \mathscr{I}_1 \sum_{j=1}^{N} \sum_{\substack{k=1 \\ k \neq j}}^{N} e^{i(\phi_j - \phi_k)}. \tag{2.5}$$

For the *incoherent* radiation in Fig. 2.1(b), the optical fields emitted by individual electrons are uncorrelated in phase, and the double sum in Eq. (2.5) equals zero. As a result, the total intensity is

$$\mathscr{I}_{\text{tot}} = N \mathscr{I}_1,$$

which scales with the total number of electrons N.

For the *coherent* radiation in Fig. 2.1(c), adjacent microbunches are separated by the radiation wavelength λ, which corresponds to a phase difference of 2π. For all $j, k \in \{1, 2, ..., N\}$, there exists an integer n such that $\phi_j - \phi_k \approx 2n\pi$. In Eq. (2.5), each term in the double sum essentially equals unity. Since there are $N^2 - N$ terms in the double sum, the total intensity is

$$\mathscr{I}_{\text{tot}} = N \mathscr{I}_1 + (N^2 - N) \mathscr{I}_1 = N^2 \mathscr{I}_1,$$

which scales with the *square* of the total number of electrons N.

In an electron bunch, the total number of electrons N can well exceed 10^7. In other words, the intensity of the coherent radiation can be higher than that of the incoherent radiation by more than seven orders of magnitude. This analysis reaffirms that coherence is a very important property of the FEL radiation.

2.3 Definition of parameters

2.3.1 Radiation

In order to proceed with the FEL theory, it is necessary to define a number of parameters. We first concern ourselves with the parameters which pertain to the radiation:

- λ is the optical wavelength;
- $k = 2\pi/\lambda$ is the optical wavenumber;
- ω is the optical angular frequency;
- E_0 is the amplitude of the optical field on the z axis;
- ϕ is the phase of the optical field on the z axis;
- σ_r is the rms transverse radius of the optical beam.

It is often convenient to scale the optical field amplitude into the dimensionless parameter

$$a \equiv \frac{e E_0}{\sqrt{2}\, m_e c^2 k}, \tag{2.6}$$

where e is the absolute value of the electron charge, and $m_e c^2$ is the rest energy of the electron.

2.3.2 Undulator

Next, we define the parameters pertaining to the undulator:

- λ_u is the undulator period;
- $k_u = 2\pi/\lambda_u$ is the undulator wavenumber;
- B_0 is the amplitude of the undulator field on the z axis.

Note that B_0 depends on the gap height, i.e. the distance between the magnetic poles above and below the electron beam path.

The dimensionless *undulator parameter* is defined as

$$K \equiv \frac{e B_0}{m_e c\, k_u}, \tag{2.7}$$

and the *rms undulator parameter* is defined as

$$a_u \equiv \frac{K}{\sqrt{2}}. \tag{2.8}$$

For planar undulator, there is a coupling factor

$$f_B \equiv J_0\left(\frac{K^2}{4+2K^2}\right) - J_1\left(\frac{K^2}{4+2K^2}\right) \tag{2.9}$$

between the electrons and the optical field, due to the longitudinal oscillations of the electrons in the undulator. Here J_0 and J_1 are Bessel functions.

In this thesis, the symbols λ_u, k_u and a_u are used interchangeably with λ_w, k_w and a_w. The subscript u stands for "undulator", and the subscript w stands for "wiggler". Without undulator tapering, λ_u, k_u, B_0, a_u and f_B are constants.

2.3.3 Electrons

In the longitudinal phase space, the motion of each electron is described by an energy variable and a phase variable.

A common choice of the energy variable is the Lorentz factor

$$\gamma \equiv \frac{1}{\sqrt{1-v^2/c^2}}, \tag{2.10}$$

which is the energy normalized to $m_e c^2$.

A common choice of the phase variable is

$$\psi \equiv (k+k_u)z - \omega t + \phi, \tag{2.11}$$

known as the *ponderomotive phase*.

In addition, we define the following parameters pertaining to the electron beam:

- I_0 is the peak current;
- σ_t is the rms bunch length;
- $\sigma_{x,y}$ is the rms transverse radius of the electron beam;
- $\varepsilon_{x,y}$ is the normalized transverse emittance;
- $\beta_{x,y}$ is the beta function.

The normalized emittance, the beta function, and the rms transverse radius are related by

$$\sigma_{x,y} = \sqrt{\frac{\varepsilon_{x,y}\beta_{x,y}}{\gamma}}. \tag{2.12}$$

The power of the electron beam is given by

$$P_{\text{beam}} = \frac{\gamma m_e c^2 I_0}{e}. \tag{2.13}$$

The *bunching factor* of the electron beam is defined as

$$b \equiv \left|\left\langle \exp(-i\psi)\right\rangle\right|, \tag{2.14}$$

where the chevrons denote the average over all electrons, and the vertical bars denote the absolute value. The bunching factor measures how well the microbunches are developed. It equals 0 when all the electrons are randomly phased. It equals 1 when the phase separation between every two electrons is exactly a multiple of 2π.

For an electron bunch with a Gaussian longitudinal profile, the current I at any coordinate t within the bunch is given by

$$I(t) = I_0 \exp\left(-\frac{t}{2\sigma_t}\right). \tag{2.15}$$

The bunch charge is given by

$$Q = \int_{-\infty}^{\infty} I(t) d\,t = \sqrt{2\pi}\, I_0 \sigma_t. \tag{2.16}$$

The current density is given by

$$J = \frac{I}{2\pi\sigma_x^2}. \tag{2.17}$$

2.3.4 Other parameters

The dimensionless FEL parameter, which is also called the *Pierce parameter*, is defined as [13]

$$\rho \equiv \frac{1}{2\gamma}\left(\frac{I}{I_A}\right)^{1/3}\left(\frac{K f_B}{k_u \sigma_x}\right)^{2/3}. \tag{2.18}$$

For x-ray FELs, ρ is typically on the order of 10^{-3}. In Eq. (2.18),

$$I_A = \frac{4\pi\epsilon_0 m_e c^3}{e} \approx 17\ \text{kA} \tag{2.19}$$

is the Alfvén current.

During the FEL interaction, the radiation power grows exponentially, and can be expressed as

$$P(z) \propto \exp\left(\frac{z}{L_g}\right), \tag{2.20}$$

where L_g is known as the *gain length*. In terms of the Pierce parameter, the gain length is defined as [13]

$$L_g \equiv \frac{\lambda_u}{4\sqrt{3}\pi\rho}. \tag{2.21}$$

In addition, the *saturation length* can be estimated by [13]

$$L_{\text{sat}} \approx \frac{\lambda_u}{\rho}, \tag{2.22}$$

and the *saturation power* can be estimated by [13]

$$P_{\text{sat}} \approx \rho P_{\text{beam}}. \tag{2.23}$$

Note that the formulae (2.21), (2.22) and (2.23) are based on the one-dimensional FEL model. The Ming Xie parametrization [14] extends these formulae to the three-dimensional model.

2.4 One-dimensional model

The one-dimensional model of the FEL interaction comprises the longitudinal dynamics of the electrons and the evolution of the optical field on the z axis. It captures the most basic essence of the FEL interaction, and is easier to comprehend than the three-dimensional model. It can be described by four differential equations:

$$\frac{d\gamma}{dz} = -\frac{e}{2m_e c^2}\frac{K f_B E_0}{\gamma}\sin\psi, \tag{2.24}$$

$$\frac{d\psi}{dz} = k_u - \frac{k}{2\gamma^2}\left(1 + a_u^2 - 2a a_u f_B \cos\psi + a^2\right) + \frac{d\phi}{dz}, \tag{2.25}$$

$$\frac{dE_0}{dz} = \frac{1}{2c\epsilon_0} K f_B J \left\langle \frac{\sin\psi}{\gamma} \right\rangle, \tag{2.26}$$

$$\frac{d\phi}{dz} = \frac{1}{2c\epsilon_0}\frac{K f_B J}{E_0}\left\langle \frac{\cos\psi}{\gamma} \right\rangle. \tag{2.27}$$

Eqs. (2.24) and (2.25) govern the γ and ψ evolution of each electron, while Eqs. (2.26) and (2.27) govern the E_0 and ϕ evolution of the optical field. These equations are derived in Refs. [15] and [16].

In particular, it is possible to simplify Eq. (2.25) by means of two approximations, as it is done in Ref. [15]. The first one is the *slowly varying envelope approximation* (SVEA):

$$\frac{dE_0}{dz} \ll k E_0. \tag{2.28}$$

Dividing (2.27) by (2.26), we have

$$\frac{d\phi}{dz} = \frac{1}{E_0}\frac{dE_0}{dz}\frac{\langle \cos\psi/\gamma \rangle}{\langle \sin\psi/\gamma \rangle} \ll k. \tag{2.29}$$

In other words, on the right-hand side of Eq. (2.25), the last term is small compared to the second term, and can therefore be neglected.

The second approximation is that $a_u \gg a$. By extension, $a a_u$ and a^2 are small compared to a_u^2. This allows us to neglect the last two terms within the parentheses in Eq. (2.25).

Upon making these approximations, Eq. (2.25) reduces to

$$\frac{d\psi}{dz} = k_u - \frac{k}{2\gamma^2}\left(1+a_u^2\right), \tag{2.30}$$

which does not depend explicitly on E_0 or ϕ.

2.5 Resonant energy

The *resonance condition* of the FEL interaction is defined by the criterion that the ponderomotive phase remains stationary:

$$\frac{d\psi}{dz} = k_u - \frac{k}{2\gamma^2}\left(1+a_u^2\right) = 0. \tag{2.31}$$

The electron energy $\gamma = \gamma_R$ fulfilling this condition is known as the *resonant energy*, and can be expressed as

$$\gamma_R = \sqrt{\frac{k}{2k_u}\left(1+a_u^2\right)} = \sqrt{\frac{\lambda_u}{2\lambda}\left(1+\frac{K^2}{2}\right)}. \tag{2.32}$$

In the case of monochromatic seeding, λ is the wavelength of the seed radiation, and γ_R is determined by λ through Eq. (2.32). In the case of SASE, γ_R is determined by the energy of the injected electron beam, and λ is determined by γ_R through Eq. (2.32).

Without undulator tapering, λ_u and K are constants. In order to keep the radiation wavelength λ unchanged, Eq. (2.32) demands γ_R to be constant.

It is often convenient to express the energy of an electron as the relative deviation from the resonant energy, using the variable

$$\eta \equiv \frac{\gamma - \gamma_R}{\gamma_R}. \tag{2.33}$$

2.6 Simplified equations of motion

Eqs. (2.24) and (2.30) are the equations of motion for an electron in the longitudinal phase space. Using the variable η and assuming that undulator tapering is not applied, these two equations can be further simplified to:

$$\frac{d\eta}{dz} = -\frac{\Omega^2}{2k_u}\sin\psi, \tag{2.34}$$

$$\frac{d\psi}{dz} = 2k_u\eta. \tag{2.35}$$

In Eq. (2.34), the variable

$$\Omega = \sqrt{\frac{e}{m_e c^2}\frac{k_u K f_B E_0}{\gamma_R^2}} \propto \sqrt{E_0} \tag{2.36}$$

has the dimension of inverse length, and scales with the square root of the optical field amplitude E_0.

By substituting Eq. (2.34) into the derivative of Eq. (2.35), we obtain the second-order differential equation

$$\frac{d^2\psi}{dz^2} + \Omega^2 \sin\psi = 0, \tag{2.37}$$

which is the familiar equation for a simple pendulum. This shows that the electron motion in ψ is oscillatory during the FEL interaction. The oscillatory motion is known as *synchrotron oscillation*, and has an angular frequency Ω given by Eq. (2.36). Correspondingly,

$$L_{\text{sync}} = \frac{2\pi}{\Omega} \tag{2.38}$$

is known as the *synchrotron period*.

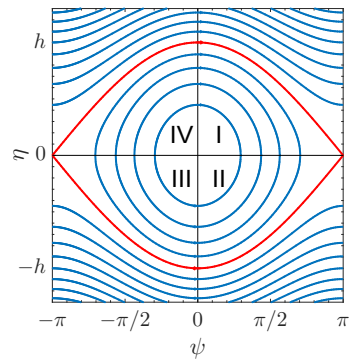

Figure 2.2. *Electron trajectories in the four quadrants (I, II, III, IV) of the longitudinal phase space (ψ,η) during the FEL interaction. The trajectory highlighted in red is the separatrix, which defines the ponderomotive bucket.*

2.7 Phase space trajectories

The equations of motion (2.34) and (2.35) satisfy the Hamilton equations

$$\frac{d\eta}{dt} = -\frac{\partial H}{\partial \psi}, \tag{2.39}$$

$$\frac{d\psi}{dt} = \frac{\partial H}{\partial \eta} \tag{2.40}$$

for the Hamiltonian

$$H(\psi,\eta) = c\,k_u\eta^2 + \frac{c\Omega^2}{2k_u}(1-\cos\psi). \tag{2.41}$$

In the longitudinal phase space (ψ,η), the trajectories of the electrons are given by the level set of the function $H(\psi,\eta)$. The trajectories are shown in Fig. 2.2 over the range of one radiation wavelength, $-\pi \le \psi \le \pi$.

In particular, the trajectory highlighted in red is the *separatrix*. Along the separatrix, the Hamiltonian has the value

$$H_{\text{sep}} = H(\pm\pi, 0) = \frac{c\Omega^2}{k_u}. \tag{2.42}$$

The region enclosed by the separatrix is known as the *ponderomotive bucket*. Within the bucket, $H < H_{\text{sep}}$. The trajectories are closed orbits, and the electrons are said to be *trapped*. Outside the bucket, $H > H_{\text{sep}}$. The trajectories are unbound, and the electrons are said to be *untrapped*.

By setting $H = H_{\text{sep}}$, we obtain the equation for the separatix:

$$\eta^2 = \frac{\Omega^2}{2k_u^2}(1+\cos\psi). \tag{2.43}$$

The maximum η value along the separatrix gives the half-height of the bucket,

$$h = \frac{\Omega}{k_u}. \tag{2.44}$$

Invoking Eq. (2.36), we obtain the proportionality

$$h \propto \sqrt{E_0}, \tag{2.45}$$

showing that the bucket increases in height as the optical field is amplified.

In Fig. 2.2, the horizontal line $\eta = 0$ and the vertical line $\psi = 0$ divide the longitudinal phase space into four quadrants, as indicated by the Roman numerals.

In quadrants I and II, we have $\psi > 0$. In quadrants III and IV, we have $\psi < 0$. According to Eq. (2.34), this implies $d\eta/dz < 0$ in quadrants I and II, and $d\eta/dz > 0$ in quadrants III and IV. In other words, electrons *decelerate* in quadrants I and II, and *accelerate* in quadrants III and IV.

Due to the principle of energy conservation, energy is transferred to the optical field in quadrants I and II, and energy is absorbed from the optical field in quadrants III and IV.

In quadrants I and IV, we have $\eta > 0$. In quadrants II and III, we have $\eta < 0$. According to Eq. (2.35), this implies that electrons moves *forward* in ψ in quadrants I and IV, and moves *backward* in ψ in quadrants II and III.

2.8 Simplified equations of the optical field

The equations (2.26) and (2.27) govern the evolution of the optical field. Without undulator tapering and with the approximation that $\gamma \approx \gamma_R$ for all electrons, these equations can be simplified to

$$\frac{dA}{dz} = k_u \langle \sin\psi \rangle, \tag{2.46}$$

$$\frac{d\phi}{dz} = \frac{k_u}{A} \langle \cos\psi \rangle. \tag{2.47}$$

Here we have defined the new dimensionless variable

$$A = \frac{2c\epsilon_0 k_u \gamma_R}{K f_B J} E_0 \tag{2.48}$$

for the scaled optical field amplitude. By invoking Eqs. (2.6), (2.17), (2.18), (2.19) and (2.36), it is possible to rewrite A as

$$A = \frac{K f_B}{16\gamma_R^2 \rho^3} \frac{k}{k_u} a \tag{2.49}$$

or

$$A = \frac{\Omega^2}{16 k_u^2 \rho^3}. \tag{2.50}$$

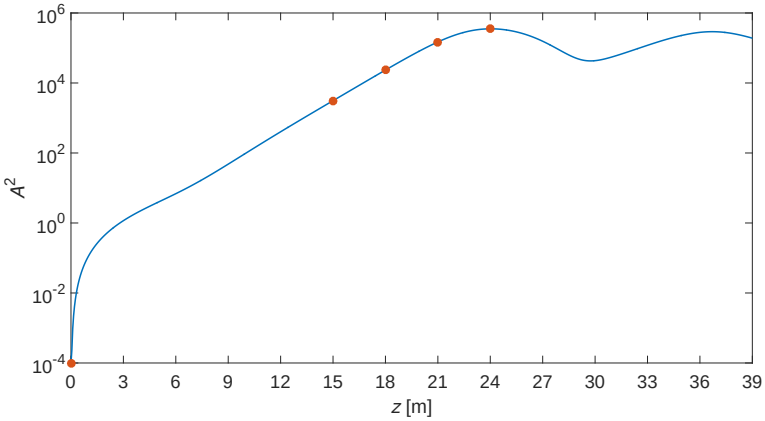

Figure 2.3. *The scaled optical intensity A^2 as a function of the distance z along the undulator. Note that the vertical axis is on a logarithmic scale.*

Hence, the equations of motion (2.34) and (2.35) for the electrons can be written in terms of A as

$$\frac{d\eta}{dz} = -8k_u\rho^3 A\sin\psi, \tag{2.51}$$

$$\frac{d\psi}{dz} = 2k_u\eta. \tag{2.52}$$

2.9 Numerical integration

Upon simplifying the equations, the one-dimensional FEL model can now be described by (2.46), (2.47), (2.51) and (2.52). In this section, we integrate these equations numerically, to examine the FEL interaction in greater detail.

We perform the integration for 15000 particles over the range of $-3\pi \le \psi \le 3\pi$. Furthermore, we assume $k_u = 200\ \mathrm{m}^{-1}$ and $\rho = 10^{-3}$.

We use the following initial conditions at $z = 0$. First, the seed radiation has $A = 10^{-2}$ and $\phi = \pi/2$. Second, the electron beam is on resonance ($\eta = 0$), and has an even distribution within an energy spread of $\Delta\eta = 2\times10^{-4}$. Third, the electron beam has an even distribution in ψ.

As we integrate the equations numerically along the z axis, we obtain the evolution of η and ψ for each particle, as well as the evolution of A and ϕ for the optical field. In particular, the evolution of A^2 along the z axis is shown in Fig. 2.3 on a logarithmic scale.

Note that the optical intensity $\mathscr{I}$ is directly proportional to E_0^2 [see Eq. (2.2)], and hence A^2 [see Eq. (2.48)]. Thus, Fig. 2.3 can be seen as a plot of the *scaled intensity* versus z.

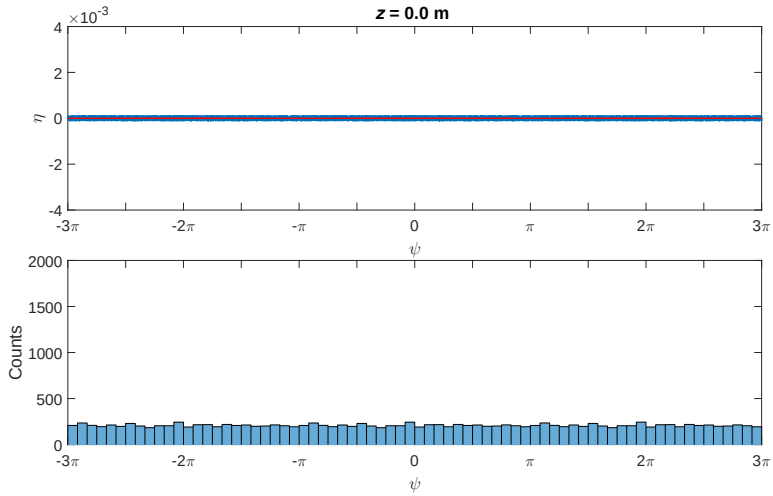

Figure 2.4. *Initial conditions, illustrated by the longitudinal phase space* (ψ, η) *and the histogram of* ψ *at* $z = 0$*. The particles are shown in blue, and the ponderomotive bucket is shown by the red curve.*

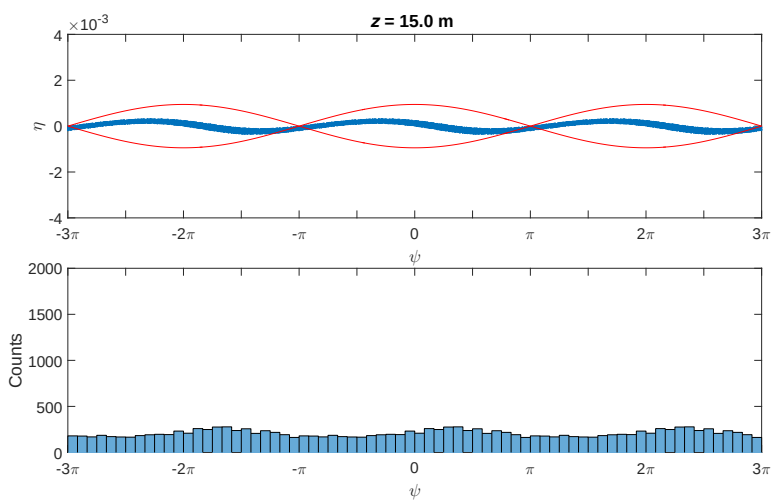

Figure 2.5. *Energy modulation, illustrated by the longitudinal phase space* (ψ, η) *and the histogram of* ψ *at* $z = 15$ *m.*

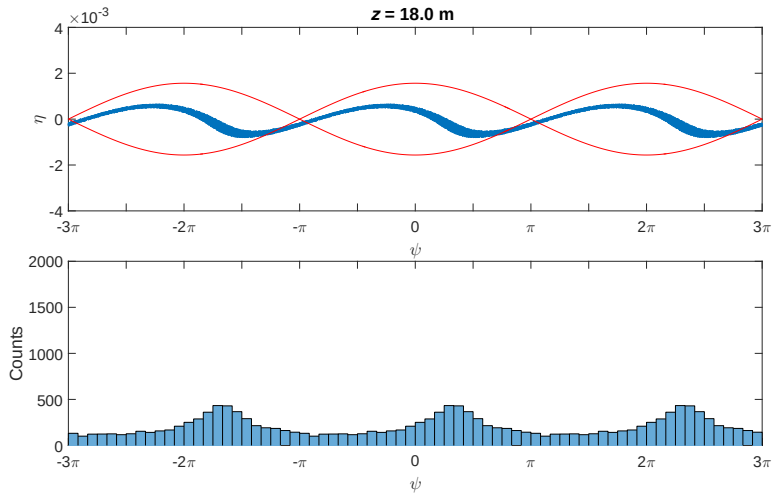

Figure 2.6. *Density modulation, illustrated by the longitudinal phase space* (ψ, η) *and the histogram of* ψ *at* $z = 18$ *m.*

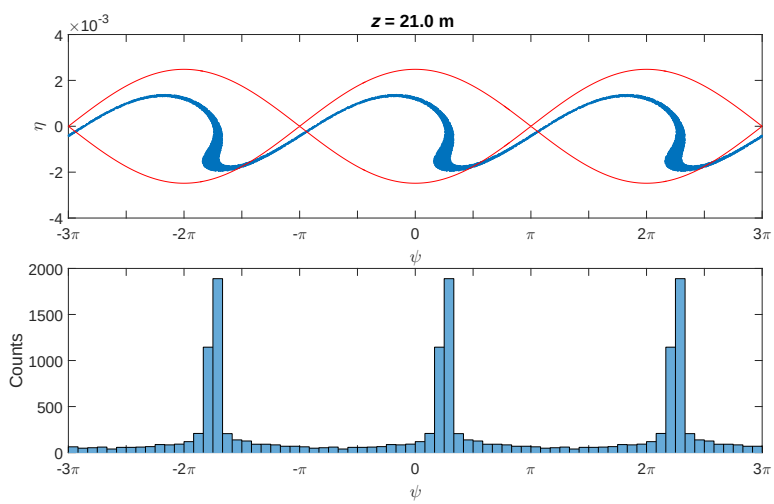

Figure 2.7. *Fully developed microbunches, illustrated by the longitudinal phase space* (ψ, η) *and the histogram of* ψ *at* $z = 21$ *m.*

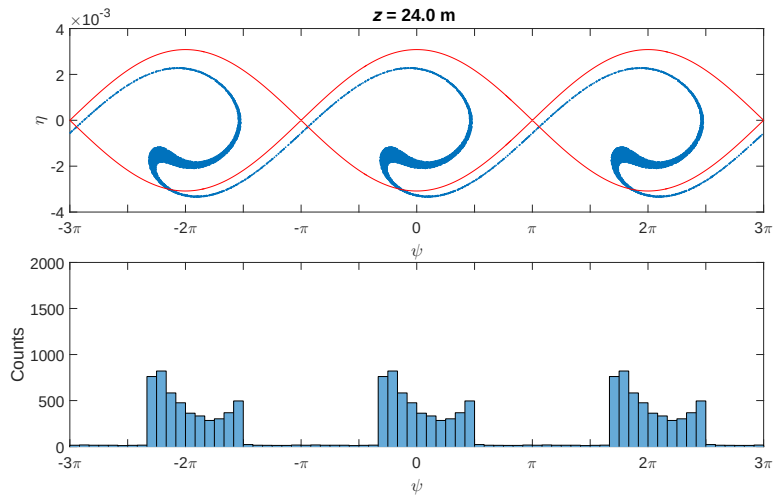

Figure 2.8. *Dissolution of microbunches, illustrated by the longitudinal phase space* (ψ,η) *and the histogram of* ψ *at* $z = 24$ *m.*

Referring to Fig. 2.3, the intensity at $z = 0$ is determined by the seed radiation. As the vertical axis is on a logarithmic scale, an exponential growth in intensity is represented by a rising straight line.

The exponential growth does not start until $z = 8$ m. Prior to that, the intensity is in the so-called "lethargy regime". In this regime, the different optical modes compete with each other until the exponential growth mode becomes dominant.

At $z = 21$ m, the intensity ceases to grow exponentially, and begins to saturate. The intensity reaches its maximum at $z = 24$ m, and subsequently remains below this maximum. In the following, we examine the longitudinal phase space (ψ,η) at the z positions indicated by the five orange dots.

Figure 2.4 shows the initial condition at $z = 0$. In the (ψ,η) plot on the top, the particles are shown in blue, and the ponderomotive bucket is shown by the red curve. The corresponding histogram of ψ at the bottom verifies the even distribution of the particles.

At $z = 0$, the pondermotive bucket is hardly visible. The reason is that the bucket height scales with $\sqrt{E_0}$ [see Eq. (2.45)], and hence $\sqrt{A}$ [see Eq. (2.48)]. Before any amplification, A is still relatively small.

Figure 2.5 shows the snapshot at $z = 15$ m. By now, the bucket has already grown significantly in height, and the particles follow the trajectories depicted in Fig. 2.2. Within each bucket, particles in the left half gain energy (move towards $\eta > 0$), while particles in the right half lose energy (move towards $\eta < 0$). As a result, a periodic *energy modulation* is imparted on the electron beam.

Figure 2.6 shows the snapshot at $z = 18$ m. The bucket continues to grow in height, as the electron beam continues to radiate. Following the trajectories depicted in Fig. 2.2, particles with $\eta > 0$ move forward in ψ, while particles with $\eta < 0$ move backward in ψ. This converts the energy modulation is into a *density modulation*. As seen in the histogram of ψ at the bottom, *microbunches* start to emerge at intervals of 2π.

Figure 2.7 shows the snapshot at $z = 21$ m. At this point, the microbunches are fully developed. As seen in the histogram of ψ, each microbunch has a very high number of particles within a small ψ spread. Beyond this point, the particle density cannot get any higher.

Figure 2.8 shows the snapshot at $z = 24$ m. At this point, particles with $\eta > 0$ continue to move forward in ψ, and particles with $\eta < 0$ continue to move backward in ψ. This leads to a decrease in particle density, and the dissolution of the microbunches.

2.10 Saturation and efficiency

The numerical integration in Section 2.9 illustrates the physics up to the saturation point, after which the radiation power does not increase any further. According to Eq. (2.23), the FEL efficiency is then given by the Pierce parameter $\rho \approx P_{\text{sat}}/P_{\text{beam}}$. For x-ray FELs, ρ is typically on the order of 10^{-3}.

The saturation sets a limit on the FEL efficiency. The "efficiency enhancement techniques" discussed in the remainder of this thesis are all about overcoming this limit, and sustaining the growth of radiation power beyond the saturation point.

Upon applying an "efficiency enhancement technique", we refer to the original saturation point as the *initial* saturation point, and the new saturation point as the *final* saturation point.

CHAPTER 3

UNDULATOR TAPERING

This chapter introduces the technique of undulator tapering, and provides the background knowledge for Papers I, II and III.

3.1 What is undulator tapering?

In the default operation mode of a free-electron laser, the undulator period λ_u and the undulator parameter K are constant.

With the implementation of undulator tapering, K is no longer constant. Instead, K is made to decrease gradually along the z axis, for the purpose of sustaining the growth of radiation power beyond the initial saturation point, and enhancing the FEL efficiency.

The function $K(z)$ is called the *taper profile*. An important goal of this thesis is to optimize the taper profile for the maximum enhancement in FEL efficiency.

In principle, tapering can also be implemented by varying λ_u and K *simultaneously* along the z axis. However, this is less commonly done, and is not considered in this thesis.

While λ_u is kept constant, the value of K is determined solely by the gap height between the permanent magnetic poles. In order to vary K along the z axis, a *variable-gap* undulator line is needed.

In the ideal case, $K(z)$ is a smooth, continuous function. In most existing FEL facilities, however, the undulator line consists of discrete modules. Each module is typically a few metres long, and K is uniform within each module. In between the modules, there are drift sections, where various instruments are installed for the focusing, trajectory correction, phase shifting and diagnostics of the electron beam. In such cases, $K(z)$ is a piecewise function.

The physics of an FEL with a tapered undulator line is described by the Kroll-Morton-Rosenbluth (KMR) model [15]. The model is based on a one-dimensional Hamiltonian formulation. It is reviewed in Refs. [16], [18] and [19].

3.2 Approaches to taper optimization

There are various methods of optimizing the taper profile. The "traditional" method involves engaging the undulator modules one by one, from upstream to downstream. At each module, the gap height is adjusted to maximize the intermediate radiation power.

However, as we will see in Paper II, maximizing the *intermediate* power does not necessarily yield the highest *final* power. In fact, it is often possible to increase the power downstream by sacrificing the power upstream.

An alternative is the multidimensional scanning method used in Paper III. The optimal taper profile is obtained by brute-force scanning over a multidimensional parameter space, comprising the taper order (such as linear and quadratic), the taper start point and the taper gradient. The advantage of this method is its relative ease to implement empirically.

A more interesting approach is to develop optimization methods based on the KMR model, as it is done in Paper I. This model-based approach allows us to examine the underlying physics of undulator tapering in greater detail.

Moreover, Paper I proposes and justifies a modification to the KMR model. The modified model opens up possibilities of further enhancement in FEL efficiency beyond the original model.

3.3 The KMR model

In the KMR model, the taper profile $K(z)$ does not have a predefined functional form, such as linear or quadratic. Instead, it is determined by the dynamics of a *resonant particle*.

In the (ψ,γ) space, the coordinates of this particle are denoted by (ψ_R,γ_R). They are subject to the following constraints:

$$\gamma_R(z) = \sqrt{\frac{\lambda_u}{2\lambda}\left[1+\frac{K^2(z)}{2}\right]}, \tag{3.1}$$

$$\psi_R(z) = \text{constant}. \tag{3.2}$$

In the constraint (3.2), the actual value of the constant is to be chosen. Meanwhile, the constraint (3.1) is identical to the resonant condition (2.32), except that γ_R and K are no longer constant. As the resonant particle is on resonance at all z, it is a representative of the particles participating in the FEL interaction.

For the resonant particle, the equation of motion (2.24) can be written as

$$\frac{d\gamma_R}{dz} = -\frac{e}{2m_e c^2}\frac{K(z)f_B(z)E_0(z)}{\gamma_R(z)}\sin[\psi_R(z)]. \tag{3.3}$$

This equation defines the relation between γ_R and ψ_R. Given the constraints (3.1) and (3.2), it determines the taper profile $K(z)$.

When $\gamma_R(z)$ decreases, the resonant particle *decelerates*. Due to the principle of energy conservation, the energy lost by the resonant particle is transferred to the optical field. A necessary condition for a continuous energy transfer to the optical field is that $\gamma_R(z)$ is a monotonically decreasing function.

This leads to two further restrictions. First, according to Eq. (3.1), $K(z)$ is required to be a monotonically decreasing function as well. Second, this means

$$\frac{d\gamma_R}{dz} < 0$$

for all z. According to Eq. (3.3), this requires

$$\sin\psi_R > 0.$$

Within the first period of ψ, this translates to

$$0 < \psi_R < \pi.$$

Note that $\psi_R = 0$ is a special case, corresponding to a uniform (i.e. untapered) undulator line. This is evidenced by the following. In Eq. (3.3), $\psi_R = 0$ implies $d\gamma_R/dz = 0$, meaning that γ_R is constant. In Eq. (3.1), a constant γ_R implies a constant K, meaning that the undulator line is untapered.

3.4 Motion around the resonant particle

In this section, we examine the motion of the particles in the close vicinity of the resonant particle. For these particles, $\gamma \approx \gamma_R$. Using the variable η defined in (2.33),

$$\begin{aligned}\frac{d\eta}{dz} &= \frac{d}{dz}\left(\frac{\gamma-\gamma_R}{\gamma_R}\right)\\ &= \frac{1}{\gamma_R}\frac{d\gamma}{dz} - \frac{\gamma}{\gamma_R^2}\frac{d\gamma_R}{dz}\\ &\approx \frac{1}{\gamma_R}\left(\frac{d\gamma}{dz} - \frac{d\gamma_R}{dz}\right).\end{aligned}$$

Invoking Eqs. (2.24) and (3.3), we obtain a new equation of motion for the variable η:

$$\frac{d\eta}{dz} = -\frac{e}{2m_e c^2}\frac{K f_B E_0}{\gamma_R^2}\left(\sin\psi - \sin\psi_R\right). \tag{3.4}$$

In the special case of $\psi_R = 0$, Eq. (3.4) reduces to the original equation of motion (2.34) for an untapered undulator line.

Meanwhile, the equation of motion for the variable ψ remains the same as in (2.35):

$$\frac{d\psi}{dz} = 2k_u\eta. \tag{3.5}$$

As we are interested in the particles with $\psi \approx \psi_R$, we may make the approximations $\sin(\psi-\psi_R) \approx \psi-\psi_R$ and $\cos(\psi-\psi_R) \approx 1$. Applying these approximations to Eq. (3.4), we have

$$\begin{aligned}\frac{d\eta}{dz} &= -\frac{e}{2m_e c^2}\frac{K f_B E_0}{\gamma_R^2}\left\{\sin\left[(\psi-\psi_R)+\psi_R\right]-\sin\psi_R\right\} \\ &= -\frac{e}{2m_e c^2}\frac{K f_B E_0}{\gamma_R^2}\left[\sin(\psi-\psi_R)\cos\psi_R\right. \\ &\qquad \left.+\cos(\psi-\psi_R)\sin\psi_R-\sin\psi_R\right] \\ &\approx -\frac{e}{2m_e c^2}\frac{K f_B E_0}{\gamma_R^2}(\psi-\psi_R)\cos\psi_R. \end{aligned} \tag{3.6}$$

Substituting Eq. (3.6) into the derivative of Eq. (3.5) yields the second-order differential equation

$$\frac{d^2\psi}{dz^2}+\widetilde{\Omega}^2(\psi-\psi_R)=0, \tag{3.7}$$

where

$$\widetilde{\Omega}=\sqrt{\frac{e}{m_e c^2}\frac{k_u K f_B E_0}{\gamma_R^2}\cos\psi_R}\,. \tag{3.8}$$

Note that Eq. (3.7) describes a harmonic oscillator. It reveals the *synchrotron oscillations* of the particles along a tapered undulator line, with $\widetilde{\Omega}$ being the angular frequency.

In an untapered undulator line, the synchrotron oscillations are centred at the phase $\psi = 0$ [see Eq. (2.37)]. In a tapered undulator line, however, the oscillations are centred at the phase ψ_R of the resonant particle [see Eq. (3.7)].

In the special case where $\psi_R = 0$, the expression (3.8) reduces to (2.36). We then have $\widetilde{\Omega} = \Omega$, where Ω (without the tilde) is synchrotron frequency for an untapered undulator line.

3.5 Phase space trajectories

In terms of the synchrotron frequency Ω for an *untapered* undulator line [see Eq. (2.36)], the equations of motion (3.4) and (3.5) for a *tapered* undulator line can be written as

$$\frac{d\eta}{dz} = -\frac{\Omega^2}{2k_u}\left(\sin\psi-\sin\psi_R\right), \tag{3.9}$$

$$\frac{d\psi}{dz} = 2k_u\eta. \tag{3.10}$$

These equations satisfy the Hamilton equations (2.39) and (2.40) for the Hamiltonian

$$H(\psi,\eta)=c\,k_u\eta^2+\frac{c\Omega^2}{2k_u}\left[\cos\psi_R-\cos\psi-(\psi-\psi_R)\sin\psi_R\right]. \tag{3.11}$$

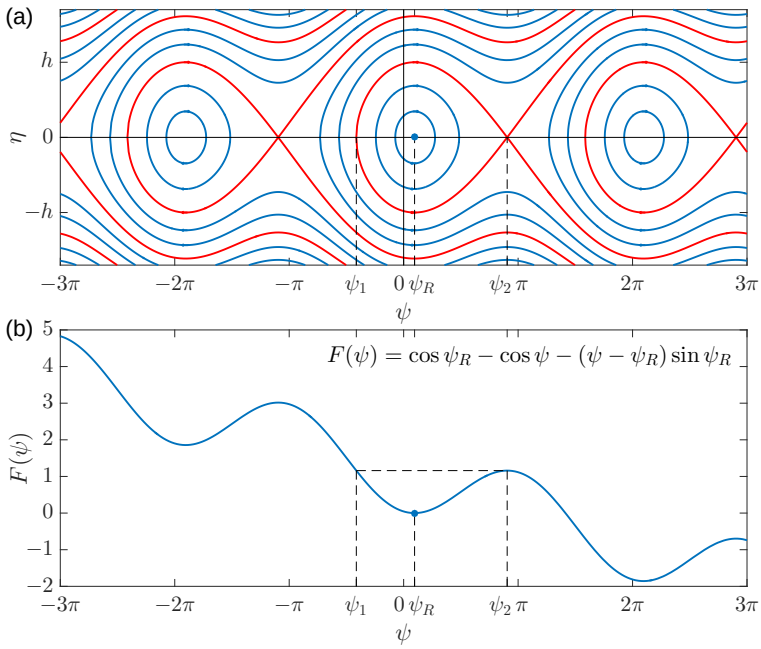

Figure 3.1. *(a) The electron trajectories in the longitudinal phase space (ψ,η) for an FEL with a tapered undulator line. A trajectory in red is a separatrix. (b) The ψ dependence of the corresponding potential well.*

Again, we can verify that Eq. (3.11) reduces to the corresponding expression (2.41) for an untapered undulator line when $\psi_R = 0$.

As the Hamiltonian H does not have any explicit time dependence, it equals the total mechanical energy. For any given Ω value, H is a constant of motion. The electron trajectories in the (ψ,η) space is therefore given by the level set of $H(\psi,\eta)$. For $\psi_R \neq 0$, the electron trajectories are shown in Fig. 3.1(a) over the range of three radiation wavelengths, $-3\pi \leq \psi \leq 3\pi$.

In Fig. 3.1(a), each red curve encloses a region where the electron trajectories are closed orbits. Outside the enclosed region, the electron trajectories are unbound. The red curve is the *separatrix*, and the region enclosed by it is the *ponderomotive bucket*.

The trajectory pattern in Fig. 3.1(a) is periodic in ψ, and repeats itself at intervals of 2π. With no loss of generality, we focus on the bucket within the interval $-\pi \leq \psi \leq \pi$ from now on. An obvious observation is that the bucket is deformed, compared to the one in Fig. 2.2 for an untapered undulator line.

The deformed bucket is no longer symmetric. The closed orbits are now centred around the point $(\psi_R, 0)$ instead of the origin $(0,0)$. The point $(\psi,\eta) = (\psi_R, 0)$ is known as the *centroid* of the bucket.

Furthermore, the deformed bucket covers a smaller range in ψ. While the original bucket has a full width of 2π, the deformed bucket only extends from some $\psi_1 > -\pi$ to some $\psi_2 < \pi$. In other words, for a tapered undulator line, there exists some ψ values at which *no* particles can be trapped.

3.6 Potential well

The Hamiltonian H in (3.11) gives the total mechanical energy of a particle. The first term depends solely on η, and can be interpreted as the kinetic energy; the second term depends solely on ψ, and can be interpreted as the potential energy.

Figure 3.1(b) shows the ψ dependence of the potential energy, given by the function

$$F(\psi) = \cos\psi_R - \cos\psi - (\psi - \psi_R)\sin\psi_R. \tag{3.12}$$

Within the interval $-\pi \le \psi \le \pi$, the function $F(\psi)$ has a local minimum at ψ_R, and a local maximum at

$$\psi_2 = \pi - \psi_R. \tag{3.13}$$

The interval $\psi_1 < \psi < \psi_2$ corresponds to a bucket in Fig. 3.1(a), and a *potential well* in Fig. 3.1(b).

In Fig. 3.1(b), if the total mechanical energy H of a particle is less than the potential energy at $\psi = \psi_2$, then the particle will stay within the potential well, and its motion will be bound. Otherwise, the particle will escape into the region $\psi > \psi_2$, and its motion will be unbound.

When the total mechanical energy H equals the potential energy, the kinetic energy vanishes, and $\eta = 0$. Thus, the critical value of H that separates the bound and unbound trajectories is $H(\psi_2, 0)$. This critical value also determines the Hamiltonian H_{sep} along the separatrix in the (ψ, η) space:

$$H_{\text{sep}} = H(\psi_2, 0) = \frac{c\Omega^2}{2k_u}\left[2\cos\psi_R - (\pi - 2\psi_R)\sin\psi_R\right]. \tag{3.14}$$

By setting $H = H_{\text{sep}}$, we obtain the equation for the separatrix:

$$\eta^2 = \frac{\Omega^2}{2k_u^2}\left[\cos\psi_R + \cos\psi - (\pi - \psi_R - \psi)\sin\psi_R\right]^{1/2}. \tag{3.15}$$

As the potential function (3.12) has a local minimum at $\psi = \psi_R$, the Hamiltonian (3.11) has a local minimum at $(\psi, \eta) = (\psi_R, 0)$. This implies that the centroid $(\psi, \eta) = (\psi_R, 0)$ is a stable point within the bucket in Fig. 3.1(a). If a particle lies at the centroid, it will remain stationary with respect to the bucket.

Meanwhile, $(\psi_R, 0)$ are precisely the coordinates of the resonant particle in the (ψ, η) space. Thus, the resonant particle *defines* the centroid of the bucket, and is stationary with respect to the bucket.

3.7 Bucket deceleration

As defined by (2.33), the energy variable η is the relative energy deviation from the resonant particle. For the resonant particle itself, the η value is always zero. When the resonant particle decelerates, its η value remains unchanged.

For the purpose of tracking the resonant particle, η is not a convenient choice of energy variable. Therefore, we now switch back to the energy variable γ, so that the energy of the resonant particle is described by $\gamma(z)=\gamma_R(z)$. As the resonant particle decelerates, $\gamma_R(z)$ decreases. In the (ψ,γ) space, the resonant particle *descends*.

By substituting (2.33) into (3.15), we obtain the equation for the separatrix in the (ψ,γ) space:

$$\gamma_\pm(\psi)=\gamma_R\pm\frac{\Omega\gamma_R}{\sqrt{2}\,k_u}[\cos\psi_R+\cos\psi-(\pi-\psi_R-\psi)\sin\psi_R]^{1/2}. \quad (3.16)$$

This is equivalent to Eq. (8) in Paper I. $\gamma_+(\psi)$ refers to the part of the separatrix with $\gamma>\gamma_R$, and $\gamma_-(\psi)$ refers to the part with $\gamma<\gamma_R$.

From Eq. (3.16), it is apparent that the separatrix shifts towards lower γ as $\gamma_R(z)$ decreases. In other words, the bucket descends together with the resonant particle in the (ψ,γ) space. This process is known as *bucket deceleration*, and is shown in Fig. 3.2.

Bucket deceleration plays an important role in the energy extraction beyond the initial saturation. During the bucket deceleration, particles trapped in the bucket are carried by the bucket towards lower γ. As these trapped particles decrease in γ, energy is extracted from them and transferred to the optical field, due to the principle of energy conservation.

As discussed in Section 3.6, the resonant particle is stationary with respect to the bucket. In the (ψ,γ) space, therefore, the bucket descends at the same rate $d\gamma_R/dz$ as the resonant particle.

According to Eq. (3.3), $d\gamma_R/dz$ scales with $\sin\psi_R$. In other words, the choice of the resonant phase ψ_R influences the rate at which the bucket descends. Within the range $0<\psi_R<\pi/2$, a larger ψ_R yields a more negative $d\gamma_R/dz$, and hence a more rapid descension.

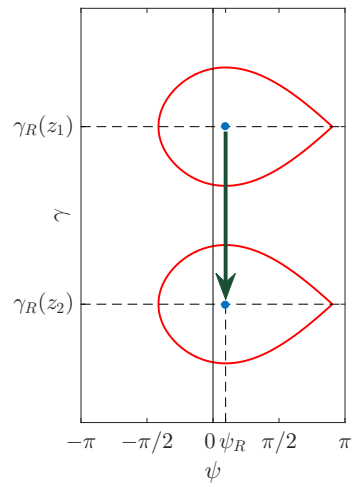

Figure 3.2. *Bucket deceleration.*

3.8 Bucket size

The amount of energy extracted from the electron beam depends on the number of particles trapped in the bucket. Meanwhile, the bucket's capacity to trap particles depends on its size. This begs the question: what determines the bucket size?

It turns out that the bucket size is influenced by the choice of the resonant phase ψ_R. This is evidenced by Fig. 3.3, which shows the separatrix (3.16) for five different ψ_R values. For each separatrix, the resonant particle is indicated by a dot of the same colour. An obvious observation is that as ψ_R increases from 0 to $\pi/3$, the bucket shrinks in both width and height.

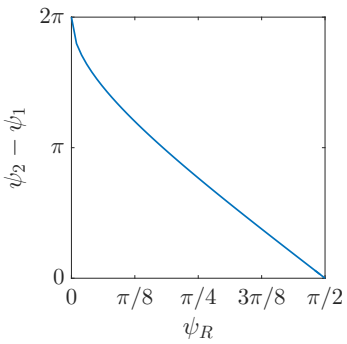

Figure 3.4. *The bucket width $\psi_2 - \psi_1$ as a function of ψ_R.*

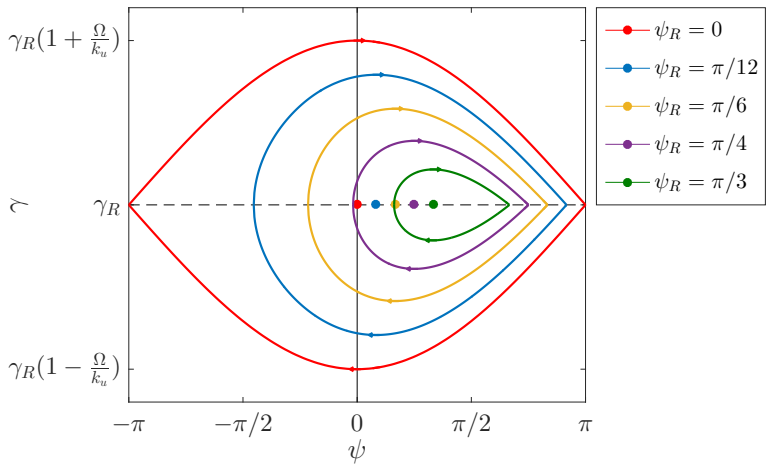

Figure 3.3. *The separatrix equation (3.16) is plotted for five different ψ_R values. The area enclosed by the separatrix is the ponderomotive bucket, which shrinks as ψ_R increases from 0 to $\pi/3$.*

Following Ref. [15], we analyse the dependence of the bucket's width, height and area on ψ_R.

3.8.1 Bucket width

Suppose ψ_1 and ψ_2 are the left bound and the right bound of the bucket, respectively [see Fig. 3.1(a)]. The bucket width is then given by the difference $\psi_2 - \psi_1$.

The right bound ψ_2 corresponds to the local maximum of the potential well in Fig. 3.1(b):

$$\psi_2 = \pi - \psi_R. \tag{3.17}$$

The left bound ψ_1 can be obtained by setting $\gamma_\pm = \gamma_R$ and $\psi = \psi_1$ in Eq. (3.16). This results in the transcendental equation

$$\cos\psi_1 + \cos\psi_R - (\pi - \psi_R - \psi_1)\sin\psi_R = 0, \tag{3.18}$$

which needs to be solved numerically.

The bucket width $\psi_2 - \psi_1$ is shown in Fig. 3.4 as a function of ψ_R. As ψ_R increases from 0 to $\pi/2$, the bucket width $\psi_2 - \psi_1$ decreases monotonically.

For an untapered undulator line ($\psi_R = 0$), we have $\psi_2 - \psi_1 = 2\pi$, meaning that the bucket has a full width of one radiation wavelength. In the case of $\psi_R = \pi/2$, we have $\psi_2 - \psi_1 = 0$, meaning that the bucket vanishes.

In the range $\pi/2 < \psi_R < \pi$, we have $\psi_2 - \psi_1 < 0$. However, a negative bucket width does not have any physical meaning. We therefore ignore this range of ψ_R.

3.8.2 Bucket height

In Eq. (3.16), the maximum γ value of the bucket is $\gamma_+(\psi_R)$, and the minimum γ value of the bucket is $\gamma_-(\psi_R)$. The bucket height is therefore given by

$$\gamma_+(\psi_R) - \gamma_-(\psi_R) = \frac{2\Omega\gamma_R}{k_u}\Gamma(\psi_R), \tag{3.19}$$

where

$$\Gamma(\psi_R) \equiv \sqrt{\cos\psi_R - \left(\frac{\pi}{2} - \psi_R\right)\sin\psi_R}\,. \tag{3.20}$$

The ψ_R dependence of the bucket height is given by the function $\Gamma(\psi_R)$, which is plotted in Fig. 3.5. The function $\Gamma(\psi_R)$ equals one when $\psi_R = 0$, and equals zero when $\psi_R = \pi/2$. As ψ_R increases from 0 to $\pi/2$, the function $\Gamma(\psi_R)$ decreases monotonically.

In the range $\pi/2 < \psi_R < \pi$, the function $\Gamma(\psi_R)$ becomes purely imaginary. We therefore ignore this range of ψ_R.

According to Eq. (3.19), the bucket height depends on Ω, in addition to ψ_R. According to Eq. (2.36), Ω depends on the undulator parameter K and the optical field amplitude E_0.

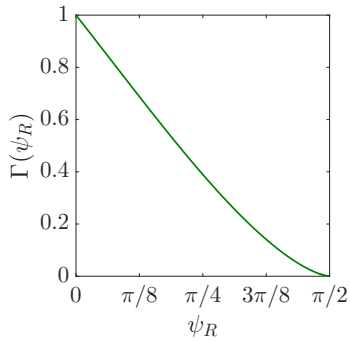

Figure 3.5. *The bucket height function* $\Gamma(\psi_R)$.

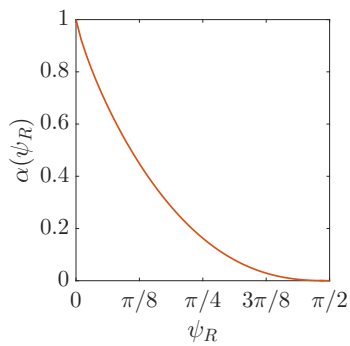

Figure 3.6. *The bucket area function* $\alpha(\psi_R)$.

3.8.3 Bucket area

The bucket area is a consequence of both the bucket width and the bucket height. Mathematically, the bucket area can be obtained by the integral

$$A_\Lambda = \int_{\psi_1}^{\psi_2} [\gamma_+(\psi) - \gamma_-(\psi)]\,d\psi = \frac{8\Omega\gamma_R}{k_u}\alpha(\psi_R), \tag{3.21}$$

where

$$\alpha(\psi_R) \equiv \frac{\sqrt{2}}{8}\int_{\psi_1}^{\psi_2} [\cos\psi_R + \cos\psi - (\pi - \psi_R - \psi)\sin\psi_R]^{1/2}\,d\psi. \tag{3.22}$$

The ψ_R dependence of the bucket height is given by the function $\alpha(\psi_R)$, which is plotted in Fig. 3.6. The function $\alpha(\psi_R)$ equals one when $\psi_R = 0$, and equals zero when $\psi_R = \pi/2$. As ψ_R increases from 0 to $\pi/2$, the function $\alpha(\psi_R)$ decreases monotonically.

In the range $\pi/2 < \psi_R < \pi$, we have $\alpha(\psi_R) < 0$. As a negative bucket area has no physical meaning, we ignore this range of ψ_R. In other words, ψ_R is now restricted to the range $0 \le \psi_R \le \pi/2$.

Again, Eq. (3.21) shows that the bucket area depends on Ω, in addition to ψ_R.

3.9 Modification to the KMR model

In an FEL with a tapered undulator line, an effective energy extraction beyond the initial saturation relies on two factors. First, the bucket needs to have a sufficiently large size, so as to trap a large number of particles. Second, the bucket needs to decelerate rapidly enough, so as to carry the trapped particles towards low energies.

Both factors depend on the choice of the resonant phase ψ_R, which is restricted to the range $0 \leq \psi_R \leq \pi/2$. As seen in Section 3.7, the larger is ψ_R, the more rapid is the bucket deceleration. As seen in Section 3.8, the larger is ψ_R, the smaller is the bucket area.

Thus, there is a conflict between the two factors. When choosing the resonant phase ψ_R, a more rapid bucket deceleration results in a smaller bucket area, and a larger bucket area results in a slower bucket deceleration. Hence, the optimization of the undulator taper requires a good balance between these two conflicting factors.

The search for the good balance provides a motivation for modifying the KMR model, and this is done in Paper I. In the modified model, the resonant phase ψ_R is no longer constant. Instead, it increases monotonically with z.

As a result, ψ_R is smaller upstream and larger downstream. At small z, we maintain a large bucket area at the cost of a slower bucket deceleration. At large z, we sacrifice the bucket area for a more rapid bucket deceleration. A detailed justification of this modification is provided in Section II D of Paper I.

Upon the modification, the coordinates (ψ_R, γ_R) of the resonant particle are subject to the following constraints:

$$\gamma_R(z) = \sqrt{\frac{\lambda_u}{2\lambda}\left[1+\frac{K^2(z)}{2}\right]}, \tag{3.23}$$

$$\psi_R(z) = \frac{\pi}{2}\left(\frac{z}{L_d}\right)^n. \tag{3.24}$$

Here n and L_d are positive real numbers to be chosen.

n is the degree of z, and does not have to be an integer. But for simplicity, one can choose $n = 1$ as in Section II E of Paper I, so that ψ_R increases *linearly* with z.

L_d is known as the *detrapping length*. At $z = L_d$, the resonant phase ψ_R reaches $\pi/2$. The bucket area then becomes zero, and total detrapping occurs. Adjusting L_d allows us to control the rate at which ψ_R increases. Note that it is possible to choose an L_d that is larger than the total length of the undulator line.

3.10 The KMR methods

The KMR model can serve as a method to optimize the taper profile. Given the constraints on the resonant particle, $K(z)$ is computed stepwise along the undulator line, with some small step size Δz.

First, we substitute Eq. (3.23) into Eq. (3.3), to eliminate the variable γ_R. This yields

$$\frac{dK}{dz} = -\frac{2e}{m_e c^2}\frac{\lambda}{\lambda_w} f_B(z) E_0(z) \sin[\psi_R(z)]. \tag{3.25}$$

Next, we assume a small step size Δz, and make the approximation $dz \approx \Delta z$, so that

$$K(z+\Delta z) = K(z) - \frac{2e}{m_e c^2}\frac{\lambda}{\lambda_w} f_B(z) E_0(z) \sin[\psi_R(z)]\Delta z. \tag{3.26}$$

Using Eq. (3.26), the required K value for each step can be computed iteratively. Once the values of K, f_B, E_0, ψ_R at z are known, the value of K at $z+\Delta z$ can be obtained.

In Eq. (3.26), $\psi_R(z)$ is a function to be chosen. With a constant ψ_R as in Eq. (3.2), the method is referred to as the *ordinary KMR method*. With $\psi_R(z)$ modified as in Eq. (3.24), the method is referred to as the *modified KMR method*.

In order to use Eq. (3.26), we also need the initial values of the variables. In particular, $K(0)$ is chosen to be in resonance with the initial energy of the electron beam, and $f_B(0)$ can be deduced from $K(0)$ through Eq. (2.9).

$E_0(0)$ is the field amplitude of the seed radiation. In the case of SASE, the effective shot noise amplitude can be used instead. In each step, the value of E_0 can be obtained from numerical simulation.

In Section III of Paper I, the variable a_w is used instead of K. The two variables are simply off by a factor of $\sqrt{2}$ [see Eq. (2.8)].

3.11 Departure from the ideal case

In Paper I, both the ordinary KMR method and the modified KMR method are applied to two cases in numerical simulation. The results show that the modified KMR method is capable of delivering a higher radiation power than the ordinary KMR method. This indicates that the modification to the KMR model opens up the possibility of a further enhancement in FEL efficiency beyond the original model.

In the cases studied in Paper I, the undulator line is continuous, with no drift sections. With a relatively small step size of $\Delta z = 0.5$ m, the taper profile $K(z)$ is a smooth and continuous function.

Paper II departs from this ideal scenario, and considers a more realistic undulator line. The undulator line consists of individual undulator segments, separated by drift sections. Each undulator segment has a length of 2.5 m, and each drift section has a length of 0.8 m. This introduces to two limitations into the picture.

First, within each undulator segment, the undulator parameter K is uniform. The K value no longer changes continuously. Instead, it changes only after every undulator segment. The segment length

sets a limit on the rate at which K decreases, and hence a limit on the rate at which the bucket descends in the (ψ,γ) space.

Second, during the FEL interaction, the diffraction of the optical beam is counteracted by the phenomenon of optical guiding [20]. In the drift sections, there is no FEL interaction, and hence no optical guiding. As the optical beam diffracts in free space, the on-axis field strength E_0 decreases. This can cause particle detrapping [21].

In Paper II, these limitations are included in the numerical simulations, and the KMR methods are applied in the presence of these limitations. With these limitations, an overall reduction of radiation power from the ideal case is inevitable.

Furthermore, Paper II progresses from steady-state simulations to time-dependent simulations. An important difference between the two is that the latter includes the time-dependent effect of sideband instability [15].

The origin of sideband instability is the synchrotron oscillations during the FEL interaction. The oscillations give rise to a longitudinal modulation of amplitude and phase in the optical pulse. The modulation manifests itself in the optical spectrum as sidebands at parasitic wavelengths.

With sideband instability, the time-dependent simulations show an overall reduction of radiation power from the steady-state simulations. When applying the KMR methods, the optimal taper in the time-dependent simulation is different from the optimal taper in the steady-state simulation.

When going from steady-state to time-dependent in the ordinary KMR method, the optimal ψ_R decreases (see Paper II). Similarly, when going from steady-state to time-dependent in the modified KMR method, the optimal L_d increases (see Paper II), which corresponds to an overall decrease in the range of ψ_R.

In the (ψ,γ) space, a smaller ψ_R leads to a less rapid bucket deceleration (see Section 3.7) and a larger bucket area (see Section 3.8). This implies that in the presence of time-dependent effects, it is preferable to maintain a relatively large bucket area at the expense of slowing down the bucket deceleration. This trade-off can be explained by the fact that sideband instability constitutes an additional source of particle detrapping [21].

3.12 Empirical optimization at FLASH2

In Paper III, an empirical optimization of undulator tapering is performed on a real FEL, namely, the FLASH2 facility [22] at the Deutsches Elektronen-Synchrotron (DESY) in Hamburg, Germany.

FLASH2 contains 12 variable-gap undulator modules, each with a length of 2.5 m. Between every two modules, there is a drift section of 0.8 m for beam focusing, trajectory correction, phase shifting and diagnostics etc.

Within each module, the undulator parameter is uniform. Thus, the undulator parameter in each module is given by a single value K_m, where $m \in \{1,2,...,12\}$. The taper profile is defined by twelve numbers: $K_1, K_2, ..., K_{12}$.

The empirical optimization is conducted using the multidimensional method, which has been demonstrated in numerical simulations by Refs. [21, 23]. In this method, the optimal taper profile is obtained by scanning over a three-dimensional parameter space, consisting of the taper order d, the start module n and the taper amplitude $\Delta K/K$. The ansatz for the taper profile is

$$K_m = \begin{cases} K & \text{for } 1 \le m < n \\ K\left[1-\left(\frac{\Delta K}{K}\right)\left(\frac{m-n+1}{12-n+1}\right)^d\right] & \text{for } n \le m \le 12. \end{cases} \tag{3.27}$$

Here K is the *initial* undulator parameter, in resonance with the initial energy of the electron beam. The undulator parameter remains at the initial value K from modules 1 to $n-1$, and decreases in steps from module n onwards. The taper order d equals 1 for linear tapering, and 2 for quadratic tapering. The taper amplitude $\Delta K/K$ is defined such that the undulator parameter of the last module is $K_{12} = K - \Delta K$.

The parameters d, n and $\Delta K/K$ are scanned for the highest optical pulse energy at the exit of the 12th undulator module. The optical pulse energy is measured and cross-checked using two devices: the micro-channel plate (MCP) detector [24] and the gas-monitor detector (GMD) [25].

After the completion of the experiment, the same optimization method is repeated in numerical simulation for comparative purposes (see Section 3 of Paper III). The simulation gives the same optimal taper profile as the experiment does. In both cases, the optimal taper is given by the point $(d, n, \Delta K/K) = (2, 7, 0.06)$ in the parameter space.

However, there are discrepancies between the experiment and the simulation. For instance, the optical pulse energies are systematically lower in the experiment than in the simulation. Paper III concludes by excluding a number of otherwise possible causes of the discrepancies, such as the deviations of the electron beam parameters, the drift of the machine, shot-to-shot variation and wakefield effects. A thorough understanding of the discrepancies would require further investigations by means of both experiment and simulation. In particular, the experimental investigation would require additional beam time.

CHAPTER 4

PHASE JUMP METHOD

This chapter introduces the phase jump method, and provides the background knowledge for Paper IV.

4.1 What is the phase jump method?

In a free-electron laser, a *phase jump* refers to an alteration of the relative phase between the electron beam and the co-propagating optical wave.

Phase jumps can be implemented using *phase shifters*. A conventional phase shifter is a compact chicane, made up of three or four dipole magnets. In an undulator line made up of discrete segments, the phase shifters can be installed in the drift sections between the segments, as shown in Fig. 4.1.

The *phase jump method* is a technique for the enhancement of the FEL efficiency. The essence is to apply appropriate phase jumps along the undulator line, so as to sustain the energy extraction from the electron beam (and hence the growth in optical power) beyond the initial saturation. The technique was first demonstrated in numerical simulation by Varfolomeev et al. [26].

An important goal of the phase jump method is to optimize the phase jumps, and maximize the enhancement in the FEL efficiency. To this end, a study by Ratner et al. [27] exploits the mathematical equivalence of phase jumps and undulator tapering, and uses a pre-optimized taper to deduce the corresponding phase jumps.

To advance the understanding of the phase jump method, a new physics model is developed in this thesis, particularly in Paper IV. The new model is independent of the undulator tapering model, and eliminates the need to deduce the phase jumps mathematically from a pre-optimized taper. Moreover, the new model reveals the potential of the phase jump method to suppress the sidebands in the optical spectrum, thereby increasing the spectral purity of the FEL.

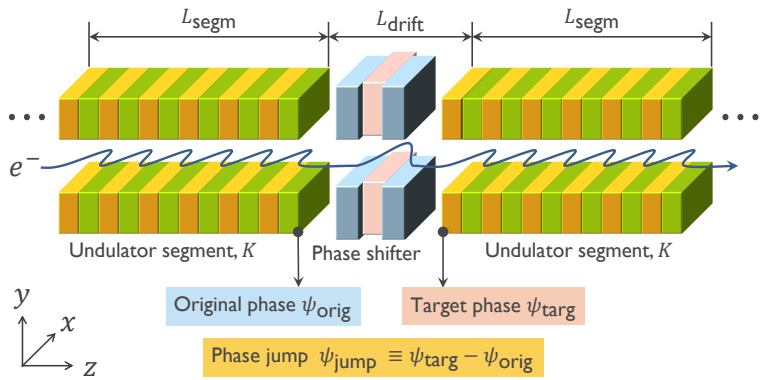

Figure 4.1. *Schematic diagram showing two of the undulator segments and the drift section in between. The phase shifter in the drift section can increase the electron path length, thus adjusting the relative phase between the electron beam and the optical wave. Focusing magnets, corrector magnets and diagnostics instruments are also commonly installed in drift sections, but they are not shown in this diagram.*

4.2 Phase definitions

In the analysis of phase jumps, it is convenient to consider the phase of an electron relative to the nearest ponderomotive bucket. We therefore use the phase variable ψ defined in Eq. (2.11), and restrict ψ to the range $-\pi \le \psi \le \pi$.

Figure 4.1 shows a phase shifter in the drift section between two undulator segments. For the purpose of specifying the phase jump, we are not concerned about the phase anywhere in the middle of the drift section. This is because the FEL energy extraction takes place in the undulator segments, and not the drift section.

Instead, we are concerned about the phase difference between the start point and the end point of the drift section. At the start point of the drift section, we define the value $\psi = \psi_{orig} \in [-\pi, \pi]$ as the *original phase*. At the end point of the drift section, we define the value $\psi = \psi_{targ} \in [-\pi, \pi]$ as the *target phase*.

For every drift section, the original phase is a given quantity, and the target phase is to be set by adjusting the phase shifter. Upon setting the target phase, the *phase jump* is given by

$$\psi_{jump} = \psi_{targ} - \psi_{orig} \in [-2\pi, 2\pi]. \tag{4.1}$$

Note that $\psi_{jump} = 0$ does *not* mean switching off or removing the phase shifter. Instead, it means configuring the phase shifter such that the phase at the start point of the drift section is *preserved* at the end point of the drift section. Without the phase shifter, this preservation is not automatically achieved in general.

Note also the sign convention that a positive ψ_{jump} corresponds to shifting an electron *forward* in ψ. However, a conventional phase shifter implements the phase jump by delaying the electrons with respect to the optical beam. It can only shift electrons backward, but not forward. In practice, if the required ψ_{jump} is positive, we need to shift the electron backward to another bucket by a total phase of $2\pi n - \psi_{\text{jump}}$ for some positive integer n.

The phase jump ψ_{jump} is a consequence of the speed difference between the electron beam and the optical beam. While the optical beam travels at the speed c, the electron beam travels at some speed $v < c$. As a result, the optical beam slips ahead of the electron beam by some distance L_{slip} as they travel together across the drift section. This distance L_{slip} is called the *slippage* in the drift section, and is related to the phase jump ψ_{jump} by

$$\frac{L_{\text{slip}}}{\lambda} = \frac{2\pi n - \psi_{\text{jump}}}{2\pi}, \tag{4.2}$$

where n is a positive integer.

4.3 Role of the phase shifter

4.3.1 Without the phase shifter

Referring to Fig. 4.1, L_{segm} is the length of each undulator segment, and L_{drift} is the length of each drift section.

Without the phase shifter, both the electron beam and the optical beam would travel across the drift section in a straight line. If we let Δt be the time taken for the electron beam to travel across the drift section, then

$$L_{\text{drift}} = v\Delta t. \tag{4.3}$$

In the same time interval Δt, the optical beam has travelled further than the electron beam. We can express the distance travelled by the optical beam as

$$L'_{\text{drift}} = c\Delta t = \frac{c}{v} L_{\text{drift}} > L_{\text{drift}}. \tag{4.4}$$

The slippage in the drift section is then given by

$$L_{\text{slip}} = L'_{\text{drift}} - L_{\text{drift}} = \left(\frac{c}{v} - 1\right) L_{\text{drift}}. \tag{4.5}$$

Invoking the definition (2.10), we have

$$\begin{aligned} \gamma = \frac{1}{\sqrt{1 - v^2/c^2}} \quad &\Rightarrow \quad \frac{v^2}{c^2} = 1 - \frac{1}{\gamma^2} \\ &\Rightarrow \quad \frac{c}{v} = \left(1 - \frac{1}{\gamma^2}\right)^{-1/2} \approx \left(1 + \frac{1}{2\gamma^2}\right). \end{aligned} \tag{4.6}$$

Substituting Eq. (4.6) into Eq. (4.5) yields

$$L_{\text{slip}} = \frac{L_{\text{drift}}}{2\gamma^2}. \tag{4.7}$$

The expression (4.7) gives the slippage in the drift section in the *absence* of the phase shifter. This slippage can be translated into the phase jump ψ_{jump} using Eq. (4.2).

In Eq. (4.7), the slippage is determined solely by the length L_{drift} of the drift section and the energy variable γ of the electron beam. However, L_{drift} is usually fixed, and cannot be changed without physically displacing the undulator segments. Besides, we have no direct control over γ in each drift section. Thus, there is no easy way to adjust L_{slip}, and hence ψ_{jump}, in each drift section.

4.3.2 With the phase shifter

In order to implement the phase jump method, we need to be able to adjust the value of ψ_{jump} for every drift section. This necessitates the use of phase shifters.

With the phase shifter in Fig. 4.1, the electron beam is deflected by the dipole magnets of the phase shifter, and takes a detour from the original straight-line trajectory.

The detour increases the electron path length in the drift section by some amount ΔL. In principle, ΔL can be adjusted by changing the magnetic field strength B_0 of the phase shifter from the control room.

While the electron beam takes the detour, the optical beam is not affected by the magnetic field of the phase shifter, as photons do have any electric charge.

As a result, the detour of the electron beam makes an additional contribution to the slippage in the drift section. The slippage in the drift section can then be written as

$$L_{\text{slip}} = \frac{L_{\text{drift}}}{2\gamma^2} + \Delta L(B_0). \tag{4.8}$$

Again, this slippage can be translated into ψ_{jump} using Eq. (4.2). The important message here is that the magnetic field strength B_0 of the phase shifter serves as an independent knob, making it easier to adjust the value of ψ_{jump} for individual drift sections.

4.4 Analysis of a phase shifter

In Eq. (4.8), the function $\Delta L(B_0)$ controls the phase jump ψ_{jump}. In this section, we analyse the electron beam path in a phase shifter, and determine the function $\Delta L(B_0)$. As a example, we consider a phase shifter with the configuration shown in Fig. 4.2.

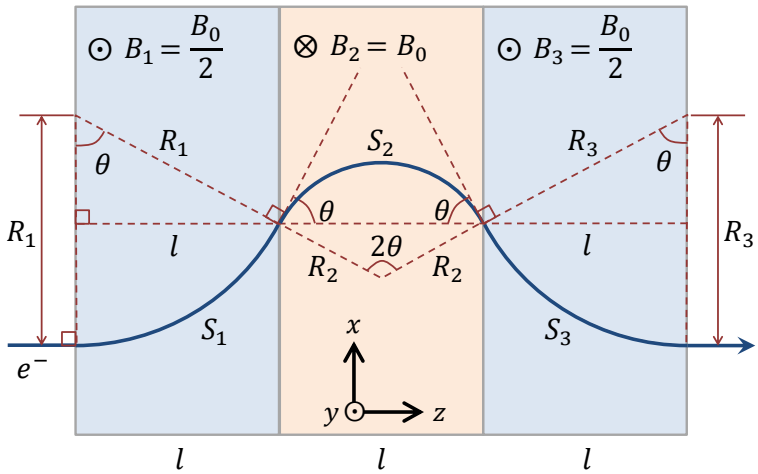

Figure 4.2. *Electron beam path in a phase shifter which comprises three dipole magnets of equal length l.*

In general, a phase shifter can consist of either three or four dipole magnets, and there can be a small drift space between adjacent magnets. In our example, the phase shifter consists of three dipole magnets, and there is no drift space in between them (see Fig. 4.2). Furthermore, the three magnets have the same length l, and a fixed magnetic field strength ratio of $-1/2:+1:-1/2$.

While the *ratio* of the magnetic field strengths is fixed, the value of B_0 (see Fig. 4.2) is adjustable. For an electromagnet, B_0 can be adjusted by changing the current through the coil. For a permanent magnet, B_0 can be adjusted by mechanically changing the gap height between the magnetic poles.

In the phase shifter, the electron beam takes a detour from the original straight-line path. Along the detour, the electron path length is $S_1+S_2+S_3$; along the original straight-line path, the electron path length is $3l$ (see Fig. 4.2). Thus,

$$\Delta L = S_1 + S_2 + S_3 - 3l. \tag{4.9}$$

In order to relate ΔL to B_0, we consider the bending radii R_1, R_2 and R_3 in the three magnets:

$$\frac{1}{R_1} = \frac{e\,B_1}{p} \quad \Rightarrow \quad R_1 = \frac{2p}{e\,B_0} \equiv R, \tag{4.10}$$

$$\frac{1}{R_2} = \frac{e\,B_2}{p} \quad \Rightarrow \quad R_2 = \frac{p}{e\,B_0} \equiv \frac{R}{2}, \tag{4.11}$$

$$\frac{1}{R_3} = \frac{e\,B_3}{p} \quad \Rightarrow \quad R_3 = \frac{2p}{e\,B_0} \equiv R. \tag{4.12}$$

In the expressions for the bending radii R_1, R_2 and R_3,

$$p = m_e c \sqrt{\gamma^2 - 1} \tag{4.13}$$

is the momentum of the electron beam. The bending radii are related to the arc lengths S_1, S_2 and S_3 as follows:

$$S_1 = R_1 \theta = R\theta, \tag{4.14}$$
$$S_2 = R_2 \times 2\theta = R\theta, \tag{4.15}$$
$$S_3 = R_3 \theta = R\theta. \tag{4.16}$$

Here the angle θ can be related to the constant l by considering the right-angled triangle in the first magnet (see Fig. 4.2):

$$\sin\theta = \frac{l}{R_1} = \frac{l}{R} \quad \Rightarrow \quad \theta = \arcsin\left(\frac{l}{R}\right). \tag{4.17}$$

As a result, Eq. (4.9) can be rewritten as

$$\Delta L = 3R\theta - 3l = 3R\arcsin\left(\frac{l}{R}\right) - 3l. \tag{4.18}$$

For a compact phase shifter, $l \ll R$. We can therefore approximate the arcsin function by the first two non-zero terms in its Taylor expansion:

$$\Delta L \approx 3R\left(\frac{l}{R} + \frac{l^3}{6R^3}\right) - 3l = \frac{l^3}{2R^2}. \tag{4.19}$$

Invoking Eqs. (4.10) and (4.13) yields

$$\begin{aligned} \Delta L(B_0) &= \frac{l^3}{2}\left(\frac{eB_0}{2p}\right)^2 \\ &= \frac{e^2 l^3 B_0^2}{8 m_e^2 c^2 (\gamma^2 - 1)}. \end{aligned} \tag{4.20}$$

Equation (4.20) defines the function $\Delta L(B_0)$. It shows how the electron path length in the drift section can be influenced by the magnetic field strength of the phase shifter.

An explicit expression relating B_0 to the phase jump ψ_{jump} can be obtained by substituting (4.20) into (4.8), and then into (4.2).

4.5 Overview of the phase jump model

A new physics model of the phase jump method is developed in Paper IV. This new model advances beyond previous studies in three major aspects. First, it illustrates the energy extraction mechanism of the phase jump method. Second, it does not rely on a pre-optimized undulator taper to compute the phase jumps. Third, it opens up new possibilities to suppress the sidebands in the optical spectrum.

The model illustrates the energy extraction mechanism by describing the particle dynamics in the longitudinal phase space. At the initial saturation, microbunches are fully developed. For further energy extraction to be possible, the microbunches must continue to decelerate together, and radiate coherently. To examine the deceleration of the microbunches, the model considers an *average particle* within each microbunch (see Section II G of Paper IV).

Without undulator tapering, there is no bucket deceleration (see Section 3.7). Therefore, the phase jump method by itself cannot rely on a descending bucket to carry the particles towards lower energies. Instead, the model identifies the *microbunch deceleration cycle* (see Section II G of Paper IV) as the underlying mechanism for energy extraction beyond the initial saturation.

An important implication of the microbunch deceleration cycle is the possibility to extract energy from particles which are *out of* the bucket (see Section II J of Paper IV). Beyond the initial saturation, the model divides the energy extraction process into the *in-bucket regime* and the *out-of-bucket regime*.

By analysing the microbunch deceleration cycle, the model sets out the selection criteria for the target phase ψ_{targ} of the average particle in the in-bucket and out-of-bucket regimes. This eliminates the reliance on a pre-optimized undulator taper in the optimization of phase jumps.

In Section IV of Paper IV, the model is extended to include time-dependent effects. An important effect is sideband instability, which is a known issue for undulator tapering (see Section 3.11).

Sideband instability can draw a significant fraction of the optical power away from the optical wavelength which we intend to amplify, and channel the power to parasitic wavelengths which show up as sidebands in the optical spectrum. This degrades the spectral purity, as well as the *useful* output of the FEL.

However, the new model reveals the potential of the phase jump method to suppress the sidebands. This is detailed in Section IV D of Paper IV. In brief, the known cause [15] of sideband instability is the synchrotron oscillations of the electrons, and the principle behind the sideband suppression is that the microbunch deceleration cycle itself disrupts the synchrotron oscillations.

This new model is verified and supported by simulation studies (see Sections III and V of Paper IV).

4.6 Comparison with undulator tapering

In this section, we compare and contrast the phase jump method with undulator tapering, in terms of the features of the model and the performance in numerical simulation.

Both the phase jump method and undulator tapering enhance the FEL efficiency by overcoming the limit on the radiation power

imposed by the initial saturation. For both techniques, the general principle is to bring a significant fraction of particles towards lower energies after the initial saturation. As these particles decelerate, energy is transferred to the optical field, due to the principle of energy conservation.

However, the phase jump model and the taper model considered in the thesis do differ in a number of aspects:

(i) **Representative particle**
The taper model traces the *resonant particle*, which defines the centroid of the ponderomotive bucket. The phase jump model traces the *average particle*, which reflects the average energy and phase within the microbunch.

(ii) **Knob to turn**
In the taper model, we control the undulator parameter K, to move the resonant particle vertically in the (ψ,γ) space. In the phase jump model, we control the phase jump ψ_{jump}, to move the average particle horizontally in the (ψ,γ) space.

(iii) **Particle deceleration mechanism**
While the taper model relies on *bucket deceleration*, the phase jump model relies on the *microbunch deceleration cycle*.

(iv) **Rate of particle deceleration**
In the taper model, the rate of particle deceleration is determined by $d\gamma_R/dz$ (see Section 3.7). In the phase jump model, the rate of particle deceleration is determined by $d\gamma/d\psi$ (see Section II J 1 of Paper IV).

(v) **Motion of the bucket**
In the taper model, the bucket descends and shrinks. In the phase jump model, the bucket neither descends nor shrinks.

(vi) **Energy extraction outside the bucket**
In the taper model, detrapped particles generally do not participate in the energy extraction. In the phase jump model, there is an *out-of-bucket regime*, which enables energy extraction from particles outside the bucket.

(vii) **Mechanism of final saturation**
In the taper model, the main causes of the final saturation are the weakening of refractive guiding and the detrapping of particles. In the phase jump model, the main causes are $d\gamma/d\psi \to 0$ and $\Delta\psi_{\text{segm}} > \pi$ (see Section II K of Paper IV).

(viii) **Sideband suppresion**
The phase jump model reveals the possibility to use the phase jumps for suppressing the sidebands in the optical spectrum (see Section IV D of Paper IV). This feature is not found in the taper model.

In Section V of Paper IV, a simulation study is conducted to compare the performances of the phase jump method and undulator tapering. Under the same initial conditions, the phase jumps and the taper are separately optimized.

Upon reaching the final saturation, the optical pulse energy attained by the optimized taper is about three times higher than that attained by the optimized phase jumps. This shows that the optimized taper is capable of extracting a larger fraction of the electron beam energy.

However, the phase jump method is more effective in sideband suppression. This means that the optimized phase jumps channel a smaller fraction of the optical power to the parasitic wavelengths, and hence a larger fraction to the central wavelength that we actually intend to amplify.

Upon reaching the final saturation, the *absolute* spectral power at the central wavelength is almost the same for both the optimized taper and the optimized phase jumps. If we define the *useful* output of the FEL as the spectral power at the central wavelength, then the optimized taper and the optimized phase jumps are almost equally as efficient.

Now that we have seen the merits of each technique, it is logical to think of the possibility to combine the strengths of the two techniques. The combined use of undulator tapering and phase jumps is beyond the scope of this thesis, but is discussed briefly in Section VI of Paper IV.

CHAPTER 5

SUMMARY AND OUTLOOK

This thesis investigates two techniques for enhancing the efficiency of a free-electron laser, namely, undulator tapering and the phase jump method. The former has been introduced in Chapter 3, and the latter has been introduced in Chapter 4. The research on these topics are presented in the papers at the end of this book.

The research on undulator tapering is built upon the KMR model (see Section 3.3). In Paper I, a modification to the KMR model is proposed, and is justified by the particle trapping consideration and the bucket deceleration consideration.

Based on the KMR model and its modified version, the "ordinary KMR method" and "modified KMR method" are developed for the optimization of the undulator taper (see Section 3.10). The methods are then demonstrated in numerical simulations.

An important conclusion of Paper I is that the modification to the KMR model opens up the possibility of a further enhancement in FEL efficiency beyond the original model.

Having established the KMR methods in Paper I, Paper II progresses beyond the ideal scenario. The simulation studies account for the limitations on the tapering technique (see Section 3.11) imposed by the uniformity of the individual undulator segments and the optical beam diffraction in the drift sections. The studies also include time-dependent effects. The results affirm that the KMR methods remain valid under the far-from-ideal circumstances.

Paper III presents an empirical study of taper optimization at a real FEL, namely, the FLASH2 facility at DESY. The empirical results are then compared against numerical simulations. While the simulation yields the same optimal taper as the experiment, there are discrepancies between the simulation and the experiment in the absolute optical pulse energies. Paper III concludes by excluding a number of otherwise possible causes of the discrepancies. However, a thorough understanding of the discrepancies would require additional beam time.

Switching gear from the topic of undulator tapering, Paper IV develops a new physics model for the phase jump method. As explained in Section 4.5, this new model advances beyond previous studies in three major aspects. First, it illustrates the energy extraction mechanism of the phase jump method. Second, it does not rely on a pre-optimized undulator taper to compute the phase jumps. Third, it opens up new possibilities to suppress the sidebands in the optical spectrum.

Finally, Paper V concerns the SPF at the MAX IV Laboratory here in Lund, Sweden. While the SPF is not an FEL, the paper gives a preliminary study of the possibility to operate the SPF as a simple FEL, for the research and development of future FELs at MAX IV. The paper also touches on the topic of single-step undulator tapering.

In this thesis, the model-based studies of undulator tapering and the phase jump method enable us to compare and contrast the two techniques (see Section 4.6). Beyond this thesis, a possible topic of further study is the combined use of the two techniques, as it is briefly discussed in Section VI of Paper IV. By combining the strengths of both techniques, there is potential for attaining an even further enhancement in FEL efficiency.

REFERENCES

[1] F. Bencivenga et al., "Coherent and transient states studied with extreme ultraviolet and x-ray free electron lasers: present and future prospects", Advances in Physics **63**, 327 (2015).

[2] J. Ullrich, A. Rudenko, R. Moshammer, "Free-electron lasers: new avenues in molecular physics and photochemistry", Annual Review of Physical Chemistry **63**, 635 (2012).

[3] R. Neutze, G. Brändén, G. F. Schertler, "Membrane protein structural biology using x-ray free electron lasers", Current Opinion in Structural Biology **33**, 115 (2015).

[4] M. A. Mackanos et al., "Corneal ablation using the pulse stretched free electron laser", Proceedings of SPIE 5688, Ophthalmic Technologies XV, 177 (2005).

[5] J. M. J. Madey, "Stimulated emission of Bremsstrahlung in a periodic magnetic field", J. Appl. Phys. **42**, 1906 (1971).

[6] L. R. Elias et al., "Observation of stimulated emission of radiation by relativistic electrons in a spatially periodic transverse magnetic field", Phys. Rev. Lett. **36**, 717 (1976).

[7] D. A. G. Deacon et al., "First operation of a free-electron laser", Phys. Rev. Lett. **38**, 892 (1977).

[8] C. Pellegrini, "The history of x-ray free electron lasers", European Phys. J. H **37**, 659 (2012).

[9] F. Curbis et al., "Towards an x-ray FEL at the MAX IV Laboratory", Proceedings of FEL 2014, Basel, Switzerland, TUP080.

[10] S. Werin et al., "Short Pulse Facility for MAX-lab", Nucl. Instr. Meth. Phys. Res., Sect. A **601**, 98 (2009).

[11] H. N. Chapman et al., "Femtosecond x-ray protein nanocrystallography", Nature (London) **470**, 73 (2011).

[12] N. M. Seibert et al., “Single mimivirus particles intercepted and imaged with an x-ray laser”, Nature (London) **470**, 78 (2011).

[13] Z. Huang, K.-J. Kim, “Review of x-ray free-electron laser theory”, Phys. Rev. ST Accel. Beams **10**, 034801 (2007).

[14] M. Xie, “Exact and variational solutions of 3D eigenmodes in high gain FELs”, Nucl. Instr. Meth. Phys. Res., Sect. A **445**, 59 (2000).

[15] N. M. Kroll, P. L. Morton, M. N. Rosenbluth, “Free-electron lasers with variable parameter wigglers”, IEEE J. Quantum Electronics **17**, 1436 (1981).

[16] D. Prosnitz, A. Szoke, V. K. Neil, “High-gain, free-electron laser amplifiers: Design considerations and simulation”, Phys. Rev. A **24**, 1436 (1981).

[17] P. Schmüser, M. Dohlus, J. Rossbach, in *Ultraviolet and Soft X-Ray Free-Electron Lasers: Introduction to Physical Principles, Experimental Results, Technological Challenges*, (Springer, Berlin, Germany, 2008), p.29.

[18] E. T. Scharlemann, in *High Gain, High Power Free Electron Lasers: Physics and Application to TeV Particle Acceleration*, edited by R. Bonifacio, L. De Salvo Souza and C. Pellegrini (Elsevier, Amsterdam, Netherlands, 1989), p.95.

[19] C. A. Brau, in *Free-Electron Lasers*, (Academic Press, Boston, USA, 1990), p.236.

[20] E. T. Scharlemann et al., “Optical guiding in a free-electron laser”, Phys. Rev. Lett. **54**, 1925 (1985).

[21] Y. Jiao et al., “Modeling and multidimensional optimization of a tapered free electron laser”, Phys. Rev. ST Accel. Beams **15**, 050704 (2012).

[22] S. Schreiber, B. Faatz, “The free-electron laser FLASH”, High Power Laser Science and Engineering **3**, e20 (2015).

[23] C. Emma et al., “High efficiency, multiterawatt x-ray free electron lasers”, Phys. Rev. Accel. Beams **19**, 020705 (2016).

[24] L. Bittner et al., “MCP-based photon detector with extended wavelength range for FLASH”, Proceedings of FEL 2007, Novosibirsk, Russia, WEPPH007.

[25] K. Tiedtke et al., “Gas detectors for x-ray lasers”, J. Appl. Phys. **103**, 094511 (2008).

[26] A. A. Varfolomeev, T. V. Yarovoi, P. V. Bousine, “Possible enhancement of SASE FEL output field intensity induced by local phase jump”, Nucl. Instrum. Methods Phys. Res., Sect. A **407**, 296 (1998).

[27] D. Ratner, Z. Huang, A. Chao, “Enhancing FEL power with phase shifters”, Proceedings of FEL 2007, Novosibirsk, Russia, MOPPH023.

Papers

COMMENTS ON THE PAPERS

I **Model-based optimization of tapered free-electron lasers**
In this paper, the Kroll-Morton-Rosenbluth (KMR) model of undulator tapering is reviewed and modified. The modified model is applied to numerical simulations, to optimize the undulator taper for the highest FEL efficiency. The results show that the modification to the model leads to a further increase in FEL efficiency. The paper is entirely my own work, and the co-authors serve as advisories.

II **Further studies of undulator tapering in x-ray FELs**
This paper is a progression beyond Paper I and a preparation for Paper III. The paper departs from the ideal case, adapts the KMR model to a segmented undulator line, and accounts for time-dependent effects. The simulation studies are conducted on a case of the FLASH2 facility, so as to lay down the theoretical foundations for the experimental work at FLASH2. The paper is entirely my own work, and the co-authors serve as advisories.

III **Empirical optimization of undulator tapering at FLASH2 and comparison with numerical simulations**
This paper documents the experimental study of undulator tapering at the FLASH2 facility, and compares the empirical results with numerical simulations. The agreement and discrepancies between the empirical and simulation results are discussed. I collaborated with the co-authors on the experimental work in the FLASH2 control room. I subsequently performed all the simulations, and wrote the entire paper with the advice of the co-authors.

IV **Phase jump method for efficiency enhancement in free-electron lasers**
This paper develops a new physics model of the phase jump method, and supports it with numerical simulations. With the aid of the model, the phase jump method is compared and contrasted with undulator tapering. The paper is entirely my own work, and the co-authors serve as advisories.

V **FEL operation modes of the MAX IV Short Pulse Facility**
This paper concerns the Short Pulse Facility (SPF), an incoherent radiation source comprising two undulator segments. The paper explores alternative operation modes, in which the SPF functions as a simple FEL. By means of numerical simulation, single-step undulator tapering is also studied. The paper is entirely my own work, and the co-authors serve as advisories.

PAPER I

Model-based optimization of tapered free-electron lasers

A. Mak, F. Curbis, S. Werin.

Phys. Rev. ST Accel. Beams **18**, 040702 (2015).

PHYSICAL REVIEW SPECIAL TOPICS - ACCELERATORS AND BEAMS **18,** 040702 (2015)

Model-based optimization of tapered free-electron lasers

Alan Mak,* Francesca Curbis, and Sverker Werin
MAX IV Laboratory, Lund University, P.O. Box 118, SE-22100 Lund, Sweden
(Received 18 December 2014; published 23 April 2015)

The energy extraction efficiency is a figure of merit for a free-electron laser (FEL). It can be enhanced by the technique of undulator tapering, which enables the sustained growth of radiation power beyond the initial saturation point. In the development of a single-pass x-ray FEL, it is important to exploit the full potential of this technique and optimize the taper profile $a_w(z)$. Our approach to the optimization is based on the theoretical model by Kroll, Morton, and Rosenbluth, whereby the taper profile $a_w(z)$ is not a predetermined function (such as linear or exponential) but is determined by the physics of a resonant particle. For further enhancement of the energy extraction efficiency, we propose a modification to the model, which involves manipulations of the resonant particle's phase. Using the numerical simulation code GENESIS, we apply our model-based optimization methods to a case of the future FEL at the MAX IV Laboratory (Lund, Sweden), as well as a case of the LCLS-II facility (Stanford, USA).

DOI: 10.1103/PhysRevSTAB.18.040702 PACS numbers: 41.60.Cr, 41.60.Ap

I. INTRODUCTION

In a free-electron laser (FEL), the technique of tapering involves the variation of the undulator parameter along the undulator line, thereby maintaining the resonance condition as the electrons lose energy to the radiation. This can increase the output power and the energy extraction efficiency, as it has been demonstrated experimentally [1,2].

The effectiveness of this technique relies on the proper optimization of the taper profile. One example is the multidimensional scanning method [3]. Another example is the GINGER self-design taper algorithm [4], which is based on the Kroll-Morton-Rosenbluth (KMR) model [5].

In a previous work [6], we briefly presented a method based on a modification to the KMR model, which involves the manipulation of the resonant particle's phase. In this work, we elaborate on this method and examine the underlying physics in greater detail.

The knowledge about taper optimization is important for the MAX IV Laboratory in the development of an x-ray FEL [7], which is part of the laboratory's long-term strategic plan. The plan includes an extension of the MAX IV linear accelerator to 4–6 GeV, to be used as the driver of the FEL.

Using the numerical simulation code GENESIS [8], we study our taper optimization methods on a case of the future MAX IV FEL, where the electron beam energy at the entrance to the FEL is assumed to be 4 GeV.

To test our methods on a different set of parameters, we also apply the methods to a case of the LCLS-II. The case is defined in Jiao *et al.* [3], based on the design parameters at the time of its publication. We then benchmark our results against a taper profile obtained by Jiao *et al.* [3] from the GINGER algorithm [4].

In this work, the numerical simulations are performed in the steady-state mode. This allows us to focus on the effects of manipulating the resonant particle's phase. Our immediate objective is to demonstrate that our modification to the KMR model gives rise to an enhanced energy extraction efficiency. The study of time-dependent effects, such as side-band growth, is left out from the scope of this work and is to be addressed in a forthcoming article.

II. THEORY

A. Tapered FELs

The resonance condition on the central axis of a FEL is given by the equation

$$\lambda = \frac{\lambda_w}{2\gamma^2}(1 + a_w^2), \tag{1}$$

where λ is the optical wavelength, λ_w is the undulator period, and γ is the electron energy normalized to its rest energy $m_e c^2$. The properties of the undulator are characterized by the rms undulator parameter

$$a_w = \frac{K}{\sqrt{2}} \equiv \frac{e\lambda_w B_w}{2\sqrt{2}\pi m_e c^2}, \tag{2}$$

where e is the absolute value of the electron charge and B_w is the undulator field strength.

*alan.mak@maxlab.lu.se

During the energy extraction, the electrons lose energy to the optical field. For a FEL with constant a_w, the electron energy γ quickly ceases to satisfy the resonance condition and the FEL power saturates. This severely limits the energy extraction efficiency of the FEL.

To overcome this limit, one can *taper* the FEL by varying a_w as a function of the axial position z, so as to maintain the resonance condition continually as the electrons decelerate. This results in the sustained energy transfer from the electrons to the optical field beyond the initial saturation point.

The function $a_w(z)$ is the taper profile. Our aim is to optimize the taper profile, thereby maximizing the energy extraction efficiency of the tapered FEL. Our approach is to develop methods for such optimization, based on a theoretical model. This model-based approach can shed some light on the physics behind the optimization.

The FEL cases considered in this article are single-pass and seeded. Each uses planar undulators with a constant period λ_w.

B. The KMR model

The Kroll-Morton-Rosenbluth model [5] is a theoretical analysis of tapered FELs based on a one-dimensional relativistic Hamiltonian formulation. It is reviewed in Refs. [9–11].

In phase space, each particle has coordinates (ψ, γ), where γ is the energy normalized to the electron rest energy $m_e c^2$ and ψ is the phase relative to the ponderomotive potential. The essence of the KMR model is the consideration of a resonant particle, with phase space coordinates (ψ_R, γ_R) subject to certain constraints. At any z position along the undulator line, the energy of this particle remains at resonance, given by

$$\gamma_R(z) = \sqrt{\frac{\lambda_w}{2\lambda}[1 + a_w^2(z)]}. \tag{3}$$

Meanwhile, the phase of this particle remains constant along the undulator line, so that

$$\psi_R(z) = \psi_R(0) = \text{constant}. \tag{4}$$

The actual value of the constant phase is chosen by the FEL designer.

With the constraints on γ_R and ψ_R, the taper profile $a_w(z)$ is uniquely determined by the equation of motion in the longitudinal direction, namely

$$\frac{d\gamma_R}{dz} = -\frac{e}{\sqrt{2}m_e c^2}\frac{a_w(z) f_B(z) E_0(z)}{\gamma_R(z)}\sin[\psi_R(z)], \tag{5}$$

where E_0 is the optical field amplitude and

$$f_B(z) = J_0\left(\frac{a_w^2(z)}{2 + 2a_w^2(z)}\right) - J_1\left(\frac{a_w^2(z)}{2 + 2a_w^2(z)}\right) \tag{6}$$

is the Bessel factor for planar undulators.

For efficient energy transfer to the optical field, $\gamma_R(z)$ should be a monotonically decreasing function. Otherwise, the resonant particle would absorb energy from the optical field, thus reducing the power of the FEL. In other words, we need

$$\frac{d\gamma_R}{dz} < 0 \quad \text{for all } z. \tag{7}$$

This has two main consequences. According to Eq. (3), this requires $a_w(z)$ to be a monotonically decreasing function as well. According to Eq. (5), this requires $\sin\psi_R > 0$, thus leading to the restriction $0 < \psi_R < \pi$.

C. The ponderomotive bucket

In phase space, the coordinates (ψ_R, γ_R) of the resonant particle defines the stable point in the ponderomotive bucket, which is often known as the centroid. An equation for the separatrices of the bucket is derived in Ref. [5] and can be rewritten as

$$\gamma_\pm(\psi) = \gamma_R \pm \sqrt{\frac{e\lambda_w a_w f_B E_0}{2\sqrt{2}\pi m_e c^2}}[\cos\psi + \cos\psi_R - (\pi - \psi - \psi_R)\sin\psi_R]^{1/2}. \tag{8}$$

As γ_R decreases with z, the ponderomotive bucket moves together towards smaller γ values. This is known as bucket deceleration and is a feature of tapered FELs.

Particles within the bucket are said to be *trapped*. These particles follow stable orbits around the resonant particle and decelerate together with the bucket. As they decelerate, energy is transferred to the optical field. Particles falling out of the bucket are said to be *detrapped*. Once detrapped, a particle quickly moves away from the resonance condition.

It is therefore apparent that the energy extraction in a tapered FEL relies heavily on the trapping of particles in the bucket. Meanwhile, the bucket's capacity to capture particles depends on its size. Following Ref. [5], we analyze the factors that influence the bucket size.

1. Bucket width

We first concern ourselves with the width of the bucket. Let ψ_1 and ψ_2 be the minimum and maximum ψ values for the bucket. The bucket width is then given by the difference $\psi_2 - \psi_1$. The value ψ_2 can be obtained from the simple equation

$$\psi_2 = \pi - \psi_R, \tag{9}$$

while the value ψ_1 can be obtained from the transcendental equation

$$\cos\psi_1 + \cos\psi_R = (\pi - \psi_R - \psi_1)\sin\psi_R. \quad (10)$$

It is apparent that the values ψ_1 and ψ_2, hence the bucket width, are solely determined by the resonant particle's phase ψ_R. Over the range $0 < \psi_R < \pi/2$, the bucket width $\psi_2 - \psi_1$ decreases with ψ_R. At $\psi_R = \pi/2$, we have $\psi_1 = \psi_2 = \pi/2$, meaning that the bucket has zero width.

2. Bucket height

The bucket height is given by

$$\gamma_+(\psi_R) - \gamma_-(\psi_R) \propto \sqrt{a_w f_B E_0}\,\Gamma(\psi_R), \quad (11)$$

where

$$\Gamma(\psi_R) \equiv \sqrt{\cos\psi_R - \left(\frac{\pi}{2} - \psi_R\right)\sin\psi_R}. \quad (12)$$

Unlike the bucket width, the bucket height depends on a_w and E_0 in addition to ψ_R. The ψ_R dependence of the bucket height is governed by the function $\Gamma(\psi_R)$, which decreases with ψ_R for $0 < \psi_R < \pi/2$ and becomes zero when $\psi_R = \pi/2$. $\Gamma(\pi/2 < \psi_R < \pi)$ is purely imaginary.

3. Bucket area

The area of the bucket is a combination of the width and the height. Mathematically, the bucket area can be obtained by the integral

$$A_\Lambda = \int_{\psi_1}^{\psi_2} [\gamma_+(\psi) - \gamma_-(\psi)]\,d\psi \propto \sqrt{a_w f_B E_0}\,\alpha(\psi_R), \quad (13)$$

where

$$\alpha(\psi_R) \equiv \frac{\sqrt{2}}{8}\int_{\psi_1}^{\psi_2} [\cos\psi + \cos\psi_R - (\pi - \psi - \psi_R)\sin\psi_R]^{1/2}\,d\psi. \quad (14)$$

It turns out that the bucket area depends on a_w and E_0 in the same way as the bucket height does. The ψ_R dependence of the bucket area is governed by the function $\alpha(\psi_R)$, which decreases with ψ_R for $0 < \psi_R < \pi/2$ and becomes zero when $\psi_R = \pi/2$.

Choosing $\psi_R \geq \pi/2$ will result in the disappearance of the bucket and the total detrapping of particles, thus making the FEL process impossible. This further restricts the choice of ψ_R to the range $0 < \psi_R < \pi/2$. Within this range, a larger ψ_R leads to a smaller bucket area, hence a smaller trapping fraction.

D. Field equations

During the FEL process, the optical field is amplified through its interaction with the electrons. The evolution of the optical field amplitude E_0 and phase ϕ are described by the field equations, of which a derivation is provided in Ref. [9].

In the resonant particle approximation, we assume that only trapped particles participate in the interaction with the optical field and that all trapped particles have the same γ and ψ as the resonant particle. With this approximation, the evolution of E_0 can be written as

$$\frac{dE_0}{dz} = \frac{1}{\sqrt{2}c\epsilon_0} a_w(z) f_B(z) J_\Lambda(z) \frac{\sin[\psi_R(z)]}{\gamma_R(z)}, \quad (15)$$

where ϵ_0 is the permittivity of free space,

$$J_\Lambda(z) = \frac{ecN_\Lambda(z)}{\pi\sigma_{x,y}^2\lambda} \quad (16)$$

is the current density due to the trapped particles, N_Λ is the number of particles trapped, and $\sigma_{x,y}$ is the rms beam radius. Combining the field equation (15) with the equation of motion (5), we have

$$\frac{dE_0}{dz} = \frac{m_e c}{\epsilon_0 e}\frac{1}{E_0(z)} J_\Lambda(z)\left|\frac{d\gamma_R}{dz}\right| \propto \frac{1}{E_0(z)} N_\Lambda(z)\left|\frac{d\gamma_R}{dz}\right|. \quad (17)$$

This shows that the growth rate of the optical field is directly proportional to the number of particles trapped N_Λ and the rate of bucket deceleration $|d\gamma_R/dz|$, but is inversely proportional to the field amplitude itself.

Therefore, in the optimization of a tapered FEL, particle trapping is merely one side of the picture. Maximizing the number of particles trapped is not a sufficient condition for maximizing the optical field strength. On the other side of the picture, the bucket also has to decelerate rapidly enough.

However, there is a conflict between rapid bucket deceleration and maintaining a large number of trapped particles. According to Eq. (5), $|d\gamma_R/dz|$ increases with ψ_R for $0 < \psi_R < \pi/2$. But according to Eq. (14), the bucket area decreases with ψ_R for $0 < \psi_R < \pi/2$. When choosing a ψ_R value, increasing the bucket deceleration rate will inevitably decrease the number of trapped particles and vice versa.

The optimization of a tapered FEL requires a good balance between these two conflicting factors. On one hand, we can sacrifice the bucket deceleration rate in exchange of better trapping. On the other hand, we can also sacrifice trapping in exchange of more rapid bucket deceleration.

E. Modification to the KMR model

In the KMR model, the constraint on the phase ψ_R of the resonant particle is somewhat arbitrary [9]. As an attempt to enhance the energy extraction efficiency further, we propose a modification to the KMR model.

Upon the modification, the resonant particle still maintains the resonant energy γ_R throughout the undulator line according to Eq. (3). However, its phase ψ_R is no longer kept constant. Instead, we now formulate ψ_R as a function of z which increases monotonically from zero. While there are many possible choices of such increasing functions, we can adopt the simplest function

$$\psi_R(z) = gz \quad \text{for some constant } g > 0. \tag{18}$$

In other words, ψ_R increases linearly with z at some gradient g, which is chosen by the FEL designer.

For any function $\psi_R(z)$ that increases monotonically from zero, there exists a value $z = L_d$ such that

$$\psi_R(L_d) = \frac{\pi}{2}. \tag{19}$$

This is when the bucket area becomes zero and total detrapping occurs. We therefore refer to L_d as the *detrapping length*. Note that it is possible to have $L_d > L_w$, where L_w is the total length of the undulator line. With this definition of L_d, the proportionality constant g in Eq. (18) can be written as

$$g = \frac{\pi}{2L_d}. \tag{20}$$

With our modification to the KMR model, ψ_R is smaller upstream and larger downstream. For small z, we sacrifice the bucket deceleration rate for particle trapping. For large z, we increase the bucket deceleration rate at the cost of detrapping more particles. We adopt this strategy for two main reasons as follows.

1. Particle trapping consideration

Particle trapping is more important at the beginning of the undulator line. The fraction of particles captured by the bucket at small z sets a limit on the amount of energy that can be extracted subsequently. With a constant ψ_R, the bucket shrinks abruptly from the full width of 2π to a reduced width of $\psi_2 - \psi_1$. This abrupt decrease in bucket width will lead to the sudden detrapping of a large fraction of particles. In contrast, if $\psi_R(z)$ increases smoothly from zero, the bucket will shrink from the full width of 2π in a gradual manner, which is more favorable for the capturing of particles.

2. Bucket deceleration consideration

Beyond the region of initial particle capturing, it is important to fully utilize bucket deceleration for energy extraction. Under the principle of energy conservation, the energy transferred to the optical field equals the total energy loss of all particles

$$W = m_e c^2 \sum_{i=1}^{N} |\gamma_i(L_w) - \gamma_i(0)|, \tag{21}$$

where N is the total number of particles. With a constant ψ_R, the bucket maintains the same width along z and most of the initially captured particles remain trapped. However, our goal here is not to trap all these particles up until the very end of the undulator line, but to make as many particles lose as much energy as possible. With an increasing ψ_R, the bucket will decelerate at an increasing rate, while shrinking in a gradual manner. With a properly chosen g in Eq. (18), the bucket centroid will experience a larger decrease in γ than in the case of a constant ψ_R over the same undulator length L_w, thus bringing trapped particles to lower energies. Even though the shrinking bucket will lead to gradual detrapping of particles along z, the deceleration of each particle up until the point of detrapping will contribute to the sum in Eq. (21). This, together with the more effective capturing of particles at small z, can result in a larger W.

F. Energy extraction efficiency

It is common to define the energy extraction efficiency of a tapered FEL as the product of the particle trapping and bucket deceleration efficiencies [4,11,12]. For instance, the particle trapping efficiency can be formulated as the normalized bucket width $(\psi_2 - \psi_1)/(2\pi)$ and the bucket deceleration efficiency as $\sin\psi_R$ [11].

However, this formulation is not directly applicable to our modified KMR model, in which ψ_R, ψ_1, and ψ_2 are continuously changing. Furthermore, the particle trapping efficiency is not only influenced by the bucket width, but also by the bucket area, which in turn depends on $E_0(z)$ and $a_w(z)$. Similarly, according to Eq. (5), the bucket deceleration rate $|d\gamma_R/dz|$ also depends on $E_0(z)$ and $a_w(z)$. Within a long undulator line, $E_0(z)$ and $a_w(z)$ can vary significantly and this needs to be taken into account.

We therefore propose a generalized formulation of the energy extraction efficiency as follows. At any axial position z along the undulator line, the number of particles trapped in the bucket is $N_\Lambda(z)$. For a small deceleration $d\gamma_R(z)$ of the bucket, the amount of energy lost by the particles is

$$dW(z) = -N_\Lambda(z) m_e c^2 d\gamma_R(z). \tag{22}$$

Integrating both sides over the entire undulator line gives the total amount of energy extracted:

$$W = -m_e c^2 \int_0^{L_w} N_\Lambda(z) \frac{d\gamma_R}{dz} dz. \tag{23}$$

Meanwhile, the initial energy of the electron beam is $W_{\text{beam}} = N\gamma_0 m_e c^2$. The ratio between W and W_{beam} gives the energy extraction efficiency:

$$\eta \equiv \frac{W}{W_{\text{beam}}} = -\frac{1}{\gamma_0}\int_0^{L_w} f_\Lambda(z)\frac{d\gamma_R}{dz}dz. \tag{24}$$

Here we have defined the trapping fraction $f_\Lambda(z) \equiv N_\Lambda(z)/N$. At this point, we can clearly see the dependence of the energy extraction efficiency on both the trapping fraction and the bucket deceleration rate. But since they are functions of z, they have to be integrated over z for the entire undulator line.

Next, we invoke Eq. (5), followed by Eq. (3), and rewrite the energy extraction efficiency explicitly as

$$\eta = \frac{e}{\sqrt{2}\gamma_0 m_e c^2}\sqrt{\frac{\lambda}{\lambda_w}}\int_0^{L_w}[E_0(z)f_\Lambda(z) \times \frac{a_w(z)f_B(z)}{\sqrt{1+a_w^2(z)}}\sin[\psi_R(z)]dz]. \tag{25}$$

In the integral, $\psi_R(z)$ is a predefined function, while $E_0(z)$, $f_\Lambda(z)$, and $a_w(z)$ need to be obtained from numerical simulations. This generalized expression for the energy extraction efficiency serves as a figure of merit for a tapered FEL.

III. METHOD

Based on the KMR model and the modified version, we optimize the taper profile $a_w(z)$ using the numerical simulation code GENESIS [8] in the steady-state mode. The principle is to perform iterative simulations along the entire undulator line, from $z = 0$ to $z = L_w$, with some small step size Δz. The required a_w value at every step Δz is computed according to the model.

In order to compute the a_w value, we substitute Eq. (3) into Eq. (5) and eliminate the variable γ_R. This yields

$$\frac{da_w}{dz} = -\frac{\sqrt{2}e}{m_e c^2}\frac{\lambda}{\lambda_w}f_B(z)E_0(z)\sin[\psi_R(z)]. \tag{26}$$

If the step size Δz is small enough, we can make the approximation $\Delta z \approx dz$ so that

$$a_w(z+\Delta z) = a_w(z) - \frac{\sqrt{2}e}{m_e c^2}\frac{\lambda}{\lambda_w}f_B(z)E_0(z)\sin[\psi_R(z)]\Delta z. \tag{27}$$

This is the equation used for the iterative simulations. In particular, $\psi_R(z)$ is a predefined function, for which the value at every z position is known. With a constant ψ_R as defined in Eq. (4), we refer to the method as the ordinary KMR method. With $\psi_R(z)$ modified as in Eq. (18), we refer to the method as the modified KMR method.

In order to use Eq. (27), we also need the initial values of the variables. In particular, $a_w(0)$ is chosen to be resonant with the initial beam energy. $E_0(0)$ is the field amplitude of the seed radiation. In the case of self-amplified spontaneous emission (SASE), the effective shot noise amplitude could be used instead. In each step Δz, we obtain the on-axis $E_0(z)$ from the numerical simulation. Equation (27) then enables us to compute the required a_w value at $z + \Delta z$ from the known values of a_w, f_B, ψ_R, and E_0 at z.

IV. RESULTS AND DISCUSSIONS

A. Application to a MAX IV FEL case

We apply the ordinary KMR method and the modified KMR method to a case of the future MAX IV FEL, in which we assume a 4-GeV and 4-kA electron beam. The main parameters are shown in Table I. A sensitivity study of these parameters can be found in Ref. [13].

To study the behavior of the electron beam, optical beam, and taper profile over a long distance, we simulate a continuous undulator line of length $L_w = 200$ m. For the purpose of beam focusing, we superimpose a FODO lattice on the undulator field. The length of the FODO cell is 5 m. Each cell contains two quadrupole magnets of length 10 cm, whose centers are separated by a longitudinal distance of 60 cm. The field strengths of the quadrupole magnets are adjusted to give the desired average beam size.

1. General results

For the ordinary KMR method, simulations reveal that the FEL power is maximized by choosing $\psi_R = 0.26$ rad. The evolution of various parameters along the undulator line are shown in Fig. 1. For the modified KMR method, the corresponding results for three selected g values, namely 3 mrad/m, 5 mrad/m, and 7 mrad/m, are shown in the same figure. These three g-values correspond to detrapping lengths of 600 m, 300 m, and 220 m, respectively.

As seen in Fig. 1(a), the ordinary KMR method features a slow, steady growth of FEL power throughout the undulator line. At $z = 200$ m, the power reaches 1.5 TW. For the

TABLE I. Main parameters of the MAX IV FEL case used in our simulation studies.

Parameter	Symbol	Value
Electron beam energy	W_{beam}	4 GeV
Energy spread	ΔW_{beam}	40 keV
Beam current	I	4 kA
Normalized emittance	$\epsilon_{x,y}$	0.2 mm mrad
Average beta	$\bar{\beta}_{x,y}$	20 m
Undulator period	λ_w	20 mm
Radiation wavelength	λ	4 Å
Seed radiation power	P_{in}	0.1 MW

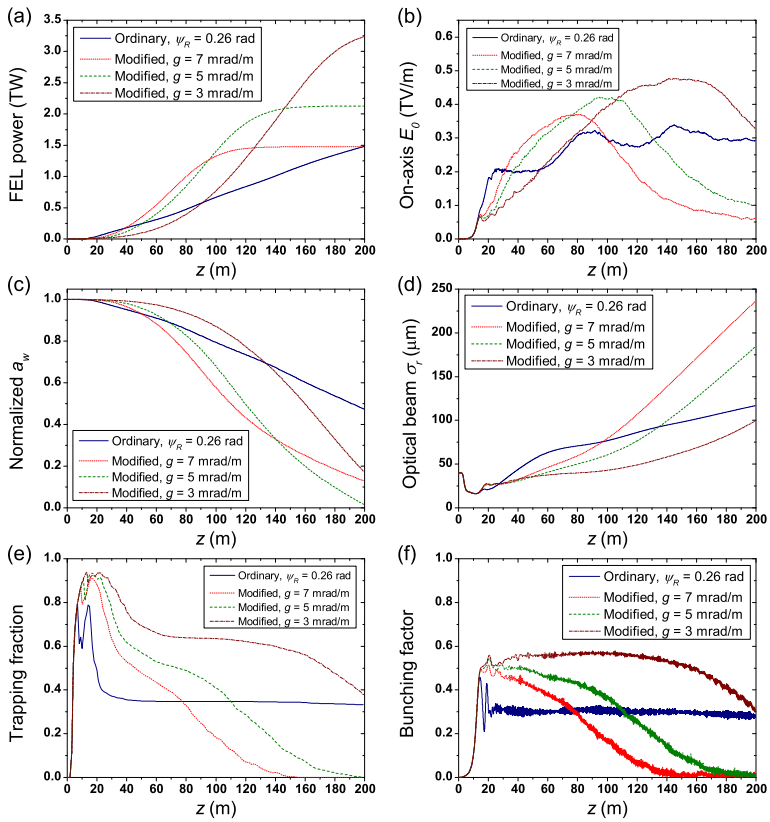

FIG. 1. Evolution of various parameters along the undulator line for the MAX IV FEL case. The parameters are (a) the FEL power, (b) the on-axis optical field amplitude, (c) the a_w parameter normalized to its initial value, (d) the rms radius of the optical beam, (e) the trapping fraction, and (e) the bunching factor. The four curves shown in each plot are the results of the ordinary KMR method with $\psi_R = 0.26$ rad and the modified KMR method with $g = 3$, 5 and 7 mrad/m.

Modified KMR method with $g = 7$ mrad/m, the same final power is attained. However, the power grows much more rapidly and final saturation is reached long before $z = 200$ m. This allows us to obtain the same power while shortening the undulator line to around 130 m, thus reducing the construction cost. With $g = 3$ mrad/m, the power at $z = 200$ m exceeds 3 TW, which is twice that produced by the ordinary KMR method.

In the modified KMR method, a larger g leads to more rapid power growth beyond the initial saturation [see Fig. 1(a)]. However, the final saturation occurs at a lower power and at a smaller z. In contrast, a smaller g leads to slower power growth beyond the initial saturation. However, the final saturation occurs at a higher power and at a larger z. In other words, g can be regarded as an independent adjustment knob for the final saturation power and the final saturation length of a tapered FEL.

The optimal g value depends on the given length of the undulator line. For instance, if the undulator line is shortened to 120 m, it is better to use $g = 5$ mrad/m than to use $g = 3$ or 7 mrad/m, as it yields the highest final power among the three cases. By the same token, if the undulator line is shortened to 80 m, it is better to use $g = 7$ mrad/m.

Figure 1(b) shows the on-axis optical field amplitude E_0 as a function of z. Comparing Figs. 1(a) and 1(b), we see that for the modified KMR method there exists a range of z where E_0 has ceased to grow while the FEL power continues to grow. This is precisely the *radiation power growth region* described in Ref. [3].

Figure 1(c) shows the four resulting taper profiles. The taper profiles resulting from the modified KMR method are more aggressive. The a_w parameter decreases so rapidly that its final value at $z = 200$ m is less than 20% of its initial value.

Figure 1(d) shows the rms radius σ_r of the optical beam as a function of z. For the modified KMR method, there is a correlation between the g value and the optical beam radius. In the deep-tapered region, a smaller g value corresponds to a smaller optical beam radius, which is a manifestation of stronger optical guiding.

There are two types of optical guiding, namely, gain guiding and refractive guiding [10,14]. In a tapered FEL, the latter usually dominates after the initial saturation point [10]. The effects of refractive guiding can be described by a complex-valued refractive index n, as defined in Ref. [14]. The strength of refractive guiding is measured by the real part of n. Under the resonant particle approximation, it can be written as

$$\mathrm{Re}[n(z)] = 1 + \frac{\sqrt{2}\lambda}{4\pi\epsilon_0 c}\frac{a_w(z)f_B(z)J_\Lambda(z)}{\gamma_R(z)E_0(z)}\cos[\psi_R(z)]. \quad (28)$$

With $\psi_R(z)$ as defined in Eq. (18), the strength of refractive guiding varies as $\cos(gz)$. At the same axial position z, a smaller g results in a larger $\cos(gz)$. This partly explains the correlation between the g value and the optical beam radius in Fig. 1(d).

Figure 1(e) shows the trapping fraction f_Λ as a function of z. With the ordinary KMR method, the trapping fraction soon reaches a plateau, meaning that the number of particles in the ponderomotive bucket is almost constant. With the modified KMR method, the trapping fraction is generally higher at small z, which reflects that the initial capturing of particles is more effective. However, the trapping fraction shows a gradual decrease along the undulator line. The larger is g, the faster is the decrease in the trapping fraction. Comparing Figs. 1(a) and 1(e), we see that when the trapping fraction drops to about 0.2, the FEL power begins to saturate.

Figure 1(f) shows the bunching factor as a function of z. Here the bunching factor is defined as

$$b \equiv |\langle e^{-i\psi}\rangle| = \frac{1}{N}\left|\sum_{j=1}^{N} e^{-i\psi_j}\right|. \quad (29)$$

With the resonant particle approximation, the contribution of the detrapped particles to the sum is zero and the sum over the remaining (trapped) particles becomes

$$b = \frac{1}{N}\left|\sum_{j=1}^{N_\Lambda} e^{-i\psi_R}\right| = \frac{N_\Lambda}{N}|e^{-i\psi_R}| = f_\Lambda. \quad (30)$$

In other words, under the resonant particle approximation, the bunching factor equals the trapping fraction. Comparing Figs. 1(e) and 1(f), the bunching fraction is indeed very close to the trapping fraction in the deep-tapered region. This confirms the validity of the resonant particle approximation in the deep-tapered region.

2. Phase space dynamics

Figure 2 shows the phase space snapshots for the two methods at four z positions along the undulator line. For the ordinary KMR method, the width of the ponderomotive bucket is almost the same at all the four z positions [see Fig. 2(a)]. For the modified KMR method, the bucket width decreases along the undulator line [see Fig. 2(b)]. This phenomenon is also reflected by the trapping fraction curve in Fig. 1(e). As the bucket shrinks in width, particles fall out of the bucket, thus leading to a decreasing trapping fraction. With a larger g value, ψ_R increases more rapidly and the bucket shrinks more rapidly, thus causing a faster decrease in trapping fraction.

Figure 3 shows the phase space trajectories of three representative particles in each of the two methods. Each trajectory has the shape of a spiral, which is a result of two combined effects: synchrotron oscillation and bucket deceleration. In synchrotron oscillation, a trapped particle orbits around the centroid of the bucket, whose position is defined by the resonant particle. In bucket

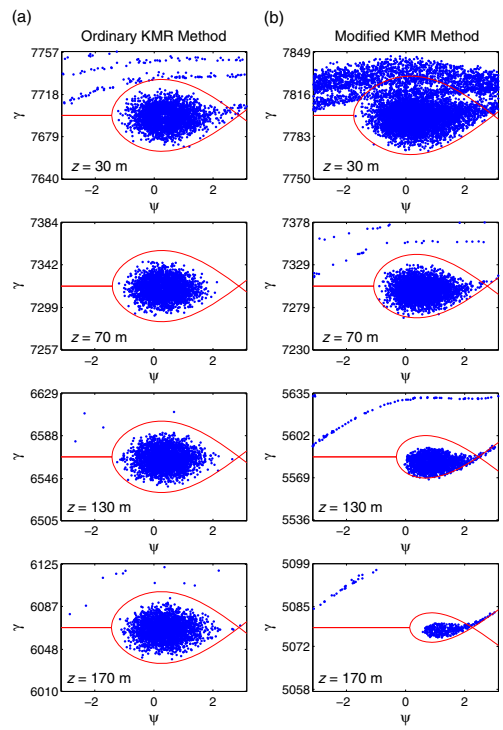

FIG. 2. The (ψ,γ) phase space at four different z positions for the (a) ordinary KMR method (with $\psi_R = 0.26$ rad) and (b) modified KMR method (with $g = 5$ mrad/m). The separatrices of the ponderomotive bucket are shown in red.

deceleration, the bucket centroid itself is moving towards smaller γ.

In the ordinary KMR method, ψ_R remains constant at all z. The trapped particles orbit around a bucket centroid that remains at the same phase [see Fig. 3(a)]. But in the modified KMR method, ψ_R increases with z. The trapped particles orbit around a bucket centroid that moves gradually towards larger phase [see Fig. 3(b)].

The spacing between successive turns in the spiral trajectory is determined by the frequency of the synchrotron oscillations and the rate of the bucket deceleration. The frequency of the synchrotron oscillations is given by [9]

$$\Omega_s(z) = \sqrt{\frac{2\sqrt{2}\pi e}{m_e c^2 \lambda_w} \frac{a_w(z) f_B(z) E_0(z)}{\gamma_R^2(z)} \cos[\psi_R(z)]}, \quad (31)$$

which varies with ψ_R as $\sqrt{\cos\psi_R}$. The rate of bucket deceleration $|d\gamma_R/dz|$, according to Eq. (5), varies with ψ_R as $\sin\psi_R$. This explains why the increase in the spacing between successive turns is more pronounced in the case of increasing ψ_R [see Fig. 3(b)] than in the case of constant ψ_R [see Fig. 3(a)].

We can also compare the final energy distributions of all particles in the ordinary KMR method and the modified KMR method, as in Fig. 4. The quantity $\gamma(L_w) - \gamma(0)$ is a measure of the energy lost by a particle throughout the undulator line.

For the ordinary KMR method (with $\psi_R = 0.26$ rad), the final energy distribution shows two distinct populations of particles [see Fig. 4(a)]. The particles around $\gamma(L_w) - \gamma(0) = 0$ are those which are not trapped during the initial capturing at small z. The particles around $\gamma(L_w) - \gamma(0) = -2000$ are those which remain trapped in the decelerating bucket up until the end of the undulator line. The former group constitutes about 60% of all particles, while the latter group constitutes about 40%.

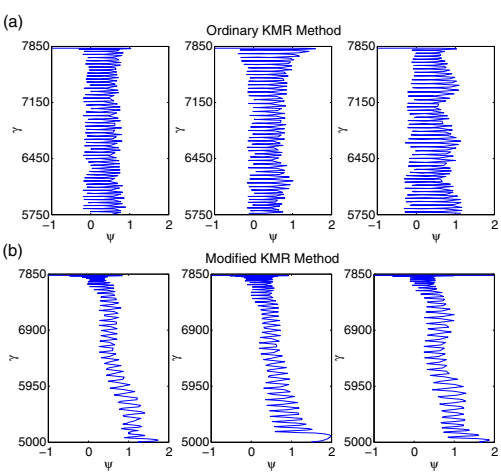

FIG. 3. Particle traces in the (ψ, γ) phase space for the (a) ordinary KMR method (with $\psi_R = 0.26$ rad) and (b) modified KMR method (with $g = 5$ mrad/m). For each of the two methods, the trajectories of three representative, trapped particles are shown.

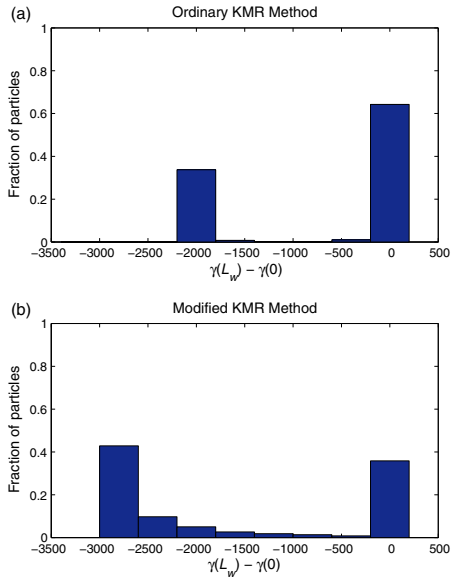

FIG. 4. Histograms showing the particle energy distributions at the end of the undulator line for the (a) ordinary KMR method (with $\psi_R = 0.26$ rad) and (b) modified KMR method (with $g = 3$ mrad/m).

For the modified KMR method (with $g = 3$ mrad/m), the particles around $\gamma(L_w) - \gamma(0) = 0$ constitute only less than 40% of all particles [see Fig. 4(b)], which shows that the initial capturing is more effective than in the ordinary KMR method. The other particles are distributed in a wide range of energies. But comparing the two histograms, the modified KMR method (with $g = 3$ mrad/m) is more effective in bringing more particles to lower energies overall.

In the modified KMR method (with $g = 3$ mrad/m), there is a larger fraction of particles with large $|\gamma(L_w) - \gamma(0)|$ [see Fig. 4(b)]. According to Eq. (21), this results in a larger total energy loss W, hence a larger total energy transfer to the optical field. This also explains the higher final FEL power exhibited in Fig. 1(a).

3. Phase manipulations of different orders

In the modified KMR method, we require $\psi_R(z)$ to be a function that increases monotonically from zero. So far we

have adopted the linear function given by Eq. (18), which is the simplest choice. Nonetheless, there are many other possible choices.

As an attempt to find out the optimal choice of $\psi_R(z)$, we explore three additional types of increasing functions, namely, quadratic ($\psi_R \propto z^2$), cubic ($\psi_R \propto z^3$), and square root ($\psi_R \propto z^{1/2}$). For each type of function, we vary the proportionality constant and examine the final FEL power at $z = L_w = 200$ m. The proportionality constant can be expressed in terms of the detrapping length L_d, which is defined in Eq. (19).

Figure 5 shows the variation of the final FEL power with L_d for the four types of functions. In each type of function, there exists an L_d that maximizes the final FEL power. For the linear functions, the maximum attainable final power is 3.2 TW, which occurs at $L_d = 600$ m. For the quadratic functions, the maximum attainable final power is 2.6 TW, which occurs at $L_d = 300$ m. For the cubic functions, the maximum attainable final power is 2.0 TW, which occurs at $L_d = 250$ m. For the square root functions, the maximum attainable final power is 3.0 TW, which occurs at $L_d = 3900$ m.

Comparing the four types of functions in Fig. 5, we see that the higher is the order of $\psi_R(z)$, the smaller is the L_d that maximizes the final power. In terms of maximizing the final FEL power, a linear increase in ψ_R with $L_d = 600$ m is the most favorable choice among all the scenarios studied in Fig. 5.

The optimal order of the increasing function $\psi_R(z)$ can depend on various factors, such as the total length L_w of the undulator line and the electron beam parameters. It can be a parameter for further optimization.

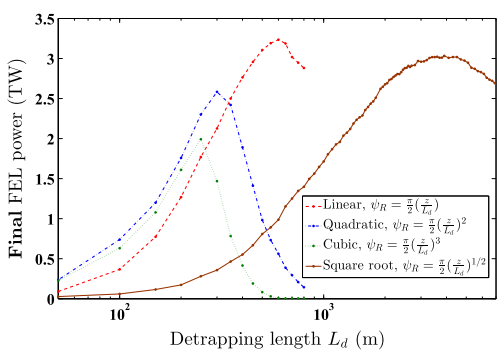

FIG. 5. Comparison of the final FEL powers resulting from different choices of the increasing function $\psi_R(z)$, namely, linear ($\psi_R \propto z$), quadratic ($\psi_R \propto z^2$), cubic ($\psi_R \propto z^3$), and square root ($\psi_R \propto z^{1/2}$). The final FEL power refers to the power at the end of the undulator line ($z = L_w = 200$ m) and is plotted as a function of the detrapping length L_d. Note that the L_d axis is on a logarithmic scale.

4. Energy extraction efficiency

The energy extraction efficiency η, given by Eq. (25), is a figure of merit for a tapered FEL. Using the results of our numerical simulations, we can compute η for the ordinary KMR method and the modified KMR method.

When applying the ordinary KMR method to the MAX IV FEL case, the final power is maximized by choosing $\psi_R = 0.26$ rad. This yields $\eta = 9.3\%$.

When applying the modified KMR method, the final power is maximized by choosing $L_d = 600$ m, which corresponds to $g = 3$ mrad/m. This yields $\eta = 20\%$.

In other words, our modification to the KMR model enables us to obtain more than twice the energy extraction efficiency.

B. Application to an LCLS-II case

We apply the ordinary KMR method and the modified KMR method also to a case of the LCLS-II facility. The case is defined in Jiao *et al.* [3], based on the design parameters at the time of its publication. As before, we simulate a 200-m continuous undulator line. For the ordinary KMR method, simulations reveal that the FEL power is maximized by choosing $\psi_R = 0.2$ rad. For the modified KMR method, the FEL power is maximized by choosing the g value 3 mrad/m.

Jiao *et al.* [3] also shows a taper profile produced by the GINGER self-design taper algorithm [4]. For the purpose of comparison, we extract this taper profile and input it to GENESIS [8] for a steady-state simulation. Since the precise configuration of the strong-focusing lattice is not provided in Jiao *et al.* [3], we have used an *ad hoc* FODO lattice for all the three methods here. The FODO lattice is superimposed on the undulator field and has a cell length of 4.4 m. Each cell contains two quadrupole magnets of length 13 cm, whose centers are separated by a longitudinal distance of 70 cm. The field strengths of the quadrupole magnets are adjusted to achieve the average beam radius of 17.5 μm.

We present the results of these three methods in the same figure. Figure 6(a) shows the evolution of the FEL power along the undulator line. Figure 6(b) shows the corresponding evolution of the optical field amplitude on axis. Figure 6(c) shows the taper profile.

As seen in Fig. 6(a), the final FEL power is 2.7 TW for the ordinary KMR method, 4.1 TW for the GINGER taper profile, and 5.8 TW for the modified KMR method. Out of the three methods, the modified KMR method (with $g = 3$ mrad/m) gives the highest final power.

There is a big difference in final FEL power between the ordinary KMR method and the GINGER algorithm, even though they are both based on the KMR model with constant ψ_R. One explanation for this difference is the treatments of the resonant particle in the two methods.

The ordinary KMR method relies on Eq. (26). When implementing the method, we have always taken $E_0(z)$ to

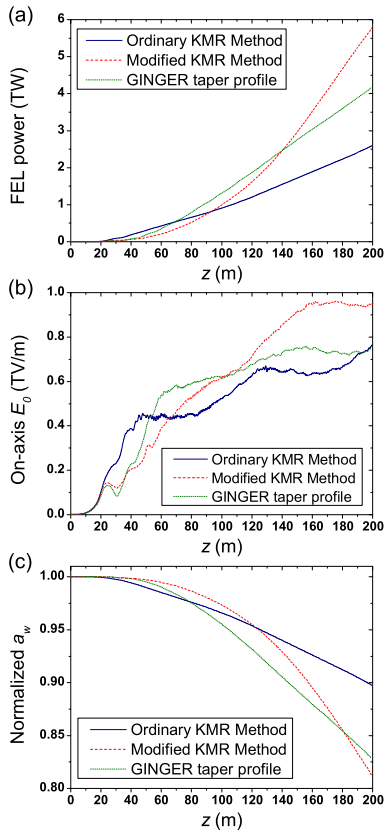

FIG. 6. Evolution of various parameters along the undulator line for the LCLS-II case. The parameters are (a) the FEL power, (b) the on-axis optical field amplitude, and (c) the a_w parameter normalized to its initial value. The three curves shown in each plot are the results of the ordinary KMR method (with $\psi_R = 0.2$ rad), the modified KMR method (with $g = 3$ mrad/m), and the GINGER taper profile from Jiao *et al.* [3].

be the value on the central axis of the FEL. In other words, the resonant particle in our ordinary KMR method is on axis.

But in Jiao *et al.* [3], the resonant particle used for the GINGER algorithm is off axis. It is fixed on the edge of the beam, at a radial position of about 17.5 μm. Using Eq. (26), we can backcalculate the function $\psi_R(z)$ for an on-axis resonant particle from the GINGER-produced taper profile in Fig. 6(c) and the corresponding on-axis $E_0(z)$ in Fig. 6(b). It turns out that $\psi_R(z)$ is not constant, but generally increasing (data not shown), if the resonant particle were to be on axis.

Finally, we compute the energy extraction efficiency η for the three methods according to Eq. (25). In the ordinary KMR method, the final power is maximized by choosing $\psi_R = 0.2$ rad and this yields $\eta = 9.2\%$. In the modified KMR method, the final power is maximized by choosing $g = 3$ mrad/m and this yields $\eta = 26\%$. Meanwhile, the GINGER taper profile gives $\eta = 19\%$. In other words, the modified KMR method gives the highest energy extraction efficiency among the three methods.

C. Undulator segment length

In both the ordinary KMR method and the modified KMR method, the function $a_w(z)$ is determined by iterative numerical simulations. The entire undulator line is divided into segments of length Δz and the required a_w value for each segment is obtained from Eq. (27). In the derivation of Eq. (27), the segment length Δz is assumed to be small. This subsection addresses the requirement on the segment length.

Within each segment Δz, the a_w value is constant. According to Eq. (3), this implies that γ_R is also constant. Recall that γ_R is the γ coordinate of the bucket's centroid in the (ψ, γ) phase space. With a constant γ_R, there is no bucket deceleration.

Meanwhile, the trapped particles continue to undergo synchrotron oscillations. If the segment Δz is long, the trapped particles can make multiple orbits within the non-decelerating bucket. Energy is transferred back and forth between the particles and the optical field. The FEL power then fluctuates, instead of growing steadily, along the undulator line. This can significantly reduce the final power, and hence the energy extraction efficiency, of the FEL.

To avoid this, the bucket must start decelerating again before the trapped particles finish one complete orbit. The distance traveled by a trapped particle down the undulator line during one complete orbit in phase space is the *synchrotron period*, given by

$$T_s(z) = \frac{2\pi}{\Omega_s(z)}. \tag{32}$$

Here Ω_s is the (angular) frequency of synchrotron oscillations given by Eq. (31). Note that T_s has the unit of length and Ω_s has the unit of inverse length. Both T_s and Ω_s are functions of z. Assuming that all the undulator segments have the same length Δz, we need

$$\Delta z < \min[T_s(z)]. \tag{33}$$

For the two FEL cases studied in this article, we have chosen Δz to be 0.5 m. From the simulation results, we compute the function $T_s(z)$ for each case. In the MAX IV FEL case, $\min[T_s(z)]$ ranges from 2.4 to 2.9 m among the four instances presented in Fig. 1. In the LCLS-II case (see Fig. 6), $\min[T_s(z)]$ is 6.0 m for the ordinary KMR method and 5.6 m for the modified KMR method. Thus, the requirement (33) is well satisfied.

V. CONCLUSION

In this work, we have examined the KMR model and proposed a modification to the model. This leads to the ordinary KMR method and the modified KMR method, which are implemented in GENESIS [8] for the purpose of taper optimization. Our modification to the model involves the manipulation of the resonant particle's phase ψ_R. This is motivated by considerations of particle trapping and bucket deceleration. To accommodate our modified KMR model, we have also proposed a generalized formulation for the energy extraction efficiency of tapered FELs.

We have applied the ordinary KMR method and the modified KMR method to two cases, namely, a MAX IV FEL case and an LCLS-II case. In the latter case, a taper profile obtained by Jiao *et al.* [3] from the GINGER self-design taper algorithm [4] is used as a benchmark. In both cases, the modified KMR method yields the highest output power. The results also show that our modification to the KMR model provides a means to enhance the energy extraction efficiency even further.

So far we have compared the different optimization methods by performing numerical simulations in the steady-state mode. Beyond this work, we will continue the studies in the time-dependent mode, so as to provide a better understanding of various time-dependent effects, such as side-band growth. We anticipate to present the results in a forthcoming article.

[1] T. J. Orzechowski *et al.*, High-Efficiency Extraction of Microwave Radiation from a Tapered-Wiggler Free-Electron Laser, Phys. Rev. Lett. **57**, 2172 (1986).

[2] D. F. Ratner *et al.*, in *Proceedings of the 31st International Free-Electron Laser Conference, Liverpool, 2009* (JACoW, Geneva, 2009), pp. 221–224 [http://accelconf.web.cern.ch/AccelConf/FEL2009/papers/tuoa03.pdf].

[3] Y. Jiao *et al.*, Modeling and multidimensional optimization of a tapered free electron laser, Phys. Rev. ST Accel. Beams **15**, 050704 (2012).

[4] W. M. Fawley, Z. Huang, K.-J. Kim, and N. A. Vinokurov, Tapered undulators for SASE FELs, Nucl. Instrum. Methods Phys. Res., Sect. A **483**, 537 (2002).

[5] N. M. Kroll, P. L. Morton, and M. N. Rosenbluth, Free-electron lasers with variable parameter wigglers, IEEE J. Quantum Electron. **17**, 1436 (1981).

[6] A. Mak, F. Curbis, and S. Werin, in *Proceedings of the 5th International Particle Accelerator Conference, Dresden, 2014* (JACoW, Geneva, 2014), pp. 2909–2911 [http://jacow.org/IPAC2014/papers/thpro023.pdf].

[7] S. Werin *et al.*, in *Proceedings of the 36th International Free-Electron Laser Conference, Basel, 2014* (JACoW, Geneva, 2014), pp. 549–552 [http://jacow.org/FEL2014/papers/tup080.pdf].

[8] S. Reiche, GENESIS 1.3: A fully 3D time-dependent FEL simulation code, Nucl. Instrum. Methods Phys. Res., Sect. A **429**, 243 (1999).

[9] D. Prosnitz, A. Szoke, and V. K. Neil, High-gain, free-electron laser amplifiers: Design considerations and simulation, Phys. Rev. A **24**, 1436 (1981).

[10] E. T. Scharlemann, in *High Gain, High Power Free Electron Lasers: Physics and Application to TeV Particle Acceleration*, edited by R. Bonifacio, L. De Salvo Souza, and C. Pellegrini (Elsevier, Amsterdam, 1989), pp. 95–125 [http://www.sciencedirect.com/science/book/9780444873958].

[11] C. A. Brau, in *Free-Electron Lasers* (Academic Press, Boston, 1990), pp. 236–255.

[12] J. M. Slater, Tapered-wiggler free-electron laser optimization, IEEE J. Quantum Electron. **17**, 1476 (1981).

[13] A. Mak, F. Curbis, and S. Werin, in *Proceedings of the 36th International Free-Electron Laser Conference, Basel, 2014* (JACoW, Geneva, 2014), pp. 399–402 [http://jacow.org/FEL2014/papers/tup018.pdf].

[14] E. T. Scharlemann, A. M. Sessler, and J. S. Wurtele, Optical Guiding in a Free-Electron Laser, Phys. Rev. Lett. **54**, 1925 (1985).

Paper II

Further studies of undulator tapering in x-ray FELs

A. Mak, F. Curbis, S. Werin.

Proceedings of FEL 2015, Daejeon, Korea, TUP002.

Proceedings of FEL2015, Daejeon, Korea TUP002

FURTHER STUDIES OF UNDULATOR TAPERING IN X-RAY FELs

Alan Mak*, Francesca Curbis, Sverker Werin, MAX IV Laboratory, Lund University, Sweden

Abstract

We further the studies of the model-based optimization of tapered free-electron lasers presented in a recent publication [Phys. Rev. ST Accel. Beams **18**, 040702 (2015)]. Departing from the ideal case, wherein the taper profile is a smooth and continuous function, we consider the more realistic case, with individual undulator segments separated by break sections. Using the simulation code GENESIS, we apply our taper optimization method to a case, which closely resembles the FLASH2 facility in Hamburg, Germany. By comparing steady-state and time-dependent simulations, we examine how time-dependent properties alter the optimal taper scenario. From the simulation results, we also deduce that the "traditional" empirical method, whereby the intermediate radiation power is maximized after closing every undulator gap, does not necessarily produce the highest final power at the exit of the undulator line.

INTRODUCTION

Present-day imaging experiments at x-ray free-electron laser (FEL) facilities call for an increased number of photons within a shorter pulse duration [1, 2]. To meet the stringent demand on the radiation power, the technique of undulator tapering has been revisited in recent years, and much theoretical effort has been dedicated to the optimization of this technique [3–6].

In a recent publication [6], we propose a modification to the Kroll-Morton-Rosenbluth (KMR) model [7], which serves as a method of optimizing the taper profile. The method features a variable phase of the resonant particle, and opens up possibilities for further enhancement of radiation power beyond the constant-phase model.

In the ideal case, the taper profile $K(z)$ is a smooth and continuous function. However, most existing taperable x-ray FELs, such as FLASH2 [8] and SACLA [9], consist of individual undulator segments separated by break sections. With these limitations, a reduction of radiation power from the ideal case is inevitable.

The break sections are needed for beam focusing, trajectory correction and diagnostics. However, vacuum diffraction of the optical beam in the break sections leads to a decrease in the on-axis field strength, which also causes particle detrapping [3].

Also, as each undulator segment is uniform within itself, the segment length sets a limit on the rate at which K can decrease, and hence a limit on the bucket deceleration rate. Furthermore, if the segment length is larger than the synchrotron period, the electron beam can absorb energy momentarily from the optical beam [6].

* alan.mak@maxlab.lu.se

In this article, we study a case with 2.5-m undulator segments separated by break sections. Using the simulation code GENESIS [10], we adapt our taper optimization method to these limitations, and obtain the highest possible power. We then compare the simulation results obtained in the steady-state mode and the time-dependent mode, quantifying the effects of time-dependent properties.

The case chosen for our simulation studies is intended to match the design parameters of the FLASH2 facility, which achieved its first lasing [11] in August 2014.

CASE DEFINITION

For the simulation studies in this article, we choose a case with main parameters as shown in Table 1. These parameter values are within the designed range for the FLASH2 facility [8].

Table 1: Main Parameters for the Simulated Case

Parameter	Symbol	Value
Electron beam energy	E	1.25 GeV
Peak current	I	2.5 kA
Bunch charge	Q	630 pC
Bunch length	σ_t	30 µm
Energy spread	σ_E	0.5 MeV
Normalized emittance	$\varepsilon_{x,y}$	1.4 µm rad
Average beta function	$\langle\beta_{x,y}\rangle$	6 m
Radiation wavelength	λ	6 nm
Undulator period	λ_w	31.4 mm
Undulator segment length	L_{seg}	2.5 m

The undulator segments considered in this case are planar. The lattice for the transverse focusing of the electron beam is in a FODO configuration. The period of the FODO cell is 6.6 m, in which two quadrupole magnets are 3.3 m apart from one another.

The FLASH2 facility has 12 undulator segments [8]. But in our simulation studies, we first consider a total of 30 segments, for the purpose of understanding the FEL dynamics over a long distance. After that, we consider the more realistic 12-segment case, by discarding all the subsequent segments in the simulations.

TAPER OPTIMIZATION METHOD

Our taper optimization method is detailed in a recent publication [6]. The method is based on the KMR model [7] and a modification thereto. It considers a resonant particle with phase-space coordinates (ψ_R, γ_R). With a constant phase $\psi_R(z) = \psi_R(0)$, it is known as the ordinary KMR

ISBN 978-3-95450-134-2

method. With an increasing phase

$$\psi_R(z) = \frac{\pi}{2}\left(\frac{z}{L_d}\right)^n,$$

it is known as the modified KMR method, where L_d and n are positive real numbers at our choice.

L_d is known as the detrapping length. At $z = L_d$, the phase ψ_R reaches $\pi/2$. The area of ponderomotive bucket then becomes zero, and total detrapping occurs. Adjusting L_d allows us to control the rate at which ψ_R increases.

The degree n does not have to be an integer. But in Ref. [6], we have shown with another case that the output power is maximized by choosing $n = 1$. In this article, we restrict ourselves to $n = 1$.

The method involves iterative simulations, with step size Δz along the undulator line. In the ideal case, Δz should be as small as possible, such as $\Delta z = \lambda_w$. But in the case at hand, the individual undulator segments require us to make the adaptation $\Delta z = L_{\rm seg}$. Furthermore, we adapt the method to the presence of break sections. In each step Δz, the decrease in on-axis field amplitude due to vacuum diffraction in the preceding break section is taken into account.

The iterative simulations are performed in the steady-state mode of GENESIS. Upon choosing a constant resonant phase ψ_R for the ordinary KMR method or a detrapping length L_d for the modified KMR method, the iterative simulations will result in a taper profile $K(z)$. Upon obtaining the taper profile, we input it to GENESIS again and run it in the time-dependent mode.

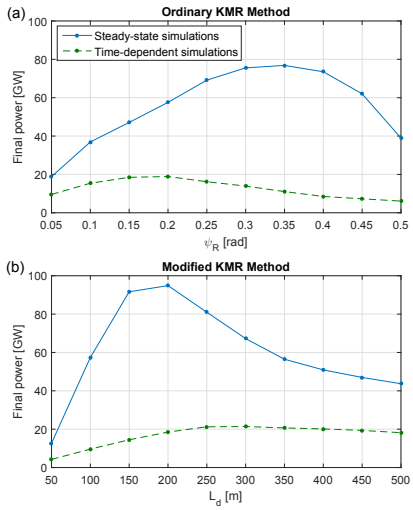

Figure 1: The final radiation power at the exit of the 30th undulator segment (a) as a function of the resonant phase ψ_R in the ordinary KMR method and (b) as a function of the detrapping length L_d in the modified KMR method. The blue solid curves are the results of steady-state simulations, and the green dashed curves are the results of time-dependent simulations.

RESULTS AND DISCUSSIONS

General Results with 30 Undulator Segments

To examine the FEL dynamics over a long distance, we simulate a total of 30 undulator segments with GENESIS.

For the ordinary KMR method, we vary the resonant phase ψ_R from 0.05 rad to 0.5 rad at intervals of 0.05 rad. For the modified KMR method, we vary the detrapping length L_d from 50 m to 500 m at intervals of 50 m.

In all these runs, we probe the final radiation power at the exit of the 30th undulator segment. The results are summarized in Fig. 1. The blue solid curves are the results of steady-state simulations, and the green dashed curves are the results of time-dependent simulations.

Ordinary KMR versus Modified KMR In the steady-state mode (see blue solid curves in Fig. 1), the final power is maximized at $\psi_R = 0.35$ rad for the ordinary KMR method, and at $L_d = 200$ m for the modified KMR method. The maximized final powers are 76.8 GW and 94.9 GW, respectively. The maximized final power for the modified KMR method is 123% that for the ordinary KMR method.

In the time-dependent mode (see green dashed curves in Fig. 1), the final power is maximized at $\psi_R = 0.2$ rad for the ordinary KMR method, and at $L_d = 300$ m for the modified KMR method. The maximized final powers are 18.9 GW and 21.4 GW, respectively. The maximized final power for the modified KMR method is 113% that for the ordinary KMR method.

In both the steady-state and the time-dependent modes, the modified KMR method produces a higher final power than the ordinary KMR method. This shows that an increasing ψ_R is more favourable than a constant ψ_R for maximizing the final power, even when time-dependent properties are taken into account. The benefit of using an increasing ψ_R over a constant ψ_R has been justified in Ref. [6] in terms of the initial capturing of particles and the rate of bucket deceleration.

Steady-state versus Time-dependent For the ordinary KMR method [see Fig. 1(a)], the maximized final power in the time-dependent mode constitutes a 75% drop from that in the steady-state mode. For the modified KMR method [see Fig. 1(b)], the maximized final power in the time-dependent mode constitutes a 77% drop from that in the steady-state mode. These show that time-dependent properties are a significant cause of power reduction.

The power reduction can be understood as follows. In GENESIS, a steady-state simulation is equivalent to considering only the central slice in a time-dependent simulation. Thus, a taper profile $K(z)$ obtained in the steady-state mode is only optimal for the centremost part of the longitudinal bunch profile, when running in the time-dependent mode. Towards the head and the tail of a Gaussian bunch profile,

ISBN 978-3-95450-134-2

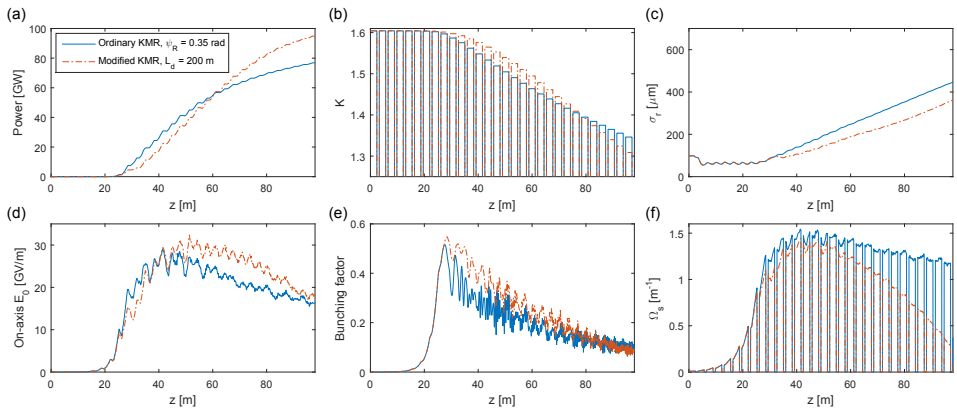

Figure 2: Results of steady-state simulations, showing the optimal scenarios of the ordinary KMR method (blue) and the modified KMR method (red) with the use of 30 undulator segments. The following quantities are plotted as functions of the distance z along the undulator line: (a) the radiation power; (b) the undulator parameter K; (c) the rms radius of the optical beam; (d) the field amplitude on axis; (e) the bunching factor; (f) the synchrotron frequency.

the slice current is significantly lower. These parts of the bunch behave in a non-optimal fashion under a taper profile $K(z)$ optimized for the central slice, thus reducing the average power produced by the bunch.

Another observation is that the optimal scenarios are not the same in the steady-state mode and in the time-dependent mode. When going from steady-state to time-dependent in the ordinary KMR method, the optimal ψ_R decreases. Similarly, when going from steady-state to time-dependent in the modified KMR method, the optimal L_d increases, which corresponds to an overall decrease in the range of ψ_R.

As discussed in Ref. [6], the area of the ponderomotive bucket decreases with ψ_R, while the bucket deceleration rate increases with ψ_R. This implies that in the presence of time-dependent effects, it is preferable to maintain a relatively large bucket at the expense of slowing down the bucket deceleration. This trade-off can be justified by the fact that time-dependent effects constitute an additional source of particle detrapping [3].

Optimal scenarios with 30 Segments

Without any tapering, power saturation occurs at around $z = 30$ m in the 10th undulator segment. This is known as the initial saturation point. The saturation power is 2.5 GW in the steady-state mode and 1.7 GW in the time-dependent mode.

The optimal taper scenarios in the steady-state mode are examined in Fig. 2. The blue solid curves correspond to the ordinary KMR method with $\psi_R = 0.35$ rad, while the red dashed curves correspond to the modified KMR method with $L_d = 200$ m.

Figure 2(a) shows the evolution of the radiation power along the undulator line. At the exit of the undulator line, the modified KMR method yields a higher power than the ordinary KMR method does, in agreement with Fig. 1. But upstream at $z = 30 - 60$ m, the situation is actually the opposite, i.e. the modified KMR method gives a *lower* power. This shows that it is possible to obtain a higher power downstream by sacrificing the power upstream. In other words, the "traditional" empirical method, whereby the radiation power is maximized after closing every undulator gap, does not necessarily yield the highest power at the end of the undulator line.

Figure 2(b) shows the taper profiles obtained from the iterative simulations. The individual undulator segments and the break sections are clearly seen. For both the ordinary KMR method and the modified KMR method, the K value hardly changes within the first seven segments. The decrease in K begins slightly before the initial saturation point. Immediately after the initial saturation point, the particle trapping development region begins [3]. In this region, the K value for the modified KMR method decreases more slowly than that for the ordinary KMR method. Downstream in the undulator line, the K value for the modified KMR method decreases more rapidly than that for the ordinary KMR method. Note that the rate of K decrease reflects the rate of bucket deceleration. For the modified KMR method, the bucket deceleration is kept slow in the particle trapping development region, thus allowing more particles to be captured in the bucket for the subsequent energy extraction.

Figure 2(c) shows the optical beam size as a function of z. Before the initial saturation point ($z = 30$ m), gain guiding keeps the optical beam size small. Beyond the initial saturation point, gain guiding is weakened, and refractive guiding becomes dominant. The strength of refractive guiding varies with the phase ψ_R as $\cos\psi_R$ [6]. For the modified KMR method, ψ_R increases with z, making the refractive guiding stronger. This partly explains why the optical beam size is

ISBN 978-3-95450-134-2

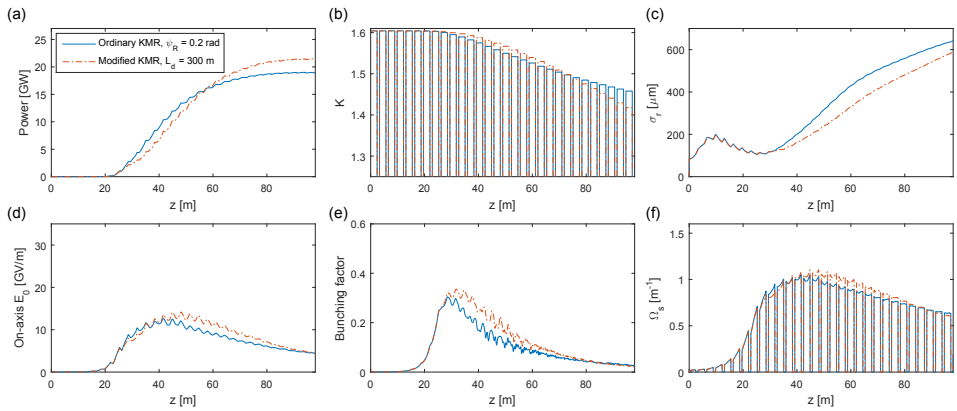

Figure 3: Results of time-dependent simulations, showing the optimal scenarios of the ordinary KMR method (blue) and the modified KMR method (red) with the use of 30 undulator segments. The following quantities are plotted as functions of z: (a) the radiation power; (b) the undulator parameter K; (c) the rms radius of the optical beam; (d) the field amplitude on axis; (e) the bunching factor; (f) the synchrotron frequency. These quantities are averaged over the electron bunch, and weighted by the slice current.

smaller for the modified KMR method than for the ordinary KMR method beyond the initial saturation point.

The effect of keeping the optical beam size small is also seen in Fig. 2(d), which shows the evolution of the on-axis field amplitude. With a smaller optical beam size beyond the initial saturation point, the modified KMR method gives a stronger field on axis.

Figure 2(e) shows the bunching factor as a function of z. Here the bunching factor is defined as the absolute value of $\langle e^{-i\psi} \rangle$, where the brackets denote the average over all particles, and ψ is the particle phase in the ponderomotive potential. In the particle trapping development region immediately beyond $z = 30$ m, the bunching factor for the modified KMR method is higher than that for the ordinary KMR method. This can be attributed to the larger on-axis field amplitude and the slower decrease in K value.

Figure 2(f) shows the synchrotron frequency as a function of z. The synchrotron frequency is given by [6, 12]

$$\Omega_s(z) = \sqrt{\frac{2\pi e}{m_e c^2 \lambda_w} \frac{K(z) f_B(z) E_0(z)}{\gamma_R^2(z)} \cos[\psi_R(z)]}.$$

For both the ordinary KMR method and the modified KMR method, the synchrotron frequency increases from zero at the entrance to the undulator line and reaches its maximum value slightly after the initial saturation point. Afterwards, the ordinary KMR method exhibits a relatively uniform synchrotron frequency, while the modified KMR method shows a rapid decrease in synchrotron frequency. The behaviour of the synchrotron frequency is a combined effect of the variations in K, E_0 and ψ_R along the undulator line.

Figure 3 shows the corresponding results in the time-dependent mode. The radiation power, K parameter, optical beam size, on-axis field amplitude and the bunching factor exhibit mostly the same patterns as in Fig. 2. However, the radiation power is lower overall [see Fig. 3(a)]. The diffraction of the optical beam is stronger [see Fig. 3(c)], and the on-axis field weaker [see Fig. 3(d)]. The bunching factor is also smaller overall [see Fig. 3(e)].

In the two optimal taper profiles Fig. 3(b), K decreases more slowly than in their steady-state counterparts [see Fig. 2(b)]. This also shows that in the presence of time-dependent effects, a slower deceleration of the ponderomotive bucket is preferable.

Comparing Fig. 3(f) to Fig. 2(f), we see that time-dependent effects give rise to a different behaviour of the synchrotron frequency. At $z = 40-80$ m, the synchrotron frequency is higher for the modified KMR method than for the ordinary KMR method in the time-dependent mode, but the situation is the opposite in the steady-state mode. Also, while the synchrotron frequency for the modified KMR method decreases very rapidly in the steady-state mode, it remains relatively uniform in the time-dependent mode.

Figure 4 shows the the spectral power distributions at the exit of the 30th undulator segment. The blue and red curves correspond to, respectively, the ordinary KMR method with $\psi_R = 0.2$ rad and the modified KMR method with $L_d = 300$ m, which are the the optimal scenarios in the time-dependent mode. The two distributions are largely similar.

Considering Only 12 Segments

The case studied in this article is intended to resemble the FLASH2 facility as closely as possible. The actual FLASH2 facility has 12 undulator segments [8]. Therefore, we now consider the more realistic 12-segment case by discarding all the subsequent segments in our simulation results.

ISBN 978-3-95450-134-2

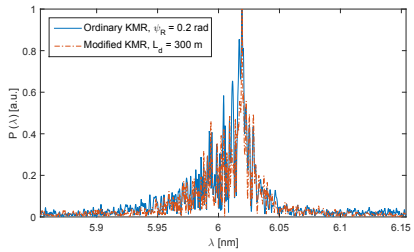

Figure 4: The spectral power distributions for the ordinary KMR method with $\psi_R = 0.2$ rad (blue) and for the modified KMR method with $L_d = 300$ m (red).

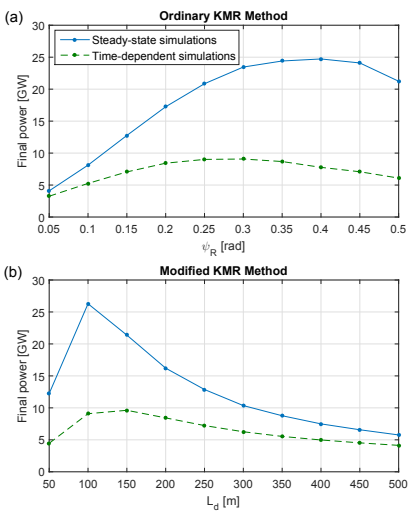

Figure 5: The final radiation power at the exit of the 12th undulator segment (a) as a function of the resonant phase ψ_R in the ordinary KMR method and (b) as a function of the detrapping length L_d in the modified KMR method. The blue solid curves are the results of steady-state simulations, and the green dashed curves are the results of time-dependent simulations.

The final power at the exit of the 12th segment is shown in Fig. 5 for different ψ_R and L_d values. With only 12 segments, the optimal ψ_R and L_d values are, of course, different from those in the 30-segment case. The reason is explained in Ref. [6].

In the steady-state mode (see blue solid curves in Fig. 5), the optimal ψ_R is 0.4 rad, which gives a final power of 24.7 GW; the optimal L_d is 100 m, which gives a final power of 26.3 GW.

In the time-dependent mode (see green dashed curves in Fig. 5), the optimal ψ_R is 0.3 rad, which gives a final power of 9.1 GW; the optimal L_d is 150 m, which gives a final power of 9.6 GW.

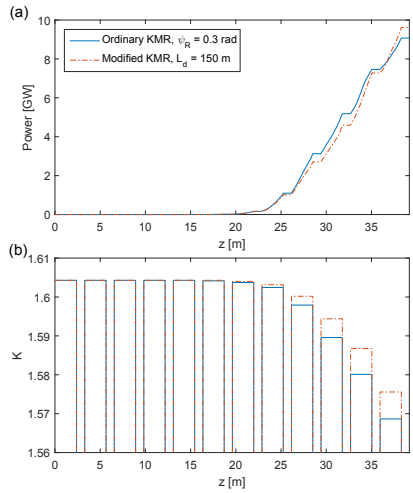

Figure 6: Results of time-dependent simulations, showing the optimal scenarios of the ordinary KMR method (blue) and the modified KMR method (red) with the use of only 12 undulator segments. (a) The bunch-averaged radiation power and (b) the undulator parameter K are plotted as functions of z.

With only 12 undulator segments, there is not a huge difference in final power between the ordinary KMR method and the modified KMR method. But compared to the case of no taper, the optimized tapers increase the final power by almost a factor of 11 in the steady-state mode, and a factor of 6 in the time-dependent mode.

The optimal scenarios in the time-dependent mode are shown in Fig. 6. It is apparent from Fig. 6(b) that the K value hardly changes in the first seven undulator segments. The post-saturation power growth is mainly due to the tapering of the last five segments.

As seen from Fig. 6(a), the modified KMR method yields a slightly higher final power at the exit of the 12th segment, compared to the ordinary KMR method. Nonetheless, upstream at $z = 25-35$ m, the power produced by the modified KMR method is actually *lower*. Once again, this shows that a higher power can be obtained at the exit of the undulator line by sacrificing the intermediate power upstream. This also implies that the "traditional" empirical method, whereby the intermediate power is maximized after closing every undulator gap, does not necessarily yield the highest final power.

SUMMARY AND OUTLOOK

In this article, we have furthered the study of a previously presented [6] taper optimization method, by adapting the

ISBN 978-3-95450-134-2

method to individual undulator segments separated by break sections. Using the simulation code GENESIS [10], we have applied the method to an x-ray FEL case, which closely resembles the FLASH2 facility [8] in Hamburg, Germany. By comparing the simulation results in the steady-state mode and the time-dependent mode, we have quantified the effects of time-dependent properties on the FEL dynamics. It would be an interesting experiment to test the 12-segment time-dependent simulation results on the FLASH2 facility.

REFERENCES

[1] R. Neutze et al., "Potential for Biomolecular Imaging with Femtosecond X-Ray Pulses", Nature **406**, 752 (2000).

[2] H. N. Chapman et al., "Femtosecond Diffractive Imaging with a Soft-X-Ray Free-Electron Laser", Nature Physics **2**, 839 (2006).

[3] Y. Jiao et al., "Modeling and Multidimensional Optimization of a Tapered Free Electron Laser", Phys. Rev. ST Accel. Beams **15**, 050704 (2012).

[4] C. Emma et al., "Terawatt X-Ray Free-Electron-Laser Optimization by Transverse Electron Distribution Shaping", Phys. Rev. ST Accel. Beams **17**, 110701 (2014).

[5] E. Schneidmiller, M. Yurkov, "Optimization of a High Efficiency Eree Electron Laser Amplifier", Phys. Rev. ST Accel. Beams **18**, 030705 (2015).

[6] A. Mak, F. Curbis, S. Werin, "Model-Based Optimization of Tapered Free-Electron Lasers", Phys. Rev. ST Accel. Beams **18**, 040702 (2015).

[7] N. M. Kroll, P. L. Morton, M. N. Rosenbluth, "Free-Electron Lasers with Variable Parameter Wigglers", IEEE J. Quantum Electronics **17**, 1436 (1981).

[8] K. Honkavaara et al., "Status of the FLASH II Project", in Proceedings of the 34th International Free-Electron Laser Conference, Nara, Japan, 381 (2012).

[9] T. Ishikawa et al., "A Compact X-Ray Free-Electron Laser Emitting in the Sub-Ångström Region", Nature Photonics **6**, 540 (2012).

[10] S. Reiche, "GENESIS 1.3: a Fully 3D Time-Dependent FEL Simulation Code", Nucl. Instrum. Meth. A **429**, 243 (1999).

[11] S. Schreiber, B. Faatz, "First Lasing at FLASH2", in Proceedings of the 36th International Free-Electron Laser Conference, Basel, Switzerland, 7 (2014).

[12] D. Prosnitz, A. Szoke, V. K. Neil, "High-Gain, Free-Electron Laser Amplifiers: Design Considerations and Simulation", Phys. Rev. A **24**, 1436 (1981).

ISBN 978-3-95450-134-2

PAPER III

Empirical optimization of undulator tapering at FLASH2 and comparison with numerical simulations

A. Mak, F. Curbis, B. Faatz, S. Werin.

DESY Report 16-168 (2016).

Empirical Optimization of Undulator Tapering at FLASH2 and Comparison with Numerical Simulations

Alan Mak[a,*], Francesca Curbis[a], Bart Faatz[b], Sverker Werin[a]

[a] *MAX IV Laboratory, Lund University, Fotongatan 2, S-22594 Lund, Sweden*
[b] *Deutsches Elektronen-Synchrotron DESY, Notkestraße 85, D-22607 Hamburg, Germany*

DESY Report 16-168 (Internally reviewed; approved for publication 29th August, 2016)

Abstract

In a free-electron laser equipped with variable-gap undulator modules, the technique of undulator tapering opens up the possibility to increase the radiation power beyond the initial saturation point, thus enhancing the efficiency of the laser. The effectiveness of the enhancement relies on the proper optimization of the taper profile. In this work, a multidimensional optimization approach is implemented empirically in the x-ray free-electron laser FLASH2. The empirical results are compared with numerical simulations.

Keywords: free-electron laser, undulator tapering, experiment, numerical simulation

1. Introduction

FLASH [1] is the free-electron laser (FEL) facility at the Deutsches Elektronen-Synchrotron (DESY) in Hamburg, Germany. It contains two undulator beamlines, FLASH1 and FLASH2, driven by the same linear accelerator. While FLASH1 consists of fixed-gap undulator modules, FLASH2 is equipped with variable-gap undulator modules. The variable-gap feature enables the simultaneous operation of FLASH1 and FLASH2 at different wavelengths [2]. It also enables the implementation of undulator tapering in FLASH2.

Undulator tapering involves the variation of the undulator parameter K as a function of the distance z along the undulator line, for the purpose of enhancing the radiation power (and hence the efficiency) of the FEL. This has been demonstrated empirically in x-ray FELs, such as LCLS [3] and SACLA [4]. In order to maximize the enhancement of radiation power, the taper profile $K(z)$ needs to be properly optimized.

Present-day imaging experiments at x-ray FELs call for an increased number of photons within a shorter pulse duration [5, 6]. To meet the stringent demand on the radiation power, the theory of taper optimization has been revisited in recent years. In Ref. [7], an important step is made towards the formulation of a universal taper law. In Refs. [8, 9], taper optimization methods based on the classic Kroll-Morton-Rosenbluth (KMR) model [10] are demonstrated in numerical simulations. In Refs. [11, 12], a multidimensional optimization method is performed in numerical simulations, whereby the optimal taper profile $K(z)$ is obtained by scanning through a parameter space comprising the taper order (such as linear and quadratic), the taper start point, the taper amplitude etc.

The multidimensional optimization approach is relatively straightforward. Guided by the theoretical studies, this approach is implemented empirically in FLASH2 at a wavelength of 44 nm, and the results are presented in this article. The empirical results of the taper optimization are then compared with the corresponding numerical simulations. The agreement and discrepancies between the empirical and simulation results are analyzed. The article concludes by excluding a number of otherwise possible causes of the discrepancies.

*Corresponding author
Email address: alan.mak@maxiv.lu.se

2. Empirical Study

2.1. Machine Parameters

FLASH2 contains a total of 12 undulator modules. Between every two adjacent modules, there is a drift section for beam focusing, trajectory correction, phase shifting, diagnostics etc. Table 1 shows the known machine parameters. For machine parameters not listed in Table 1, the nominal design values [1] are assumed.

Parameter	Symbol	Value
Electron beam energy	$\gamma m_e c^2$	646 MeV
Bunch charge	Q	300 pC
Radiation wavelength	λ	44 nm
Repetition rate	R	1 MHz
Undulator period	λ_w	31.4 mm
Magnetic length per module	L_{mod}	2.5 m
Period of FODO lattice	L_{FODO}	6.6 m

Table 1: Machine parameters

2.2. Taper Optimization Scheme

Each of the 12 undulator modules ($m = 1, 2, ..., 12$) is set to an undulator parameter K_m. Within each module, the undulator parameter is uniform. The taper profiles considered in this empirical study are defined by three parameters: the taper order d, the start module n and the taper amplitude $\Delta K/K$. These taper profiles are given by the ansatz

$$K_m = \begin{cases} K & \text{for } 1 \leq m < n \\ K\left[1 - \left(\dfrac{\Delta K}{K}\right)\left(\dfrac{m-n+1}{12-n+1}\right)^d\right] & \text{for } n \leq m \leq 12. \end{cases} \tag{1}$$

In Eq. (1), K is the *initial* undulator parameter, in resonance with the initial energy of the electron beam. The undulator parameter remains K from modules 1 to $n-1$, and decreases in steps from module n onwards. The taper order d equals 1 for linear tapering, and 2 for quadratic tapering. The taper amplitude $\Delta K/K$ is defined such that the undulator parameter of the last module is $K_{12} = K - \Delta K$.

Multidimensional optimization is performed by scanning d, n and $\Delta K/K$ empirically for the highest final radiation energy. The same type of multidimensional optimization in numerical simulations is presented in Refs. [11, 12].

2.3. Phase Shifter Configuration

In the drift section between every two undulator modules, there is a phase shifter for the proper matching of the phase between the electron beam and the optical field. The phase shifters are characterized in Ref. [13]. The required phase shift in each drift section depends solely on the undulator parameter of the preceding undulator module. The phase shifts are implemented automatically by a baseline procedure to ensure constructive interference between the optical fields emitted before and after each drift section. The procedure also accounts for the phase advance caused by the fringe fields at the two ends of each undulator module.

2.4. Radiation Energy Measurement

The lasing of FLASH2 takes place through the process of self-amplified spontaneous emission (SASE). The energy of a radiation pulse is measured with a micro-channel plate (MCP) detector [14], located downstream after the 12 undulator modules. The MCP detector offers a relatively high accuracy over a dynamic range of radiation intensities. To account for the shot-to-shot variability, each energy measurement is averaged over about 100 pulses.

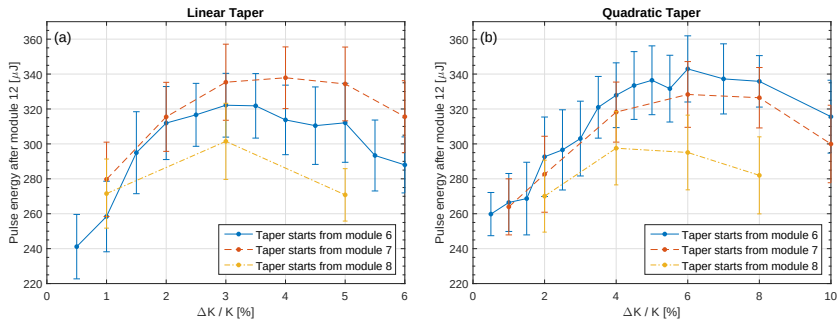

Figure 1: Empirical data. The final pulse energy is plotted as a function of the taper amplitude $\Delta K/K$ for (a) linear tapering ($d = 1$) and (b) quadratic tapering ($d = 2$). The blue solid curve, red dashed curve and yellow dotted curve correspond respectively to start modules $n = 6$, 7 and 8.

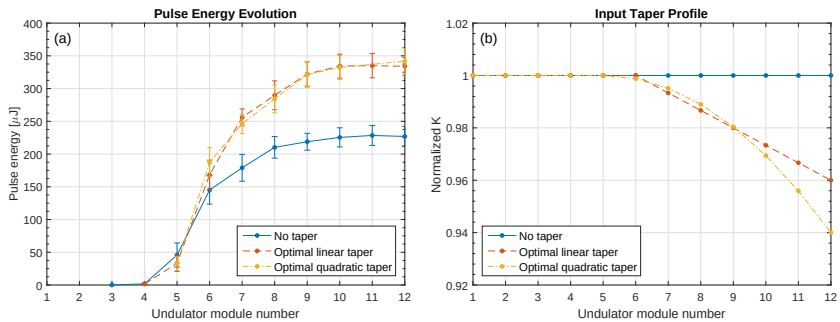

Figure 2: Empirical data. The evolution of the (a) optical pulse energy and (b) input undulator parameter along the undulator line. The undulator parameter is normalized to the initial value. The blue solid curve, red dashed curve and yellow dotted curve correspond respectively to no taper ($\Delta K/K = 0$), the optimal linear taper ($n = 7$, $\Delta K/K = 4\%$) and the optimal quadratic taper ($n = 6$, $\Delta K/K = 6\%$).

The gas-monitor detector (GMD) [15], which is also located downstream after the 12 undulator modules, measures the optical pulse energy in parallel. The GMD reading is used as a cross check.

With all the 12 undulator modules engaged, the MCP and GMD measure the *final* pulse energy. To examine the evolution of the pulse energy along the undulator line, it is necessary to measure the *intermediate* pulse energy upstream. To measure the pulse energy immediately after an upstream undulator module, the gaps of all subsequent modules are opened, so that the optical pulse propagates towards the detectors without further interacting with the electron beam. During the propagation, the optical pulse undergoes vacuum diffraction, and its transverse size can increase. So long as the detectors collect the signal of the *entire* optical pulse, the *pulse energy* remains unchanged.

2.5. Empirical Results

The final optical pulse energy is measured for different taper profiles given by Eq. (1). The measurement is done for taper orders $d = 1, 2$ and for start modules $n = 6, 7, 8$. The results are shown in Fig. 1. Each data point in Fig. 1 is obtained with the MCP detector, and is the average over 140 ± 50 pulses. The error bar indicates the standard deviation of the MCP readings. Among all the taper profiles considered in Fig. 1, the optimal linear taper occurs at $n = 7$ and $\Delta K/K = 4\%$, whereas the optimal quadratic taper occurs at $n = 6$ and $\Delta K/K = 6\%$.

For the optimal linear taper, the optimal quadratic taper and no taper, the intermediate pulse energies are measured. The evolution of the pulse energy along the undulator line is shown

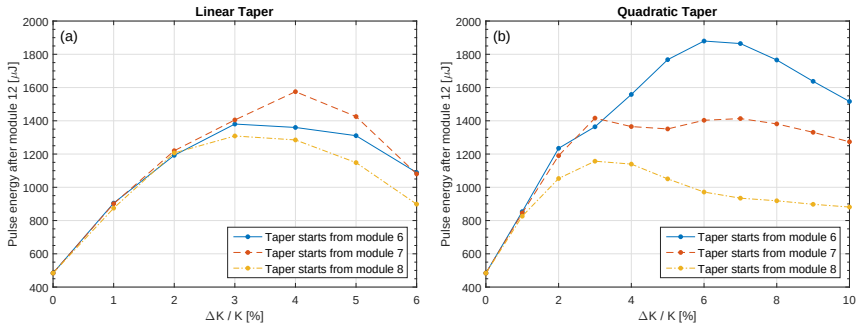

Figure 3: Simulation results. The final pulse energy is plotted as a function of the taper amplitude $\Delta K/K$ for (a) linear tapering ($d = 1$) and (b) quadratic tapering ($d = 2$). The blue solid curve, red dashed curve and yellow dotted curve correspond respectively to start modules $n = 6$, 7 and 8.

in Fig. 2(a). The corresponding taper profiles, as input from the control room, are shown in Fig. 2(b) for reference. Each data point in Fig. 2(a) is obtained with the MCP detector, and is the average over 110 ± 30 pulses. Among all the data points in Figs. 1 and 2(a), the absolute difference between the MCP and GMD values is 19 μJ on average, with a standard deviation of 16 μJ.

In the absence of tapering, the saturation of pulse energy is reached in module 8 [see solid curve in Fig. 2(a)]. In other words, the start modules ($n = 6, 7, 8$) considered in Fig. 1 are in the vicinity of the initial saturation point.

3. Comparison with Numerical Simulation

3.1. Simulation Parameters

The empirical results are compared with numerical simulation, after the experiment has been completed. The simulation is performed using the three-dimensional and time-dependent simulation code GENESIS [16], with parameter values as close as possible to the empirical ones (see Table 1). Parameters not specified in Table 1 are assumed to have the nominal values shown in Table 2.

Parameter	**Symbol**	**Value**
Peak current	I_0	1.5 kA
RMS bunch length	σ_z	24 μm
RMS energy spread	$\sigma_\gamma m_e c^2$	0.5 MeV
Normalized emittance	$\varepsilon_{x,y}$	1.4 mm mrad
Average of beta function	$\bar{\beta}_{x,y}$	6 m

Table 2: Nominal FLASH2 parameter values used in the simulation

In the simulation, the initial values of the optical functions and the quadrupole strengths are chosen self-consistently to give the desired average beta value, independent of the values used in the experiment.

3.2. Simulation Results

The same multidimensional optimization is performed in simulation. Using Eq. (1) as the ansatz, the parameters d, n and $\Delta K/K$ are scanned for the highest final radiation energy. The results are shown in Fig. 3. Among all the taper profiles considered in Fig. 3, the optimal linear taper occurs at $n = 7$ and $\Delta K/K = 4\%$, whereas the optimal quadratic taper occurs at $n = 6$ and $\Delta K/K = 6\%$.

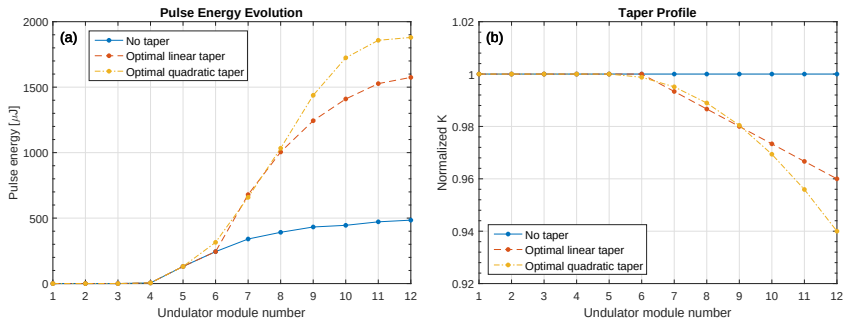

Figure 4: Simulation results. The evolution of the (a) optical pulse energy and (b) undulator parameter along the undulator line. The undulator parameter is normalized to the initial value. The blue solid curve, red dashed curve and yellow dotted curve correspond respectively to no taper ($\Delta K/K = 0$), the optimal linear taper ($n = 7$, $\Delta K/K = 4\%$) and the optimal quadratic taper ($n = 6$, $\Delta K/K = 6\%$).

For the optimal linear taper, the optimal quadratic taper and no taper, the simulated pulse energy evolutions along the undulator line are shown in Fig. 4(a). The corresponding taper profiles are shown in Fig. 4(b) for reference.

3.3. Comparing Empirical and Simulation Results

Comparing Fig. 1 (empirical) and Fig. 3 (simulation), the optimal taper profiles are consistent. In both cases, the optimal linear taper occurs at $n = 7$ and $\Delta K/K = 4\%$, and the optimal quadratic taper occurs at $n = 6$ and $\Delta K/K = 6\%$. Figs. 1 and 3 also show good agreement in the overall trend for the final optical pulse energy $\mathcal{E}$. In both cases, the overall trend for linear tapering ($d = 1$) is

$$\mathcal{E}(n = 7, \Delta K/K) > \mathcal{E}(n = 6, \Delta K/K) > \mathcal{E}(n = 8, \Delta K/K),$$

whereas the overall trend for quadratic tapering ($d = 2$) is

$$\mathcal{E}(n = 6, \Delta K/K) > \mathcal{E}(n = 7, \Delta K/K) > \mathcal{E}(n = 8, \Delta K/K).$$

However, Figs. 1 and 3 show disagreement in terms of the absolute pulse energies. The range of pulse energies is generally higher in the simulation than in the experiment.

Next, the pulse energy evolution along the undulator line is compared between simulation [see Fig. 4(a)] and experiment [see Fig. 2(a)]. In both cases, the pulse energy remains in the order of 1 μJ before module 5, and exceeds the 10-μJ threshold in module 5. In the absence of tapering, the initial saturation point is situated around module 8 in both cases (see solid curves). With the optimal linear and quadratic tapers, final saturation is reached within the 12 undulator modules in both simulation and experiment, but occurs earlier in the experiment than in the simulation (see dashed and dotted curves).

In the experiment, the optimal linear taper and the optimal quadratic taper yield almost identical final pulse energy. But in the simulation, the final pulse energy for the optimal quadratic taper is 1.2 times higher than that for the optimal linear taper.

In the experiment, the enhancement factor is

$$\frac{\mathcal{E}(\text{optimal taper})}{\mathcal{E}(\text{no taper})} = 1.5.$$

But in the simulation, the enhancement factor is

$$\frac{\mathcal{E}(\text{optimal taper})}{\mathcal{E}(\text{no taper})} = 3.9,$$

which is 2.6 times higher than that in the experiment.

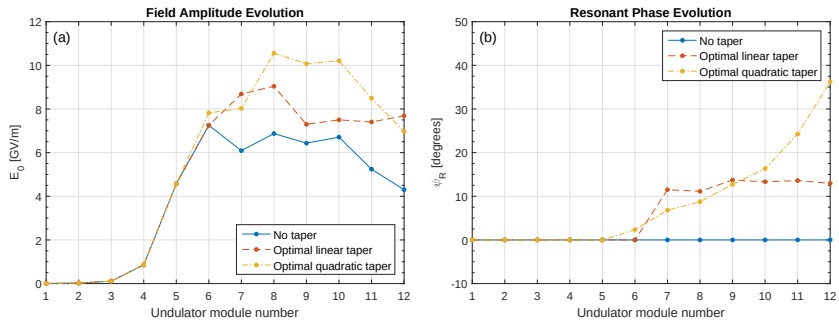

Figure 5: Simulation results. The evolution of the (a) optical field amplitude E_0 and (b) resonant phase ψ_R along the undulator line. The blue solid curve, red dashed curve and yellow dotted curve correspond respectively to no taper ($\Delta K/K = 0$), the optimal linear taper ($n = 7$, $\Delta K/K = 4\%$) and the optimal quadratic taper ($n = 6$, $\Delta K/K = 6\%$).

3.4. Discussion on the Taper Start Point

In both the simulation and empirical results, the optimal linear taper starts from module 7, while the optimal quadratic taper starts from module 6. The reason for this difference in the optimal start point is that the undulator parameter decreases much more slowly at the beginning of the quadratic taper. This is seen in Figs. 2(b) and 4(b). In module 6 from which the quadratic taper starts, the undulator parameter K_6 is effectively identical to the initial value K_1, as $K_6 = 99.88\% \times K_1 \approx K_1$. It is in module 7 where the undulator parameter starts to show a significant difference from the initial value. In other words, the optimal quadratic taper starts effectively from module 7, the same module from which the optimal linear taper starts.

Refs. [7, 17] suggest that the optimal taper start point is two gain lengths before the initial saturation point. In one-dimensional theory, the gain length is given by

$$L_g = \frac{\lambda_w}{4\sqrt{3}\pi\rho}, \tag{2}$$

where

$$\rho = \frac{1}{4}\left(\frac{I}{I_A \varepsilon_{x,y} \bar{\beta}_{x,y}}\right)^{1/3} \left(\frac{\lambda_w K f_B}{\pi\gamma}\right)^{2/3} \tag{3}$$

is the dimensionless Pierce parameter, $I_A = m_e c^3/e = 17.045$ kA is the Alfvén current, σ_x is the rms radius of the electron beam, and $f_B = J_0(\xi) - J_1(\xi)$ is the Bessel factor for planar undulators, with $\xi = K^2/[2(K^2+2)]$.

With the parameters in Tables 1 and 2, the Pierce parameter is $\rho = 3.51 \times 10^{-3}$, and the gain length is $L_g = 0.41$ m. Thus, the optimal taper start point is predicted to be $2L_g = 0.82$ m before the initial saturation point, excluding the length of the drift section between undulator modules. If we assume that the precise initial saturation point is at the beginning of module 8, then the optimal taper start point should lie within module 7. This rough prediction agrees with the simulation and empirical results.

3.5. Relating Optimal Taper Profiles to the KMR Model

The Kroll-Morton-Rosenbluth (KMR) model [10] is a theoretical analysis of undulator tapering in FELs based on a one-dimensional relativistic Hamiltonian formulation. In Refs. [8, 9], the KMR model is used as a method to optimize FEL taper profiles in numerical simulations. After choosing the resonant phase $\psi_R(z)$, the taper profile $K(z)$ is computed from the differential equation

$$\frac{dK}{dz} = -\frac{2e}{m_e c^2}\frac{\lambda}{\lambda_w} f_B(z) E_0(z) \sin[\psi_R(z)], \tag{4}$$

where E_0 is the on-axis field amplitude and z is the position along the undulator line. With a constant ψ_R, the optimization is known as the ordinary KMR method. With a variable ψ_R which increases gradually from zero, the optimization is known as the modified KMR method.

With the simulation results at hand, the evolution of the resonant phase ψ_R along the undulator line can be back-calculated from Eq. (4). This back-calculation requires the taper profile $K(z)$ [see Fig. 4(b)] and the field amplitude evolution $E_0(z)$ [see Fig. 5(a)] as inputs. Carrying out this back-calculation for the optimal linear taper, the optimal quadratic taper and no taper, the resulting $\psi_R(z)$ functions are shown in Fig. 5(b).

The optimal linear and quadratic tapers start from module 7 and module 6, respectively. Before the taper starts, $\psi_R = 0$ [see dashed and dotted curves in Fig. 5(b)]. This is expected, as $dK/dz = 0$ implies $\psi_R = 0$ according to Eq. (4). For the same reason, in the absence of any tapering, ψ_R remains zero at all times [see solid line in Fig. 5(b)].

When the optimal linear taper starts in module 7, ψ_R increases abruptly from 0 to 12°, and remains almost constant afterwards [see dashed curve in Fig. 5(b)]. When the optimal quadratic taper starts in module 6, ψ_R increases gradually and monotonically from 0, until it reaches a value of 36° in the final module [see dotted curve in Fig. 5(b)]. The $\psi_R(z)$ function for the optimal linear taper resembles one used in the ordinary KMR method, whereas the $\psi_R(z)$ function for the optimal quadratic taper resembles one used in the modified KMR method.

4. Post-Experimental Analysis of the Discrepancies

4.1. General Remarks

The empirical and simulation results are in good agreement in terms of:

- the $(n, \Delta K/K)$ values for the optimal linear and quadratic tapers;
- the overall trend in the plots of the final energy $\mathcal{E}$ versus $\Delta K/K$ (see Figs. 1 and 3); and
- the module in which the exponential gain crosses the 10-μJ threshold (see Figs. 2 and 4).

However, there are three main discrepancies between the empirical and simulation results:

- In the parameter space $(d, n, \Delta K/K)$ considered, the $\mathcal{E}$ range is generally lower in the experiment than in the simulation (see Figs. 1 and 3).
- The enhancement factor $\mathcal{E}$(optimal taper)/$\mathcal{E}$(no taper) is 3.9 in the simulation, but only 1.5 in the experiment.
- With the optimal linear and quadratic tapers, final saturation occurs earlier in the experiment than in the simulation (see Figs. 2 and 4).

The exact causes of these discrepancies are not known. Yet, it is possible to *exclude* a number of otherwise possible causes, such as the shot-to-shot variability, drift of the machine and wakefield effects. These are addressed in the upcoming subsections.

The discrepancies in question can also be caused by incorrect assumptions of parameter values. For the simulation, the nominal FLASH2 parameter values in Table 2 are assumed. The assumed nominal values in the simulation can be different from the unknown actual values in the experiment.

As illustrated in the sensitivity study in Ref. [18], a slight change in the emittance, energy spread or peak current can have a huge impact on the optimized radiation power of a tapered FEL. In other words, if the actual emittance, energy spread or peak current is worse than assumed, then the optimized radiation energy will be lower than expected. This will, in turn, influence the enhancement factor. This can possibly explain the discrepancies in question. However, the proposition that the emittance, energy spread or peak current is worse than assumed will be *disproved* in the following subsections.

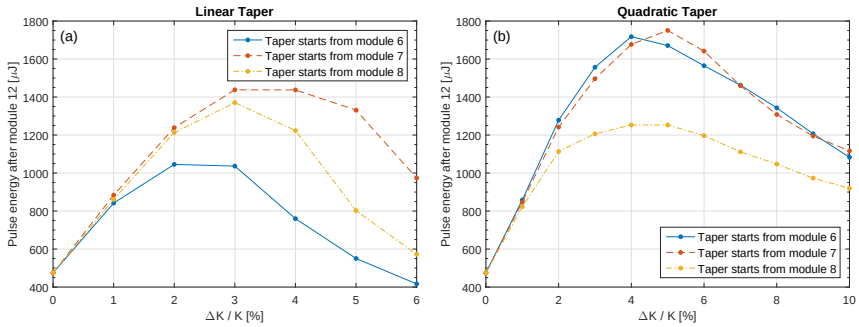

Figure 6: Simulation results with normalized emittance increased from 1.4 mm mrad to 1.6 mm mrad. The final pulse energy is plotted as a function of the taper amplitude $\Delta K/K$ for (a) linear tapering and (b) quadratic tapering.

4.2. Shot-to-Shot Variability

In the empirical results (Figs. 1 and 2), the shot-to-shot fluctuations are accounted for by the error bar, which indicates the standard deviation of many shots. All the error bars are within $\pm$ 23 μJ, which is too small to account for the discrepancies between the simulation and empirical results.

4.3. Drift of the Machine

Consider two scenarios in particular, the optimal linear taper and no taper. Since the optimal linear taper only starts from undulator module 7, the two scenarios are identical before module 7. In principle, the two scenarios should yield the same pulse energy evolution before module 7. This is precisely the case in the simulation [see solid and dashed curves in Fig. 4(a)], which is the ideal case free of any drift. But in the empirical results [see solid and dashed curves in Fig. 2(a)], the two scenarios yield slightly different energies in modules 5 and 6. The energy differences can be partly attributed to the drift of the machine. But despite the drift, the energy differences are still within 24 μJ, which is too small to account for the discrepancies between the simulation and empirical results.

4.4. Emittance Underestimated

In order to disprove that the emittance is underestimated, the simulation is repeated with the normalized emittance slightly increased, from 1.4 mm mrad to 1.6 mm mrad. All other parameters in Tables 1 and 2 are kept unchanged. With the average beta function $\bar{\beta}_{x,y}$ kept unchanged, this requires increasing the RMS beam radius $\sigma_{x,y}$ from 82 μm to 87 μm. The new simulation results are shown in Fig. 6.

If the emittance were indeed underestimated in the original simulation, then the new simulation (with an increased emittance) would show an improved agreement with the empirical results. But in the new simulation results, the overall trends of the final pulse energy $\mathcal{E}$ change. As seen in Fig. 6, the overall trend for linear tapering ($d = 1$) becomes

$$\mathcal{E}(n = 7, \Delta K/K) > \mathcal{E}(n = 8, \Delta K/K) > \mathcal{E}(n = 6, \Delta K/K),$$

whereas the overall trend for quadratic tapering ($d = 2$) becomes

$$\mathcal{E}(n = 6, \Delta K/K) \approx \mathcal{E}(n = 7, \Delta K/K) > \mathcal{E}(n = 8, \Delta K/K).$$

The overall trends actually become further off from those in the empirical results (see Fig. 1). Meanwhile, there is no improved agreement in the $\mathcal{E}$ range and in the enhancement factor. This disproves that the emittance is underestimated in the original simulation.

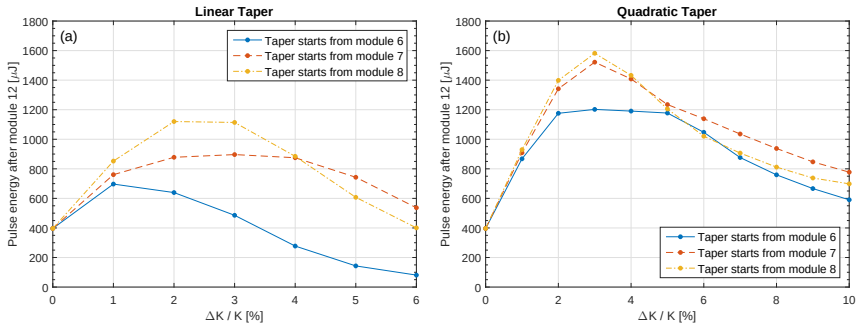

Figure 7: Simulation results with peak current decreased from 1.5 kA to 1.2 kA. The final pulse energy is plotted as a function of the taper amplitude $\Delta K/K$ for (a) linear tapering and (b) quadratic tapering.

Comparing the two sets of simulation results in Fig. 3 and 6, the increased emittance makes it more favourable to start the taper at a later point down the undulator line. The optimal quadratic taper in Fig. 3 starts from module 6, whereas that in Fig. 6 starts from module 7. As for linear taper, module 7 remains the most favourable start module. Yet, while module 8 is the least favourable of the three start modules considered in Fig. 3, it becomes the second most favourable in Fig. 6.

The shift in the optimal taper start point can be explained as follows. Refs. [7, 17] suggest that the optimal taper start point z_0 is two gain lengths before the initial saturation point. In one-dimensional theory, this is given by

$$z_0 = L_{\mathrm{sat}} - 2L_g = \frac{\lambda_w}{\rho} - 2\left(\frac{\lambda_w}{4\sqrt{3}\pi\rho}\right) = \left(1 - \frac{1}{2\sqrt{3}\pi}\right)\frac{\lambda_w}{\rho} \propto \frac{1}{\rho}. \tag{5}$$

With the definition of the Pierce parameter in Eq. (3), one can deduce that

$$z_0 \propto \frac{1}{\rho} \propto (\varepsilon_{x,y})^{1/3}. \tag{6}$$

The proportionality implies that an increased emittance moves the optimal taper start point downstream. It also implies that a further increase in emittance would move the optimal taper start point further downstream, thus making the overall trends of $\mathcal{E}$ even further off from those in the empirical results.

4.5. Peak Current Overestimated

In order to disprove that the peak current is overestimated, the simulation is repeated with the peak current slightly decreased, from 1.5 kA to 1.2 kA. In order to keep the known bunch charge in Table 1 unchanged, this requires increasing the RMS bunch length from 24 μm to 30 μm. All other parameters in Tables 1 and 2 are kept unchanged. The new simulation results are shown in Fig. 7.

Again, by decreasing the peak current in the simulation, the overall trends in the final pulse energy $\mathcal{E}$ become further off from those in the empirical results (see Fig. 1). This disproves that the peak current is overestimated.

Comparing the two sets of simulation results in Fig. 3 and 7, the decreased peak current also makes it more favourable to start the taper in a later undulator module. This agrees with the one-dimensional theoretical prediction from Eqs. (3) and (5) that

$$z_0 \propto \frac{1}{\rho} \propto \frac{1}{I^{1/3}}. \tag{7}$$

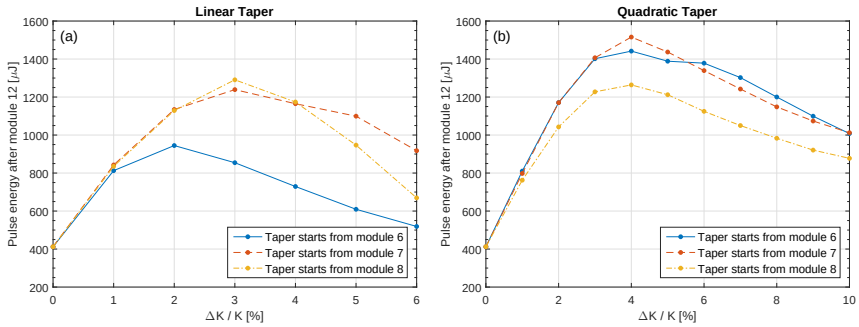

Figure 8: Simulation results with energy spread increased from 0.5 MeV to 0.7 MeV. The final pulse energy is plotted as a function of the taper amplitude $\Delta K/K$ for (a) linear tapering and (b) quadratic tapering.

4.6. Energy Spread Underestimated

In order to disprove that the energy spread is underestimated, the simulation is repeated with the energy spread slightly increased, from 0.5 MeV to 0.7 MeV. All other parameters in Tables 1 and 2 are kept unchanged. The new simulation results are shown in Fig. 8.

Again, by increasing the energy spread in the simulation, the overall trends in the final pulse energy $\mathcal{E}$ become further off from those in the empirical results (see Fig. 1). This disproves that the energy spread is underestimated.

Comparing the two sets of simulation results in Fig. 3 and 8, the increased energy spread also makes it more favourable to start the taper in a later undulator module. However, it is impossible to use the one-dimensional formulation to explain the shift in the optimal taper start point caused by the increased energy spread, as it is done for the emittance and the peak current. Nonetheless, the energy spread effects can be explained by similar arguments using the generalized formulation of Ming Xie [19].

4.7. Wakefield Effects

In Ref. [16], a simulation study on the effects of wakefields is performed on a case of the TTF-FEL, which is the predecessor of the FLASH1 and FLASH2 facilities. The machine parameters used in the simulation study are in the same orders of magnitude as those in Tables 1 and 2. The study identifies three major sources of wakefields, namely, the conductivity, surface roughness and geometrical changes of the beam pipe along the undulator. The simulation on the TTF-FEL case shows that wakefields can reduce the saturation power of the FEL by three orders of magnitude, while keeping the saturation length almost unchanged. In principle, wakefield effects can be a possible explanation for the discrepancies between our empirical and simulation results for FLASH2. However, this can be disproved as follows.

In the empirical optimization of undulator tapering, the optimal taper profile which maximizes the final radiation energy is also that which best compensates the energy loss due to wakefields [4]. Meanwhile, in the simulation which results in Fig. 3, wakefields are *not* considered. If wakefield effects were significant, then the optimal taper profile should occur at very different $(n, \Delta K/K)$ values in the empirical and simulation results. But as seen in Figs. 1 and 3, this is *not* the case. In fact, the experiment and simulation yield the exact same $(n, \Delta K/K)$ values for the optimal linear taper, and for the optimal quadratic taper. This leads us to the conclusion that wakefield effects are not significant in the experiment, and therefore do not account for the discrepancies in question.

4.8. Beam Trajectory Errors

The ideal trajectory of the electron beam is the central axis along the undulator line. But if the electron beam undergoes betatron oscillations as a whole, it deviates from the ideal

trajectory and is subject to trajectory errors. These errors can be caused by a combination of many factors, which include

- the imperfect alignment of the undulator modules;
- the imperfect alignment of the quadrupole magnets; and
- the inclined injection of the electron beam to the undulator modules.

Trajectory errors can degrade the FEL performance through a number of mechanisms [20]. A complete analysis of all these mechanisms is not trivial. But in taper optimization studies, it is the undulator parameter K which characterizes a taper profile. The following discussions shall focus on the implication of trajectory errors to K.

The undulator parameter K is associated with the magnetic field strength B_0 on the central axis of the undulator by the definition

$$K = \frac{e\lambda_w}{2\pi m_e c} B_0. \tag{8}$$

In the presence of trajectory errors, the electron beam deviates from the central axis. Even if the on-axis field strength B_0 were perfectly accurate, the electron beam would still experience a field strength different from the desired value B_0, hence an undulator parameter different from the desired value K. As derived in the Appendix, the effective undulator parameter is

$$K_{\text{eff}} = K \cosh(k_w y) \geq K, \tag{9}$$

where y is the deviation of the electron beam from the central axis, and $k_w = 2\pi/\lambda_w$ is the undulator wavenumber. The magnetic field strength experienced by an electron beam with a trajectory error y in an undulator with parameter K is equivalent to that experienced by an on-axis electron beam in an undulator of parameter K_{eff}.

The effective undulator parameter K_{eff} also leads to a phase shift error. As mentioned in Section 2.3, the required phase shift in the drift section depends solely on the K value of the preceding undulator module. Given an input value K, the phase shifter is automatically adjusted to ensure proper phase matching at the end of the drift section. But if the effective value is $K_{\text{eff}} \neq K$, then a phase mismatch will occur. As derived in the Appendix, this phase mismatch is given by

$$\delta\phi = -k_w L_D K^2 \left(1 + \frac{K^2}{2}\right)^{-2} [\cosh(k_w y) - 1], \tag{10}$$

Here L_D is the drift section length, which is 800 mm in FLASH2.

The simulation is now repeated with the K_{eff} and $\delta\phi$ associated with a trajectory error of $y = 250$ μm, calculated from Eqs. (9) and (10). With a trajectory error of $y = 250$ μm, the difference between K_{eff} and K becomes comparable to the Pierce parameter ρ, and is therefore significant. The new simulation results are shown in Fig. 9. Again, the overall trends in the final pulse energy $\mathcal{E}$ become further off from those in the empirical results (see Fig. 1). Thus, the K_{eff} and $\delta\phi$ associated of a trajectory error of $y = 250$ μm cannot account for the discrepancies between the empirical and simulation results.

4.9. Combination of Different Factors

In the preceding discussions, the different possible causes of the discrepancies in question are considered separately. In the following, combinations of these factors will be discussed.

Shot-to-shot fluctuations and the drift of the machine can each affect the measured optical pulse energy by about 20 μJ. The combined effect is then 40 μJ, which is still too small to account for the discrepancies in question.

The emittance, the peak current and the energy spread have been considered individually. As discussed in Sections 4.4–4.6, if any of these three parameters is worse than assumed, then

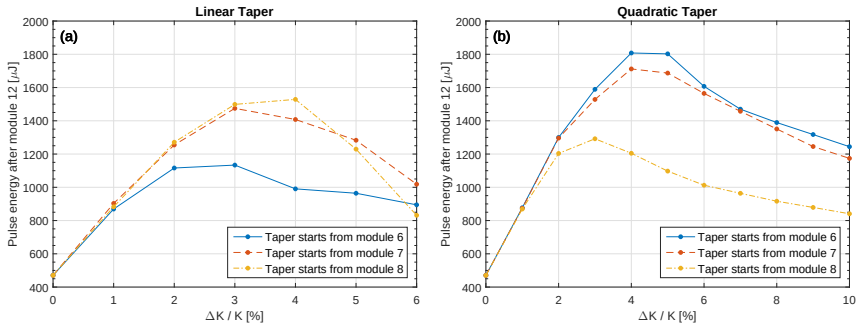

Figure 9: Simulation results for K_{eff} and $\delta\phi$ associated with a trajectory error of $y = 250$ μm. The final pulse energy is plotted as a function of the taper amplitude $\Delta K/K$ for (a) linear tapering and (b) quadratic tapering.

the optimal taper start point z_0 will be shifted downstream [see e.g. Eqs. (6) and (7)]. From this one can deduce that if all three (or at least two of the three) parameters are worse than assumed, then the optical taper start point z_0 will be shifted even further downstream. This will, in turn, make the overall trends of the final pulse energy $\mathcal{E}$ even further off from those in the empirical results. Thus, the discrepancies between the simulation and empirical results cannot be explained by the combination of an underestimated emittance, an overestimated peak current and an underestimated energy spread.

There are no indications that the three parameters are much different from their design values. But in principle, one could consider different scenarios where one parameter is worse than assumed while another parameter is *better* than assumed. One example examined in numerical simulation is the scenario where the normalized emittance is halved while the energy spread is doubled (results not shown). The resulting range of optical pulse energies becomes closer to that in the experiment. Yet, the overall trends of the final pulse energy $\mathcal{E}$, as well as the $(n, \Delta K/K)$ values of the optimal tapers, become further off from those in the experiment.

Even though there are possible explanations for some of the discrepancies between the empirical and simulation results, there is no simple explanation that would explain all differences.

5. Conclusion

A multidimensional optimization method has been implemented empirically in FLASH2, to optimize the taper profile for the maximum radiation energy. The empirical results have been correlated to simulations.

In the empirical study, the taper profile is characterized by the taper order d, the start module n and the taper amplitude $\Delta K/K$. For the optimal linear ($d = 1$) and quadratic ($d = 2$) tapers, the evolution of the optical pulse energy along the undulator line was examined.

The empirical results were compared with the corresponding results of numerical simulation. The two sets of results show good agreement in terms of the overall trend in the variation of the final pulse energy $\mathcal{E}$ with $\Delta K/K$. They also show good agreement for the optimal linear and quadratic tapers regarding the start module (n), the taper amplitude ($\Delta K/K$) and the exponential gain profile. However, there are discrepancies in terms of the general range of pulse energies, the enhancement factor from tapering, as well as the final saturation points for the optimal tapers.

Possible causes of the discrepancies have been examined, and a number of them excluded, such as emittance, energy spread and peak current deviations. Also, shot-to-shot variation, the drift of the machine, wakefield effects, as well as the systematic K and phase shift errors associated with a beam trajectory error have been excluded.

Remaining factors are mainly (i) a poor overlapping between the electron beam and the optical mode, caused by the misalignment and mismatch of the electron optics; and (ii) phase

mismatch caused by random errors in the phase shifters. These remaining factors need to be investigated in more detail. Further studies in numerical simulations and empirical measurements are planned for the future.

Acknowledgment

The authors would like to thank Katja Honkavaara and Siegfried Schreiber for their crucial roles in facilitating this international collaboration. The authors would also like to thank Evgeny Schneidmiller, Markus Tischer and Mikhail Yurkov for their participation in the planning meeting for the experimental work.

Appendix: Derivation of K_{eff} and $\delta\phi$

In Section 4.8, the effective undulator parameter K_{eff} associated with a trajectory error is discussed. This Appendix gives a derivation for K_{eff} and the subsequent phase mismatch $\delta\phi$.

Consider a pair of magnetic poles in the undulator, directly opposite to each other. Define the y-axis as the straight line passing through the middle points of the two pole tips. As usual, the z-axis is in the direction of beam propagation, perpendicular to the y-axis. A trajectory error in the y-direction changes the distance between the electron beam and the magnetic pole, which has a strong impact on the magnetic field strength experienced by the beam. Meanwhile, an trajectory error purely in the x-direction imposes no change on the beam-pole distance, and is therefore not treated here.

Following the derivation in Ref. [21], the variation of the magnetic field strength B_y along the y-axis is examined using a two-dimensional model in the yz-plane. Along the z-axis, the magnetic field strength is periodic, with a period of $\lambda_w = 2\pi/k_w$. Assuming that the periodic variation is perfectly sinusoidal, the following ansatz can be written for the magnetic scalar potential:

$$\varphi(y,z) = f(y)\cos(k_w z). \tag{11}$$

Here $f(y)$ is an unknown function which depends only on y. The scalar potential φ has to satisfy the Laplace equation

$$\nabla^2\varphi(y,z) = 0. \tag{12}$$

Substituting Eq. (11) into Eq. (12) results in the second-order ordinary differential equation

$$\frac{d^2 f(y)}{dy^2} - k_w^2 f(y) = 0, \tag{13}$$

to which the general solution is

$$f(y) = A_1\sinh(k_w y) + A_2\cosh(k_w y) \tag{14}$$

with arbitrary constants A_1 and A_2. Inserting this into Eq. (11), the scalar potential may be rewritten as

$$\varphi(y,z) = A_1\sinh(k_w y)\cos(k_w z) + A_2\cosh(k_w y)\cos(k_w z). \tag{15}$$

The y-component of the magnetic field is then

$$B_y(y,z) = -\frac{\partial\varphi}{\partial y} = -k_w A_1\cosh(k_w y)\cos(k_w z) - k_w A_2\sinh(k_w y)\cos(k_w z). \tag{16}$$

Recalling that the peak field on the z-axis is $B_y(0,0) = B_0$, we have $A_1 = -B_0/k_w$. Given the symmetry of the system about the plane $y = 0$, we have $B_y(+y,z) = B_y(-y,z)$ and hence $A_2 = 0$. With these results, Eq. (16) can be rewritten as

$$B_y(y,z) = B_0\cosh(k_w y)\cos(k_w z). \tag{17}$$

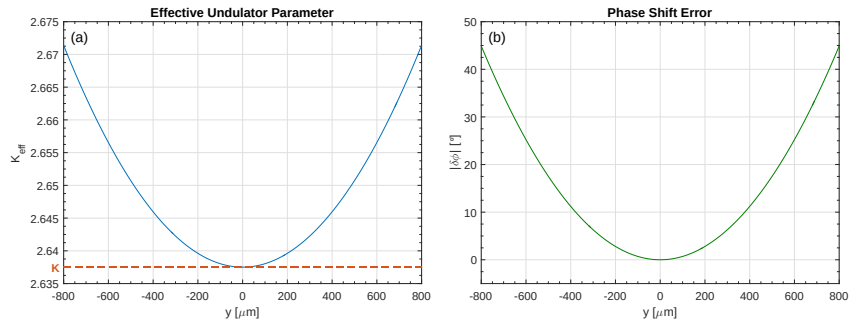

Figure 10: The following quantities are plotted as functions of the trajectory error y: (a) the effective undulator parameter K_{eff} of an undulator module and (b) the resulting error $|\delta\phi|$ in the phase shift immediately after the undulator module. These plots are made for a desired K value of 2.638, which is in resonance with the initial energy of the electron beam.

To examine the variation of B_y along the y-axis, we set $z = 0$ and obtain

$$B_y(y, 0) = B_0 \cosh(k_w y). \tag{18}$$

In other words, if the electron beam has a trajectory error of y, then it experiences a field $B_y(y, 0)$ as given by Eq. (18). Analogous to Eq. (8), the effective undulator parameter can be defined as

$$K_{\text{eff}}(y) \equiv \frac{e\lambda_w}{2\pi m_e c} B_y(y, 0) = \frac{e\lambda_w}{2\pi m_e c} B_0 \cosh(k_w y) = K \cosh(k_w y). \tag{19}$$

A plot of K_{eff} versus y is shown in Fig. 10(a). Note that $K_{\text{eff}}(y) > K$ for all $y \neq 0$, meaning that any trajectory error in the y-direction effectively *increases* the undulator parameter from the desired value K.

The difference between the effective undulator parameter K_{eff} and the desired value K can be expressed as

$$\delta K = K_{\text{eff}} - K = K[\cosh(k_w y) - 1]. \tag{20}$$

This difference of δK in an undulator module, in turn, leads to a phase mismatch in the drift section thereafter. In the drift section, there is a phase advance due to the speed difference between the electron beam and the radiation emitted in the preceding undulator module. For a drift length L_D after an undulator module with parameter K, this phase advance is [13]

$$\phi = k_w L_D \left(1 + \frac{K^2}{2}\right)^{-1}. \tag{21}$$

The phase shifter in the drift section is configured to perform automatic phase matching for the ϕ associated with the input value K. Thus, the difference of δK causes a phase shift error of

$$\delta\phi = -k_w L_D K \left(1 + \frac{K^2}{2}\right)^{-2} \delta K = -k_w L_D K^2 \left(1 + \frac{K^2}{2}\right)^{-2} [\cosh(k_w y) - 1]. \tag{22}$$

The absolute phase error $|\delta\phi|$ is shown in Fig. 10(b) as a function of y. In this discussion, the additional phase advance due to the fringe fields at the two ends of an undulator module is not considered.

References

[1] S. Schreiber, B. Faatz, "The Free-Electron Laser FLASH", High Power Laser Science and Engineering **3**, e20 (2015).

[2] B. Faatz et al., "Simultaneous Operation of Two Soft X-Ray Free-Electron Lasers Driven by One Linear Accelerator", New J. Phys. **18**, 062002 (2016).

[3] D. Ratner et al., "FEL Gain Length and Taper Measurements at LCLS", Proceedings of the 31st International Free-Electron Laser Conference, Liverpool, UK, 221 (2009).

[4] T. Tanaka et al., "Undulator Commissioning by Characterization of Radiation in X-Ray Free Electron Lasers", Phys. Rev. ST Accel. Beams **15**, 110701 (2012).

[5] R. Neutze et al., "Potential for Biomolecular Imaging with Femtosecond X-Ray Pulses", Nature **406**, 752 (2000).

[6] H. N. Chapman et al., "Femtosecond Diffractive Imaging with a Soft-X-Ray Free-Electron Laser", Nature Physics **2**, 839 (2006).

[7] E. A. Schneidmiller, M. V. Yurkov, "Optimization of a High Efficiency Free Electron Laser Amplifier", Phys. Rev. ST Accel. Beams **18**, 030705 (2015).

[8] A. Mak, F. Curbis, S. Werin, "Model-Based Optimization of Tapered Free-Electron Lasers", Phys. Rev. ST Accel. Beams **18**, 040702 (2015).

[9] A. Mak, F. Curbis, S. Werin, "Further Studies of Undulator Tapering in X-Ray FELs", Proceedings of the 37th International Free-Electron Laser Conference, Daejeon, Korea, 321 (2015).

[10] N. M. Kroll, P. L. Morton, M. N. Rosenbluth, "Free-Electron Lasers with Variable Parameter Wigglers", IEEE J. Quantum Electronics **17**, 1436 (1981).

[11] Y. Jiao et al., "Modeling and Multidimensional Optimization of a Tapered Free Electron Laser", Phys. Rev. ST Accel. Beams **15**, 050704 (2012).

[12] C. Emma et al., "High Efficiency, Multiterawatt X-Ray Free Electron Lasers", Phys. Rev. Accel. Beams **19**, 020705 (2016).

[13] M. Tischer et al., "Phase Shifters for the FLASH2 FEL", Proceedings of the 5th International Particle Accelerator Conference, Dresden, Germany, 2010 (2014).

[14] L. Bittner et al., "MCP-Based Photon Detector with Extended Wavelength Range for FLASH", Proceedings the 29th International Free-Electron Laser Conference, Novosibirsk, Russia, 334 (2007).

[15] K. Tiedtke et al., "Gas Detectors for X-Ray Lasers", J. Appl. Phys. **103**, 094511 (2008).

[16] S. Reiche, "GENESIS 1.3: a Fully 3D Time-Dependent FEL Simulation Code", Nucl. Instr. Meth. Phys. Res. A **429**, 243 (1999).

[17] W. M. Fawley et al., "Tapered Undulators for SASE FELs", Nucl. Instr. Meth. Phys. Res. A **483**, 537 (2002).

[18] A. Mak, F. Curbis, S. Werin, "Sensitivity Study of a Tapered Free-Electron Laser", Proceedings of the 36th International Free-Electron Laser Conference, Basel, Switzerland, 399 (2014).

[19] M. Xie, "Exact and Variational Solutions of 3D Eigenmodes in High Gain FELs", Nucl. Instr. Meth. Phys. Res. A **445**, 59-66 (2000).

[20] T. Tanaka, H. Kitamura, T. Shintake, "Consideration on the BPM Alignment Tolerance in X-Ray FELs", Nucl. Instr. Meth. Phys. Res. A **528**, 172 (2004).

[21] P. Schmüser, M. Dohlus, J. Rossbach, in *Ultraviolet and Soft X-Ray Free-Electron Lasers: Introduction to Physical Principles, Experimental Results, Technological Challenges* (Springer, Berlin, 2008), pp. 11-12.

PAPER IV

Phase jump method for efficiency enhancement in free-electron lasers

A. Mak, F. Curbis, S. Werin.

Phys. Rev. Accel. Beams (under 3rd review as of May 2017).

Phase Jump Method for Efficiency Enhancement in Free-Electron Lasers

Alan Mak,* Francesca Curbis, and Sverker Werin
MAX IV Laboratory, Lund University, P.O. Box 118, SE-22100 Lund, Sweden
(Dated: 10th April, 2017)

The efficiency of a free-electron laser can be enhanced by the phase jump method. The method utilizes the phase-shifting chicanes in the drift sections between the undulator segments. By applying appropriate phase jumps, the microbunched electron beam can decelerate and radiate coherently beyond the initial saturation, enabling further energy transfer to the optical beam. This article presents a new physics model for the phase jump method, and supports it with numerical simulations. Based on the electron dynamics in the longitudinal phase space, the model describes the energy extraction mechanism, and addresses the selection criteria for the phase jump magnitude. While the ponderomotive bucket is stationary, energy can be extracted from electrons outside the bucket. With the aid of the new model, a comparison is made between the phase jump method and undulator tapering. The model also explores the potential of the phase jump method to suppress the growth of synchrotron sidebands in the optical spectrum.

I. INTRODUCTION

In most single-pass free-electron laser (FEL) facilities, the undulator line is segmented by drift sections, where instruments for beam focusing, trajectory correction and diagnostics are installed. Often time, phase shifters are also installed in the drift sections [1–4].

Conventional phase shifters are compact magnetic chicanes, made up of either permanent magnets or electromagnets. The magnetic chicane can be used to increase the electron path length in the drift section, thus adjusting the phase angle between the electron beam and the optical wave.

A common application of phase shifters is phase correction, equalizing the phase angles at the two ends of a drift section. This allows the optical waves emitted in different undulator segments to interfere constructively. Without the phase correction, the velocity difference between electrons and light in the drift section can lead to an unwanted change in the phase angle, causing the optical waves to interfere destructively.

Another application of phase shifters is the suppression of the fundamental wavelength in harmonic lasing, thereby increasing the spectral intensity of the desired harmonic [5, 6]. In addition, the phase shifter is an essential element of the mode-locking technique [7] for the generation of attosecond optical pulses.

Moreover, phase shifters can be used for further energy extraction beyond the initial saturation, and hence the enhancement of the FEL efficiency. This is achieved by choosing appropriate phase jumps, and purposely altering the phase angle between the electron beam and the optical wave. This phase jump method was first proposed by Varfolomeev *et al.* [8], and can be used in place of the technique of undulator tapering [10–12].

The phase jump method was subsequently studied by Ratner *et al.* [9]. The study exploits the mathematical equivalence of phase jumps and undulator tapering, and relies on a pre-optimized taper to deduce the required phase jumps.

In this article, we further the study of the phase jump method by developing a physics model independent of undulator tapering. Our intuitive model illustrates the particle dynamics in the longitudinal phase space, and enables a deeper understanding of the energy extraction mechanism.

In Section II, we start with the steady-state model, focusing on a single ponderomotive bucket. We propose the microbunch deceleration cycle, and describes the energy extraction both in and out of the bucket.

In relation to this mechanism, we discuss the selection criteria for each phase jump, the requirement on the undulator segment length, and the origin of the final saturation. We then compare and contrast our phase jump model with the classic Kroll-Morton-Rosenbluth (KMR) model [10] of undulator tapering.

In Section III, we verify the features of our steady-state model by means of a steady-state numerical simulation.

In Section IV, we expand the steady-state model to include time-dependent effects. In particular, we discuss the potential of the phase jump method to suppress the growth of sidebands in the optical spectrum.

In Section V, we perform a time-dependent simulation to demonstrate that the phase jump method remains valid in the presence of time-dependent effects, and to demonstrate that the phase jump method is more effective than undulator tapering in sideband suppression.

II. STEADY-STATE MODEL

A. Problem description

Consider an FEL with a planar undulator line segmented by drift sections, as depicted in Fig. 1. All undulator segments have the same length L_{segm}, and all drift sections have the same length L_{drift}. In every drift section, there is a phase shifter installed. The distance

* alan.mak@maxiv.lu.se

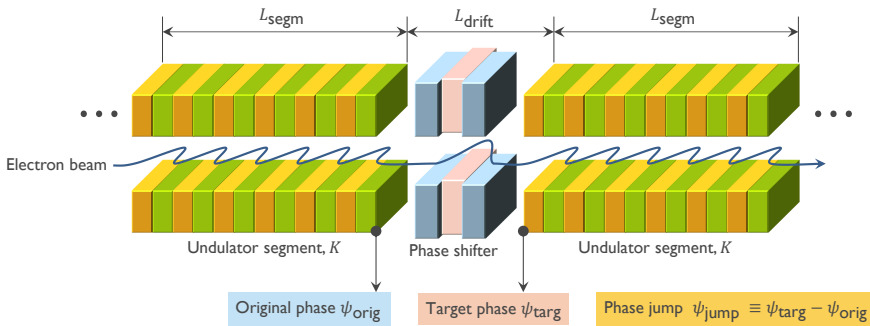

FIG. 1. Schematic diagram showing two of the undulator segments and the drift section in between. The phase shifter in the drift section can increase the electron path length, thus adjusting the phase angle between the electron beam and the optical wave. Focusing magnets, corrector magnets and diagnostics instruments are also commonly installed in drift sections, but are not shown in this diagram.

between the centres of every two adjacent phase shifters is $L_{\rm segm} + L_{\rm drift}$, which is constant.

In this section, we develop a one-dimensional, steady-state model of the phase jump method, which makes use of the phase shifters to sustain the growth of radiation power at the fundamental wavelength beyond the initial saturation point.

In particular, we are interested in the effect of the phase jumps alone, in the absence of undulator tapering. We therefore restrict ourselves to a constant undulator period $\lambda_u = 2\pi/k_u$ and a constant undulator parameter

$$K = \frac{eB_0}{m_e c k_u}, \tag{1}$$

where e is the absolute value of the electron charge, m_e is the electron rest mass, c is the speed of light, and B_0 is the peak undulator field.

In addition, we assume the amplitude E_0 and phase ϕ of the optical field to be slowly varying in the course of the FEL interaction.

B. Energy definitions

The energy of an electron can be expressed as $\gamma m_e c^2$, and the resonant energy $\gamma_R m_e c^2$ is defined by

$$\gamma_R = \sqrt{\frac{\lambda_u}{2\lambda}\left(1 + \frac{K^2}{2}\right)}, \tag{2}$$

where $\lambda = 2\pi/k$ is the radiation wavelength.

In the case of monochromatic seeding, λ is the wavelength of the seed radiation, and γ_R is determined by λ through Eq. (2). In the case of self-amplified spontaneous emission (SASE), γ_R is determined by the energy of the incoming electron beam, and λ is determined by γ_R through Eq. (2).

With undulator tapering, the undulator parameter K decreases with the distance z along the undulator line. According to the definition in Eq. (2), γ_R decreases with z to retain the radiation wavelength λ. Without undulator tapering, however, K is constant. According to the definition in Eq. (2), γ_R remains constant to retain λ.

In other words, the resonant energy is constant in the phase jump method. This allows us to express the energy of an electron as the relative deviation from the resonant energy, by the variable

$$\eta \equiv \frac{\gamma - \gamma_R}{\gamma_R}. \tag{3}$$

Even though the resonant energy is constant by definition, if the electrons themselves can decrease in η beyond the initial saturation point, they can continue to transfer energy to the optical field.

C. Phase definitions

The longitudinal profile of the electron bunch is customarily treated in slices of width λ. During the FEL interaction, each slice contains a pondermotive potential well. In the steady-state model, all slices are assumed to be identical, and it suffices to consider only a single slice.

In the analysis of phase jumps, we are not interested in the *absolute* phase of an electron. Instead, it is more convenient to consider the phase of an electron relative the ponderomotive potential well, with the usual definition

$$\psi \equiv (k + k_u)z - \omega t + \phi. \tag{4}$$

Within a single slice, ψ spans from $-\pi$ to π.

As indicated in Fig. 1, we let $\psi_{\rm orig} \in [-\pi, \pi]$ be the original phase of an electron at the start point of a drift section, and $\psi_{\rm targ} \in [-\pi, \pi]$ be the target phase at the

end point of the same drift section. We then define the phase jump as the difference:

$$\psi_{\text{jump}} = \psi_{\text{targ}} - \psi_{\text{orig}} \in [-2\pi, 2\pi]. \tag{5}$$

Note that $\psi_{\text{jump}} = 0$ does *not* mean that the phase shifter is turned off. Instead, it means that the phase shifter is configured merely for phase correction, whereby the phase angle between the electron and the optical field at the beginning of the drift section is preserved at the end of the drift section.

Note also the sign convention that a *positive* ψ_{jump} corresponds to shifting the electron *forward* in ψ. However, a conventional phase shifter applies the phase jump by increasing the electron path length. It can only shift electrons backward in ψ, but not forward. In practice, if the required ψ_{jump} is positive, we need to shift the electron backward to another potential well by a phase of $2n\pi - \psi_{\text{jump}}$, where n is a positive integer.

As a side note, this phase jump method for efficiency enhancement can, in principle, be implemented in combination with the iSASE technique [14] for bandwidth reduction. This is done by choosing a large n, so that the optical field emitted by the electrons towards the tail of the bunch may develop correlations with the electrons towards the head of the bunch, thus increasing the coherence length.

D. Equations of motion

In our model of the phase jump method, we concern ourselves with the electron dynamics in the longitudinal phase space (ψ, η). In the undulator segments, the longitudinal dynamics of an electron can be described by two equations of motion:

$$\frac{d\eta}{dz} = -\frac{\Omega^2}{2k_u}\sin\psi, \tag{6}$$

$$\frac{d\psi}{dz} = 2k_u\eta. \tag{7}$$

A derivation of these equations is given in Ref. [13].

In Eq. (6), the quantity

$$\Omega = \sqrt{\frac{e}{m_e c^2}\frac{k_u K f_B E_0}{\gamma_R^2}} \propto \sqrt{E_0} \tag{8}$$

is the angular frequency of the synchrotron oscillation, which has the dimension of inverse length. Meanwhile, $f_B = J_0(\xi) - J_1(\xi)$ is the Bessel factor for planar undulators, with $\xi = K^2/[2(K^2+2)]$. By substituting Eq. (6) into the derivative of Eq. (7), we can verify that the longitudinal dynamics satisfies the pendulum equation

$$\frac{d^2\psi}{dz^2} + \Omega^2 \sin\psi = 0. \tag{9}$$

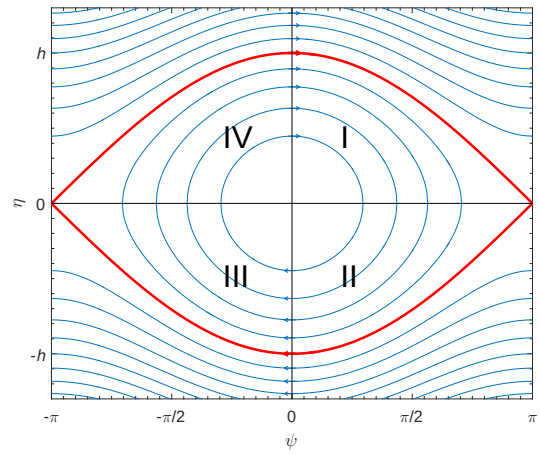

FIG. 2. The longitudinal phase space (ψ, η), with electron trajectories shown by the blue curves. The red curve is the *separatrix*, and the region enclosed by it is the *ponderomotive bucket*. The straight lines $\eta = 0$ and $\psi = 0$ divide the space into four quadrants, as indicated by the Roman numerals.

E. Phase space trajectories

The equations of motion (6) and (7) satisfy the Hamilton equations for the Hamiltonian

$$H(\psi, \eta) = ck_u\eta^2 + \frac{c\Omega^2}{2k_u}(1 - \cos\psi). \tag{10}$$

The electron trajectories in the longitudinal phase space (ψ, η) are given by the level set of the function $H(\psi, \eta)$, and are shown in Fig. 2.

In particular, the trajectory highlighted in red is known as the *separatrix*. Along the separatrix, the Hamiltonian has the value

$$H_{\text{sep}} = H(\pm\pi, 0) = \frac{c\Omega^2}{k_u}. \tag{11}$$

The region enclosed by the separatrix is known as the *ponderomotive bucket*. Within the bucket, $H < H_{\text{sep}}$. The trajectories are closed orbits, and the electrons are *trapped*. Outside the bucket, $H > H_{\text{sep}}$. The trajectories are unbounded, and the electrons are *detrapped*.

The maximum η value along the separatrix gives the half-height of the bucket,

$$h = \frac{\Omega}{k_u}. \tag{12}$$

Invoking the definition of the synchrotron frequency in Eq. (8), we obtain the proportionality

$$h \propto \sqrt{E_0}, \tag{13}$$

meaning that the bucket half-height h increases with the optical field amplitude E_0.

In Fig. 2, the horizontal line $\eta = 0$ and the vertical line $\psi = 0$ divide the longitudinal phase space into four quadrants, as indicated by the Roman numerals.

In quadrants I and II, $\psi > 0$. In quadrants III and IV, $\psi < 0$. According to Eq. (6), this implies $d\eta/dz < 0$ in quadrants I and II, and $d\eta/dz > 0$ in quadrants III and IV. In other words, electrons decelerate in quadrants I and II, and accelerate in quadrants III and IV. Due to the conservation of energy, energy is transferred to the optical field in quadrants I and II, and energy is absorbed from the optical field in quadrants III and IV.

In quadrants I and IV, $\eta > 0$. In quadrants II and III, $\eta < 0$. According to Eq. (7), this implies that electrons have increasing ψ in quadrants I and IV, and decreasing ψ in quadrants II and III.

F. Phase jump commencement

The essence of the phase jump method is microbunch deceleration. The aim is to decelerate the microbunched beam after the initial saturation, so that it can continue to radiate coherently. Thus, the phase jumps should commence in the vicinity of the initial saturation point, where the microbunching is fully developed.

In the exponential regime, the phase shifters should be configured for $\psi_{\text{jump}} = 0$, or there will be disruption in the microbunching development. For SASE FELs in particular, applying $\psi_{\text{jump}} \neq 0$ in the exponential regime can also lead to a red or blue shift in the radiation wavelength, depending on the magnitudes of the phase jumps and their positions along the undulator line [6].

G. Microbunch deceleration mechanism

To analyze the microbunch deceleration, it is convenient to follow the motion of an average particle within the microbunch μ. Let $(\bar{\psi}, \bar{\eta})$ be the coordinates of the average particle in the longitudinal phase space. They can be defined as

$$\bar{\eta} \equiv \langle \eta \rangle_\mu = \frac{1}{N} \sum_{j \in \mu}^{N} \eta_j, \tag{14}$$

$$\bar{\psi} \equiv \arg \left\langle e^{-i\psi} \right\rangle_\mu = -i \ln \left(\frac{1}{N} \sum_{j \in \mu}^{N} e^{-i\psi_j} \right), \tag{15}$$

where N is the number of particles in μ.

Microbunch deceleration takes place in quadrants I and II, where particles decelerate and transfer energy to the optical field (see Fig. 2). Thus, a general principle of the phase jump method is to increase the time that the average particle spends in the deceleration quadrants (I and II), and decrease the time that the average particle spends in the acceleration quadrants (III and IV).

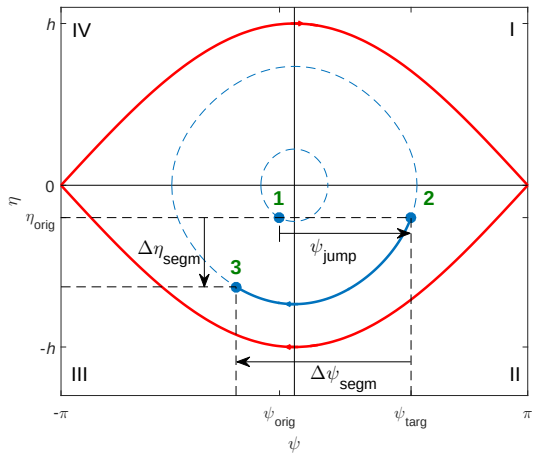

FIG. 3. The microbunch deceleration cycle as illustrated by the movement of the average particle within the ponderomotive bucket. Position 1 corresponds to the start point of a drift section, position 2 the end point of the same drift section, and position 3 the end point of the subsequent undulator segment.

In the longitudinal phase space (ψ, η), a phase jump moves a particle horizontally. If the average particle lies in quadrant IV, then we should choose a phase jump that moves it into quadrant I. If it lies in quadrant III, then we should move it into quadrant II. If it lies in quadrant II but is about to enter quadrant III, then we should move it to a slightly larger phase within quadrant II (i.e. away from quadrant III).

The mechanism is illustrated in Fig. 3. Suppose that the average particle has an original phase $\bar{\psi} = \psi_{\text{orig}} < 0$ at the start point of a drift section, as indicated by position 1. We then apply a phase jump $\psi_{\text{jump}} > 0$, so that the average particle arrives at a target phase $\bar{\psi} = \psi_{\text{targ}} > 0$ at the end point of the drift section, as indicated by position 2.

In an ideal phase shifter, electrons have no energy loss to synchrotron radiation, and the average particle has the same η at positions 2 as at position 1.

At position 2, the electrons enter an undulator segment, and follow the phase space trajectories described by Eqs. (6) and (7). In particular, the average particle follows the solid blue curve. So long as $\bar{\psi} > 0$, the microbunch decelerates, and transfer energy to the optical field.

The average particle then arrives at position 3, as it reaches the end point of the undulator segment. Depending on the length L_{segm} of the undulator segment, position 3 can be located in either quadrant II or III. In quadrant III, where $\bar{\psi} < 0$, the microbunch absorbs energy from the optical field.

Within the undulator segment, $\bar{\psi}$ and $\bar{\eta}$ of the average

particle have changed by $\Delta\psi_{\rm segm}$ and $\Delta\eta_{\rm segm}$, respectively. Provided that $\Delta\eta_{\rm segm} < 0$, the microbunch has a net deceleration, and hence a net energy transfer to the optical field.

In the course of the energy transfer, the optical field amplitude E_0 changes. Consequently, the bucket half-height h changes according to the proportionality (13). In principle, this can also lead to a distortion of the particle trajectories in the longitudinal phase space (ψ, η). However, since E_0 is assumed to be slowly varying, the distortion of the solid blue curve is negligible as the average particle transits from position 2 to position 3.

The end point of the undulator segment is also the start point of the next drift section. We can then repeat this microbunch deceleration cycle, by taking position 3 of the old cycle as position 1 of the new cycle. The cycle can continue until the end of the last undulator segment.

As the cycle continues, the microbunch moves towards the bottom of the ponderomotive bucket. Close to the bottom of the bucket, further phase jumps will move the microbunch out of the bucket. In other words, we can divide the energy extraction process beyond the initial saturation point into three main stages: (i) the in-bucket regime, (ii) the out-of-bucket regime, and (iii) the final saturation regime.

With an appropriate choice of the target phase $\psi_{\rm targ}$ in every phase jump, we can have $\Delta\eta_{\rm segm} < 0$ in every undulator segment between the initial saturation and the final saturation. Obtaining the precise value of the optimal $\psi_{\rm targ}$ is a matter of empirical phase scan. But from a theoretical perspective, there are general criteria for a good choice of $\psi_{\rm targ}$ within the deceleration quadrants.

H. In-bucket regime

The in-bucket regime is the first stage beyond the initial saturation point. At this stage, microbunch deceleration takes place along the closed orbits within the ponderomotive bucket.

1. *Lower bound for good target phase*

In the single-cycle microbunch deceleration illustrated in Fig. 3, the energy extraction is the most efficient if the average particle stays within the deceleration quadrants throughout the entire undulator segment, and never manages to enter quadrant III. For this to be the case, the chosen target phase $\psi_{\rm targ}$ must satisfy the criterion

$$\begin{aligned} &\psi_{\rm targ} - |\Delta\psi_{\rm segm}| \geq 0 \\ &\qquad \Leftrightarrow \psi_{\rm targ} \geq |\Delta\psi_{\rm segm}|. \end{aligned} \tag{16}$$

In order to proceed from here, we obtain an expression for $\Delta\psi_{\rm segm}$ by integrating both sides of Eq. (7) with respect to z over one undulator segment. This yields

$$|\Delta\psi_{\rm segm}| = 2k_u \left| \int_{z'}^{z'+L_{\rm segm}} \bar{\eta}(z) dz \right|. \tag{17}$$

Within the undulator segment, we expect the average particle to decelerate, and $\bar{\eta}(z)$ should therefore be more negative than the original value $\eta_{\rm orig}$ right before the undulator segment. Hence,

$$|\Delta\psi_{\rm segm}| \geq 2k_u |\eta_{\rm orig}| L_{\rm segm}. \tag{18}$$

Combining the inequalities (16) and (18), we obtain the lower bound $\psi_{\rm min}$ for the choice of $\psi_{\rm targ}$:

$$\psi_{\rm targ} \geq 2k_u |\eta_{\rm orig}| L_{\rm segm} \equiv \psi_{\rm min}. \tag{19}$$

When configuring each phase shifter, $\psi_{\rm targ}$ needs to be at least $\psi_{\rm min}$, for the average particle to *have a chance* of avoiding the acceleration quadrants. If $\psi_{\rm targ}$ is less than $\psi_{\rm min}$, then the average particle will *definitely* enter quadrant III within the upcoming undulator segment.

2. *Upper bound for good target phase*

During the in-bucket regime, we should keep the average particle in the bucket as long as possible. This allows us to fully exploit the in-bucket regime before the average particle becomes detrapped.

Thus, the upper bound $\psi_{\rm max}$ for the target phase $\psi_{\rm targ}$ is given by the separatrix in the deceleration quadrants (see Fig. 3). This can be expressed mathematically as

$$H(\psi_{\rm max}, \eta_{\rm orig}) = H_{\rm sep}. \tag{20}$$

To proceed from Eq. (20), we can substitute the right-hand side by Eq. (11), and the left-hand side by Eq. (10) with $(\psi, \eta) = (\psi_{\rm max}, \eta_{\rm orig})$. Cognizant of the fact that $0 \leq \psi_{\rm max} \leq \pi$, we can then solve for $\psi_{\rm max}$, and obtain the expression

$$\psi_{\rm max} = 2 \arccos\left(\frac{k_u^2 |\eta_{\rm orig}|}{\Omega^2} \right). \tag{21}$$

This is the upper bound for the choice of $\psi_{\rm targ}$, in order to avoid entering the out-of-bucket regime.

3. *Undulator segment length*

Within the first few cycles of the mechanism depicted in Fig. 3, the average particle should have reached the $\eta < 0$ region, i.e. quadrants II and III. For the microbunch deceleration to be efficient, the average particle should stay within quadrant II, without entering quadrant III. However, this will not be possible if $\Delta\psi_{\rm segm}$ is too large (see Fig. 3). From the inequality (18), we notice that $\Delta\psi_{\rm segm}$ increases with the undulator segment length $L_{\rm segm}$. This imposes an upper limit on $L_{\rm segm}$.

As a particle undergoes one complete orbit in the ponderomotive bucket, it travels down the undulator magnet by a distance of one synchrotron period $L_{\rm sync} = 2\pi/\Omega$. As the particle sweeps across one quadrant in the bucket, it undergoes a quarter of a complete orbit, and travels down the undulator magnet by a distance of $L_{\rm sync}/4$.

Thus, for the average particle to stay within a single quadrant (namely, quadrant II), an undulator segment should be no longer than $L_{\rm sync}/4$. Since $L_{\rm sync}$ varies with z, the requirement for the undulator segment length is

$$L_{\rm segm} < \frac{1}{4}\min[L_{\rm sync}(z)]. \tag{22}$$

I. Regime transition

As the microbunch deceleration cycle continues, the relative energy deviation $\bar{\eta}$ of the average particle becomes more and more negative, meaning that $|\eta_{\rm orig}|$ becomes larger with every phase jump.

Throughout the in-bucket regime, $\psi_{\rm min}$ increases with $|\eta_{\rm orig}|$ according to Eq. (19), and $\psi_{\rm max}$ decreases with $|\eta_{\rm orig}|$ according to Eq. (21). As the average particle is close to the bottom of the bucket, we will eventually encounter a scenario where $\psi_{\rm min} > \psi_{\rm max}$.

In such a scenario, it is no longer possible to choose a target phase $\psi_{\rm targ}$ in the range of $\psi_{\rm min} \le \psi_{\rm targ} \le \psi_{\rm max}$. We are then forced to choose $\psi_{\rm targ} > \psi_{\rm max}$, and move the average particle out of the bucket. This marks the end of the in-bucket regime, and the beginning of the out-of-bucket regime.

J. Out-of-bucket regime

In the out-of-bucket regime, the trajectories in the longitudinal phase space (ψ, η) are unbounded. Nonetheless, microbunch deceleration is possible. The mechanism is similar to that in the in-bucket regime, and is illustrated in Fig. 4.

1. *Deceleration efficiency*

The deceleration efficiency in each undulator segment depends on the slope of the particle trajectory in the deceleration quadrants of the (ψ, η) space. The steeper is the slope, the higher is the rate at which a particle loses energy.

The slope is given by the derivative $d\eta/d\psi$. Dividing Eq. (6) by Eq. (7), we can obtain an expression for the derivative as follows:

$$\left|\frac{d\eta}{d\psi}\right| = \frac{\Omega^2}{4k_u^2|\eta|}\sin\psi. \tag{23}$$

Note that in the deceleration quadrants, we have $0 \le \psi \le \pi$ and hence $0 \le \sin\psi \le 1$. As a result, $|d\eta/d\psi|$ is inversely proportional to $|\eta|$, and the deceleration efficiency decreases with $|\eta|$.

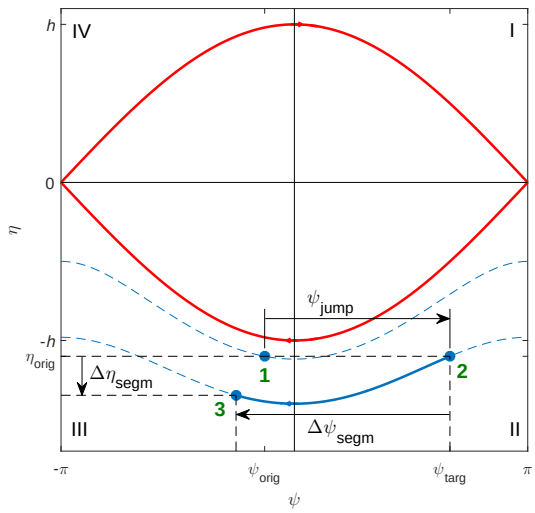

FIG. 4. The microbunch deceleration cycle as illustrated by the movement of the average particle outside the bucket. Position 1 corresponds to the start point of a drift section, position 2 the end point of the same drift section, and position 3 the end point of the subsequent undulator segment.

For the in-bucket regime, $|\eta| < h$. For the the out-of-bucket regime, $|\eta| > h$. Thus, the deceleration efficiency is lower in the out-of-bucket regime than in the in-bucket regime. As the microbunch deceleration cycle continues, the deceleration efficiency decreases with every undulator segment.

2. *Lower bound for good target phase*

For the in-bucket regime, the deceleration in an undulator segment can be made more efficient by keeping the average particle in the deceleration quadrants and preventing it from entering the acceleration quadrants. This argument also applies to the out-of-bucket regime. Thus, the lower bound for a good $\psi_{\rm targ}$ in the out-of-bucket regime is also given by Eq. (19):

$$\psi_{\rm min} = 2k_u|\eta_{\rm orig}|L_{\rm segm}.$$

3. *Upper bound for good target phase*

In the out-of-bucket regime, the average particle is already outside the bucket. The separatrix does not impose any limit on $\psi_{\rm targ}$. In principle, the upper limit of $\psi_{\rm targ}$

in the out-of-bucket regime is π, which is the maximum phase in the deceleration quadrants.

However, it is not favourable to let the average particle get too close to π, or a fraction of the particles within the microbunch will leak into the $\pi < \psi < 3\pi$ region, which corresponds to the acceleration quadrants associated with the bucket ahead. In that region, particles absorb energy from the optical field.

The precise upper bound for the choice of ψ_{targ} depends on the ψ spread of the microbunch. But roughly speaking, the upper bound for a good ψ_{targ} is *slightly below* π.

K. Final saturation regime

According to the relation (18), $|\Delta\psi_{\text{segm}}|$ increases with $|\eta_{\text{orig}}|$. At some point in the out-of-bucket regime, $|\eta_{\text{orig}}|$ will have become so large that

$$|\Delta\psi_{\text{segm}}| = \pi. \tag{24}$$

This signifies the onset of the final saturation regime.

Beyond that point, it is no longer possible to prevent the average particle from moving into quadrant III within a single undulator segment, regardless of the choice of ψ_{targ} (see Fig. 4). The microbunch deceleration cycle then becomes inefficient, and $\Delta\eta_{\text{segm}}$ approaches zero.

As $\Delta\eta_{\text{segm}}$ approaches zero, the inequality (18) can be approximated by

$$|\Delta\psi_{\text{segm}}| \approx 2k_u|\eta_{\text{orig}}|L_{\text{segm}} \equiv \psi_{\min}. \tag{25}$$

With this approximation, the relative energy deviation at the onset of the final saturation regime is then

$$|\eta_{\text{orig}}| = \frac{\pi}{2k_u L_{\text{segm}}}. \tag{26}$$

The final saturation point is reached when $\Delta\eta_{\text{segm}} \geq 0$, i.e. when it is no longer possible to maintain a net transfer of energy from microbunch to the optical field.

L. Small subtlety about phase jump

When using a non-isochronous phase shifter, it is important to note that the specified phase jump is only valid for particles at a certain reference energy. In other words, a particle which is not at the reference energy experiences a different phase jump from the specified value.

In applying the phase jump method, it is convenient to use the resonant energy $\gamma_R m_e c^2$ as the reference energy, as it is constant. But in our model, we are mainly concerned about the phase jump applied to the average particle, which has $\gamma \neq \gamma_R$ in general. Therefore, we need a conversion formula between the phase jump $\psi^{\text{A}}_{\text{jump}}$ for the average particle and the phase jump $\psi^{\text{R}}_{\text{jump}}$ for particles at the resonant energy.

To obtain such a conversion formula, we model the phase-shifting chicane as a one-period undulator, with undulator period $\hat{\lambda_u}$ and deflection parameter $\hat{K}$. After the one undulator period, the slippage $\hat{\lambda}$ is given by

$$\hat{\lambda} = \frac{\hat{\lambda_u}}{2\gamma^2}\left(1 + \frac{\hat{K}^2}{2}\right). \tag{27}$$

For particles at the resonant energy, $\gamma = \gamma_R$. The slippage $\hat{\lambda}$ is related to the phase jump $\psi^{\text{R}}_{\text{jump}}$ by

$$\frac{\psi^{\text{R}}_{\text{jump}}}{2\pi} = -\frac{\hat{\lambda}}{\lambda}, \tag{28}$$

where λ (without the caret) is the actual radiation wavelength of the FEL. The negative sign in the equation arises from the sign convention of $\psi^{\text{R}}_{\text{jump}}$.

In general, the average particle has $\gamma \neq \gamma_R$. In the same one-period undulator, the average particle experiences a different slippage $\hat{\lambda} + \Delta\hat{\lambda}$, which is related to the phase jump $\psi^{\text{A}}_{\text{jump}}$ by

$$\frac{\psi^{\text{A}}_{\text{jump}}}{2\pi} = -\frac{\hat{\lambda} + \Delta\hat{\lambda}}{\lambda}, \tag{29}$$

To proceed from here, we take the differential on both sides of Eq. (27), and obtain

$$\begin{aligned}\Delta\hat{\lambda} &= \frac{\hat{\lambda_u}}{2}\left(1 + \frac{\hat{K}^2}{2}\right)\left(\frac{-2\Delta\gamma}{\gamma^3}\right) \\ &= -2\hat{\lambda}\frac{\Delta\gamma}{\gamma} = -2\hat{\lambda}\bar{\eta}.\end{aligned} \tag{30}$$

As usual, $\bar{\eta}$ is the relative energy deviation of the average particle. Using Eqs. (28), (29) and (30), we can eliminate λ, $\hat{\lambda}$ and $\Delta\hat{\lambda}$. This results in the conversion formula

$$\psi^{\text{A}}_{\text{jump}} = \psi^{\text{R}}_{\text{jump}}(1 + 2\bar{\eta}). \tag{31}$$

M. Comparison with undulator tapering

Apart from the phase jump method, undulator tapering is another common technique for efficiency enhancement in FELs. In this subsection, we compare and contrast the two techniques. In particular, we discuss the similarities and differences between our phase jump model and the classic Kroll-Morton-Rosenbluth (KMR) model [10] of undulator tapering.

Both models make use of one-dimensional Hamiltonian mechanics to describe the particle dynamics in the longitudinal phase space (ψ, η). The KMR tapering model follows the motion of a resonant particle, which defines the stable point in the middle of the ponderomotive bucket. Our phase jump model follows the motion of the average particle within the microbunch.

In the KMR model, we directly control the undulator parameter K, and move the resonant particle vertically

in the (ψ, η) space. In our phase jump model, we directly control the phase jump $\psi_{\rm jump}$, and move the average particle horizontally in the (ψ, η) space.

In both models, the energy extraction is sustained beyond the initial saturation point by bringing a fraction of particles towards lower energies. As these particles decelerate, energy is transferred to the optical field, due to the conservation energy.

However, the underlying principle of the particle deceleration is different in the two models. In the KMR model, particle deceleration relies on the deceleration of the bucket itself. In our phase jump model, particle deceleration relies on the microbunch deceleration cycle.

In the KMR model, the bucket moves towards lower energies during the energy extraction. In this process, the phase of the resonant particle increases, and the width of the bucket decreases. In our phase jump model, the bucket is stationary, and does not reduce in width. During the energy extraction process, the optical field amplitude increases, and the height of the bucket increases.

In the KMR model, particles need to be trapped in the bucket in order to decelerate. In our phase jump model, the microbunch deceleration cycle continues in the out-of-bucket regime. Energy extraction outside the bucket is impossible for the former, but possible for the latter.

In the KMR model, the efficiency of particle deceleration is determined by the rate at which the bucket decreases in energy. This, in turn, depends on the dK/dz, the rate at which the undulator parameter decreases along the undulator line. In the phase jump model, the efficiency of particle deceleration is determined by $d\eta/d\psi$, the slope of the particle trajectory in the longitudinal phase space. This, in turn, depends on the relative energy deviation $\bar{\eta}$ of the average particle, as evident by Eq. (23).

In the KMR model, the undulator segment length required for the efficient deceleration of particles is $L_{\rm segm} < \min[L_{\rm sync}(z)]$, as discussed in Ref. [12]. In our phase jump model, the requirement is $L_{\rm segm} < \min[L_{\rm sync}(z)]/4$, which is a more stringent one.

In the KMR model, the main causes of the final saturation are the weakening of refractive guiding and the detrapping of particles. In our phase jump model, the main causes of the final saturation are the decrease of $|d\eta/d\psi|$ and increase of $|\Delta\psi_{\rm segm}|$ with particle energy.

III. STEADY-STATE SIMULATION

A. Case definition

So far, our physics model of the phase jump method is a one-dimensional and steady-state one. For the purpose of verifying the model, we perform a three-dimensional and steady-state simulation study, using the numerical simulation code GENESIS [15].

We first define a case for the simulation study. The main parameters are listed in Table I.

TABLE I. Parameters of the steady-state simulation.

Parameter	Symbol	Value
Electron beam energy	$\gamma m_e c^2$	5 GeV
Energy spread	σ_γ/γ	1×10^{-4}
Beam current	I	3 kA
Normalized emittance	$\varepsilon_{x,y}$	0.4 mm mrad
Average of beta function	$\bar{\beta}_{x,y}$	7 m
Radiation wavelength	λ	2 Å
Undulator period	λ_u	20 mm
Undulator parameter	K	1.35
Length of each undulator segment	$L_{\rm segm}$	1 m
Length of each drift section	$L_{\rm drift}$	0.2 m

In the chosen case, SASE is the start-up mechanism of the FEL. The effective shot-noise power is 830 W.

Planar undulator segments are used. Undulator tapering is not implemented.

The lattice for strong focusing is in a FODO configuration, with one quadrupole magnet in every other drift section. The length of the FODO cell is 4.8 m. Within the cell, the centres of the two quadrupole magnets are separated by a distance of 2.4 m. The length of each quadrupole magnet is 80 mm.

The strengths of the quadrupole magnets and the initial twiss parameters are matched self-consistently to give the average beta $\bar{\beta}_{x,y}$ specified in Table I.

In the GENESIS simulation, we place a phase shifter in every drift section, by putting an `AD` element in the external magnet file. We control the phase jump by setting the `AD` element to an appropriate value.

Here the undulator segment length of $L_{\rm segm} = 1$ m is smaller than what is used in most existing FEL facilities. The small $L_{\rm segm}$ is chosen to fulfill the requirement (22).

B. Initial saturation

In order to obtain information about the initial saturation point, we first run the simulation in the absence of phase jumps, by setting $\psi_{\rm jump} = 0$ for all drift sections.

The simulation shows that the initial saturation occurs at $z = 38.2$ m within the 32th undulator segment. The saturation power is 2 GW. At the initial saturation point, the bunching factor $b = |\langle e^{-i\psi}\rangle|$ is the highest, and has a value of 0.4.

C. Phase jump commencement

We then repeat the simulation with the introduction of phase jumps. We start the phase jumps in the vicinity of the initial saturation point, where the microbunching is fully developed. Thus, the first non-zero phase jump occurs in the drift section at $z = 37$ m, immediately preceding the 32th undulator segment. Meanwhile, we keep $\psi_{\rm jump} = 0$ for all the drift sections before $z = 37$ m.

While there are infinite possible sets of phase jumps, we shall discuss one chosen set which yields an increase in radiation power beyond the initial saturation. The phase jumps are obtained by coarse tuning within the selection criteria discussed in Section II.

It is possible to obtain even higher radiation power by fine-tuning the phase jump. However, the purpose of this simulation study is to verify the steady-state model, and not to perform a thorough optimization.

D. Radiation power evolution

Figure 5(a) shows the radiation power P as a function of z, for the chosen set of phase jumps. Along the radiation power curve, there are short, straight, horizontal sections, where the power is neither increasing nor decreasing. These sections correspond to the drift sections, where the radiation does not exchange energy with the electron beam.

After the first non-zero phase jump at $z = 37$ m, the radiation power continues to grow. Up until $z = 50$ m, the power grows monotonically. But after that, the power fluctuates. Within every undulator segment, the power first increases, and then decreases. Nonetheless, there is still a net power increase.

In the undulator segment which begins at $z = 64.8$ m, there is no longer a net power increase within an undulator segment. This indicates the arrival of the final saturation. The power at the final saturation is 36 GW, which is 18 times the power at the initial saturation.

The FEL efficiency can be defined as the power ratio of the output radiation to the injected electron beam. With this definition, the chosen set of phase jumps enhance the FEL efficiency by a factor of 18. It is possible to obtain an even larger enhancement factor by fine-tuning the phase jump values. But again, the purpose of this simulation study is to verify the model, and not to perform a thorough optimization.

E. Energy evolution of the average particle

We now turn our attention to the average particle within the microbunch. The relative energy deviation $\bar{\eta}$ of the average particle is defined by Eq. (14). Figure 5(b) shows $\bar{\eta}$ as a function of z.

Before the first non-zero phase jump at $z = 37$ m, $\bar{\eta}$ remains close to zero, meaning that the energy of the average particle is close to the resonant energy.

After the first non-zero phase jump at $z = 37$ m, $\bar{\eta}$ exhibits an overall decreasing trend. The energy of the average particle deviates further and further from the resonant energy. This is an evidence of microbunch deceleration.

As $\bar{\eta}$ becomes more and more negative, the rate of $\bar{\eta}$ decrease becomes lower and lower. This agrees with the prediction of Eq. (23).

Up until $z = 50$ m, $\bar{\eta}$ decreases monotonically. But after that, $\bar{\eta}$ fluctuates. Comparing Fig. 5(a) and (b), we notice that a decrease in $\bar{\eta}$ corresponds to an increase in P, and vice versa. This can be explained by the conservation of energy. When $\bar{\eta}$ decreases, the microbunch loses energy. This energy is transferred to the radiation, leading to an increase in P.

The onset of the final saturation regime is defined by Eq. (26). According to this definition, the final saturation regime begins when $\bar{\eta} = 5 \times 10^{-3}$. As seen in Fig. 5(b), this corresponds to $z = 55.5$ m.

F. Phase evolution of the average particle

The ponderomotive phase $\bar{\psi}$ of the average particle is defined by Eq. (14). Figure 5(c) shows $\bar{\psi}$ as a function of z. After the first non-zero phase jump at $z = 37$ m, $\bar{\psi}$ oscillates in z. The upward slopes coincide with the drift sections, while the downward slopes coincide with the undulator segments. In other words, a crest coincides with the start point of an undulator segment, while a trough coincides with the end point of an undulator segment.

In terms of the microbunch deceleration cycle (see Figs. 3 and 4), a crest corresponds to position 2, while a trough corresponds to position 1 or 3. The period of the oscillation is one microbunch deceleration cycle. The crest value of each cycle is the target phase ψ_{targ}. The phase change represented by an upward slope is ψ_{jump}, while the phase change represented by a downward slope is $\Delta\psi_{\text{segm}}$.

Figure 5(c) also shows the lower bound $\psi_{\min}$ and the upper bound $\psi_{\max}$ for the target phase ψ_{targ} in each drift section. The values are given by Eqs. (19) and (21). Recall that $\psi_{\max}$ is defined by the separatrix of the ponderomotive bucket in the $\psi \geq 0$ region, and that $\psi_{\min}$ is the minimum requirement for the average particle to avoid entering the $\psi < 0$ region.

In Fig. 5(c), the region immediately after the first non-zero phase jump at $z = 37$ m is the in-bucket regime, as evident by the fact that $\bar{\psi} < \psi_{\max}$. The decrease of $\psi_{\max}$ with z reflects that the average particle is moving towards the bottom of the bucket.

In the in-bucket regime, ψ_{targ} is made to increase with $\psi_{\min}$, so as to fulfill the requirement that $\psi_{\text{targ}} > \psi_{\min}$. As a result, the average particle is prevented from entering the $\psi < 0$ region. Within every undulator segment, the average particle transfers energy to the radiation, without absorbing energy from the radiation. This explains the monotonic decrease of $\bar{\eta}$ [see Fig. 5(b)].

Prior to $z = 46.5$ m, the choice of ψ_{targ} satisfies the requirement that $\psi_{\min} < \psi_{\text{targ}} < \psi_{\max}$. But in the vicinity of $z = 46.5$ m, the average particle is so close to the bottom of the bucket that we encounter the situation where $\psi_{\min} \approx \psi_{\max}$. We are then forced to choose $\psi_{\text{targ}} > \psi_{\max}$, thus placing the average particle outside the bucket. This marks the beginning of the out-of-bucket regime.

Even though the average particle is outside the bucket,

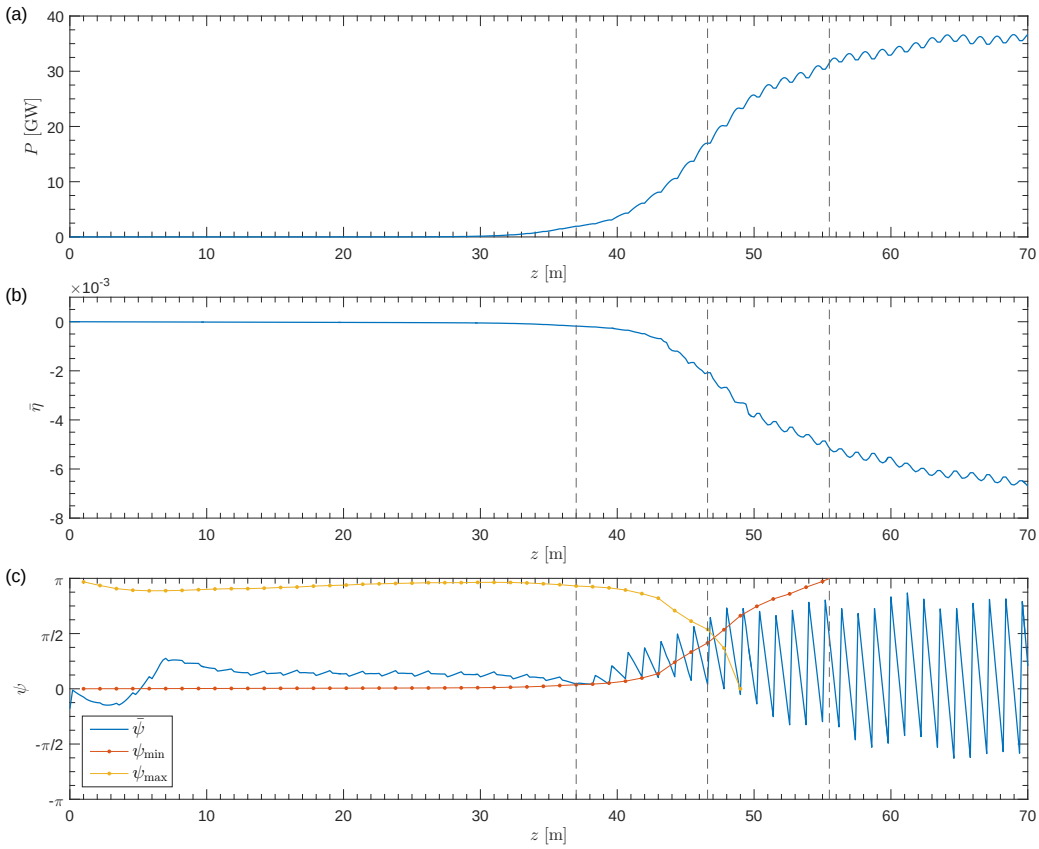

FIG. 5. Result of steady-state simulation. The following quantities are plotted as functions of the distance z along the undulator line: (a) the radiation power, (b) the relative energy deviation $\bar{\eta}$ of the average particle, and (c) the ponderomotive phase $\bar{\psi}$ of the average particle (in blue), together with the lower bound $\psi_{\min}$ (in red) and the upper bound $\psi_{\max}$ (in yellow) for the target phase ψ_{targ} in each drift section. The dashed vertical lines mark the beginning of the in-bucket, out-of-bucket and final saturation regimes.

a fraction of the particles in the microbunch are still inside the bucket. For the next two periods of the oscillation, a part of the microbunch follows the in-bucket trajectories, while a part of the microbunch follows the out-of-bucket trajectories. The average particle, tracing the average behaviour of the entire microbunch, moves in and out of the bucket. At $z = 49$ m, $\psi_{\max} = 0$, indicating that the average particle is at the same energy level as the lowest point of the bucket.

In the out-of-bucket regime, $\psi_{\min}$ continues to increase, and becomes closer and closer to π. However, we want to prevent the average particle from getting too close to π, or a fraction of the particles in the microbunch will enter the acceleration region associated with the bucket ahead. This concern forces us to choose $\psi_{\text{targ}} < \psi_{\min}$. The consequence is that the average particle enters the $\psi < 0$ region, thus absorbing energy from the radiation. Hence, $\bar{\eta}$ no longer decreases monotonically [see Fig. 5(b)]. Instead, $\bar{\eta}$ decreases and increases within a single undulator segment.

The final saturation regime begins at $z = 55.5$ m, where $\psi_{\min} = \pi$ [see Fig. 5(c)]. In this regime, it is no longer possible to prevent the average particle from entering the $\psi < 0$ region, regardless of the choice of ψ_{targ}. As the average particle enters deep into the $\psi < 0$ region, the energy extraction becomes far less effective.

G. Direct observation in phase space

Next, we observe the microbunch deceleration cycle directly in the longitudinal phase space (ψ, η). Figure 6

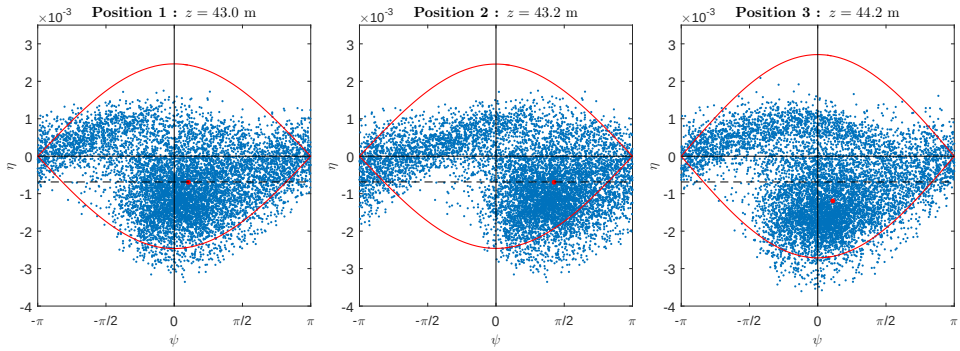

FIG. 6. Result of steady-state simulation. Snapshots in the longitudinal phase space (ψ, η) showing a microbunch deceleration cycle in the in-bucket regime. The red dot represents the average particle within the microbunch.

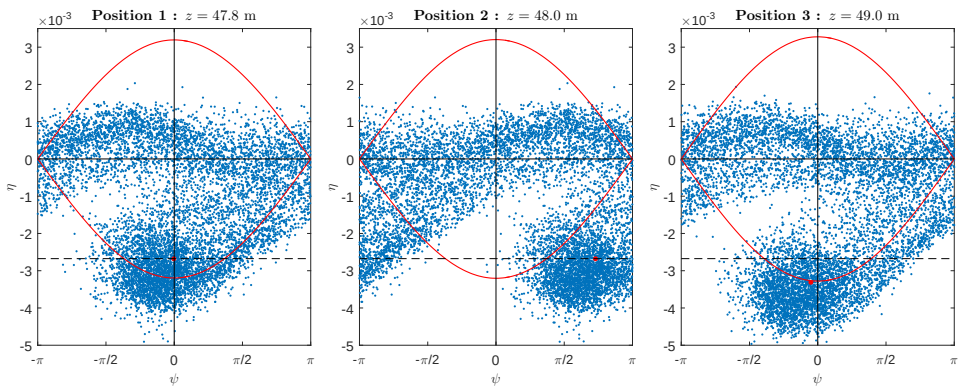

FIG. 7. Result of steady-state simulation. Snapshots in the longitudinal phase space (ψ, η) showing a microbunch deceleration cycle during the transition from the in-bucket regime to the out-of-bucket regime.

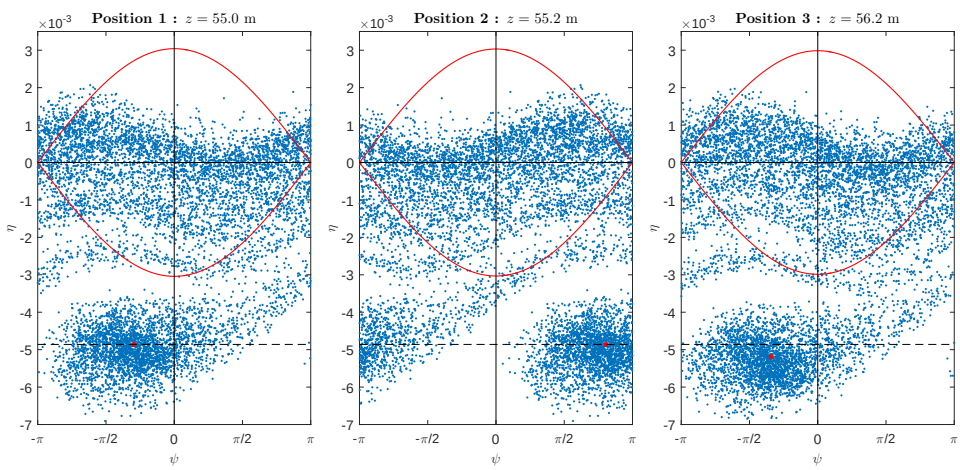

FIG. 8. Result of steady-state simulation. Snapshots in the longitudinal phase space (ψ, η) showing a microbunch deceleration cycle at the onset of the final saturation regime.

shows a cycle in the in-bucket regime. Figure 7 shows a cycle during the transition from the in-bucket regime to the out-of-bucket regime. Figure 8 shows a cycle at the onset of the final saturation regime.

In each of these phase space snapshots, the red curve represents the separatrix of the ponderomotive bucket, and the red dot represents the average particle. These snapshots clearly show that the electron beam remains microbunched along the undulator line. From these snapshots, it is also apparent that the microbunch moves towards lower η as z increases, verifying the microbunch deceleration once again.

In each cycle, position 1 corresponds to the start point of the drift section, position 2 the end point of the drift section, and position 3 the end point of the subsequent undulator segment.

In position 1 and position 2, the average particle has the same η. This is expected for an ideal phase shifter, wherein the phase jump ψ_{jump} changes only the phase, but not the energy, of the average particle.

In the transition from position 2 to position 3, the particles pass through an undulator segment, where there is energy exchange between the particles and the radiation. The energy exchange alters the bucket half-height h slightly. This is also expected, as h depends on the slowly varying optical field amplitude E_0 according to the proportionality (13).

In all the three cycles shown here, the average particle ends up with a lower η at position 3 than at position 1, meaning that there is a net energy transfer from the microbunch to the radiation in the undulator segment. The motion of the average particle in these snapshots reflects the mechanism depicted in Figs. 3 and 4.

H. Trace of the average particle

Figure 9 shows the trace of the average particle in the longitudinal phase space (ψ, η) over the entire undulator line. Within the trace, there are straight, horizontal sections, each representing the transition from position 1 to position 2 within a microbunch deceleration cycle.

As the average particle moves from high η to lower η, the η spacing between successive horizontal sections decreases, meaning that the amount of energy lost by the average particle decreases with every cycle. In other words, the deceleration efficiency decreases with η, as predicted by Eq. (23).

At $\eta \approx -6 \times 10^{-3}$, the η spacing between successive horizontal sections approaches zero. There is no longer a net energy transfer from the microbunch to the radiation. This indicates the arrival of the final saturation.

I. Undulator segment length

In the simulation, the synchrotron period L_{sync} varies as a function of z (data not shown). The smallest value is

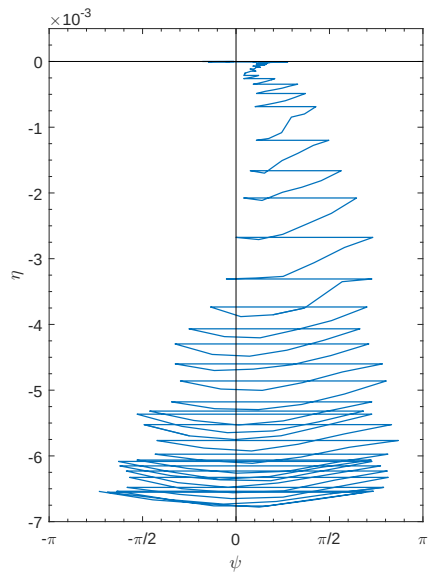

FIG. 9. Result of steady-state simulation. The trace of the average particle in the longitudinal phase space (ψ, η) over the entire undulator line.

$\min[L_{\text{sync}}(z)] = 5.9$ m, which occurs at $z = 49$ m. With a undulator segment length of $L_{\text{segm}} = 1$ m as specified in Table I, the requirement (22) is satisfied.

IV. TIME-DEPENDENT MODEL

A. Problem description

In this section, we extend the steady-state model of the phase jump method into a time-dependent model. As before, we consider the longitudinal profile of the electron bunch as a series of slices, each with a width of λ.

The steady-state model assumes all slices to be identical. For every slice, the optical field that slips into the slice ahead is identical to the optical field that comes in from the slice behind. This implies that the electron bunch has an infinite length and a constant current. The resulting FEL signal has only a single frequency component, and hence zero bandwidth.

The time-dependent model departs from these assumptions, and accounts for the interactions between distinct slices in a profile of finite length. For example, in a Gaussian profile, the current I at any position t within the electron bunch is given by

$$I(t) = I_0 e^{-\frac{t^2}{2\sigma_t^2}}, \tag{32}$$

where I_0 is the peak current and σ_t is the RMS bunch length.

B. Average average particle

There is one average particle for every slice. In the steady-state model, all average particles behave in the exact same manner, as all slices are identical. The optimal phase jump for any one average particle is also the optimal for the entire electron bunch.

In the time-dependent model, however, all these average particles generally have distinct $(\bar{\psi}, \bar{\eta})$ values at any given position z along the undulator line. The optimal phase jump for one average particle is generally not the optimal for another. In order to optimize the phase jump for the electron bunch as a whole, we need a compromise between all the average particles.

In obtaining the compromise, the average particles should not be treated equally, as the slices generally do not have the same charge. Thus, we propose to optimize the phase jump for an *average average particle*, which is the weighted average of all the average particles.

Let $(\bar{\bar{\psi}}, \bar{\bar{\eta}})$ be the coordinates of the average average particle in the longitudinal phase space. They can be defined as

$$\bar{\bar{\eta}} \equiv \sum_{\mu} w_{\mu} \bar{\eta}_{\mu}, \tag{33}$$

$$\bar{\bar{\psi}} \equiv \arg\left(\sum_{\mu} w_{\mu} e^{-i\bar{\psi}_{\mu}} \right), \tag{34}$$

where

$$w_{\mu} = \frac{I(t_{\mu})}{\sum_{\nu} I(t_{\nu})} \tag{35}$$

is the weighting factor based on the slice current $I(t_{\mu})$.

Note that the definitions (33), (34) and (35) are applicable to any electron profile, and not specifically to a Gaussian profile. With these definitions, the higher is the current in a slice, the better is the slice represented by the average average particle.

C. Ansatz for optimization

In the steady-state model, the average particle of a single slice is put through the microbunch deceleration cycles depicted in Figs. 3 and 4. The deceleration of the average particle is optimized by choosing an appropriate target phase $\bar{\psi} = \psi_{\mathrm{targ}}$ for each cycle.

In the time-dependent model, this same mechanism is applicable to the average average particle of the entire electron bunch. The deceleration of the average average particle is optimized by choosing an appropriate target phase $\bar{\bar{\psi}} = \psi_{\mathrm{targ}}$ for each cycle.

For the average average particle, the in-bucket and out-of-bucket regimes can be defined in relation to an imaginary bucket with half-height h determined by the optical field amplitude E_0 averaged over all slices. The selection criteria for ψ_{targ} then remain the same as in the steady-state model. In this subsection, we develop an ansatz for the optimal evolution of ψ_{targ} along the undulator line, based on these selection criteria.

Among the selection criteria, the most important one is the common lower bound ψ_{min} in both the in-bucket and out-of-bucket regimes, given by Eq. (19). This criterion is a necessary condition for the microbunch to have a net deceleration, $\Delta\eta_{\mathrm{segm}} < 0$, within an undulator segment.

In contrast, the upper bound ψ_{max} in the in-bucket regime, given by Eq. (21), is not as crucial. Even if ψ_{targ} exceeds ψ_{max} by a small amount, the energy extraction can still continue in the out-of-bucket regime.

According to Eq. (19), ψ_{min} increases with $|\bar{\bar{\eta}}|$ of the average average particle. Beyond the initial saturation point, $|\bar{\bar{\eta}}|$ increases gradually from zero as the electrons decelerate. Hence, ψ_{min} is expected to increase gradually from zero, and this is precisely the observation in the steady-state simulation [see Fig. 5(c)]. It is therefore logical that the optimal ψ_{targ} should increase with every phase shift.

However, ψ_{targ} cannot increase indefinitely, due to the upper bound in the out-of-bucket regime. The upper bound is a chosen value ψ_1, which is slightly less than π. This criterion is a necessary condition for preventing a microbunch from leaking into the acceleration quadrants associated with the bucket ahead. Therefore, the optimal ψ_{targ} should increase gradually beyond the initial saturation point only until it reaches ψ_1, and remains at ψ_1 for all subsequent phase shifts.

We label the phase shifters along the undulator line with the index $m \in \{1, 2, ...\}$. Suppose that the initial saturation point is in the vicinity of $m = m_0$. Then, all the phase shifters with $1 \leq m \leq m_0$ should be configured for $\psi_{\mathrm{jump}} = 0$, or equivalently, $\psi_{\mathrm{targ}} = \psi_{\mathrm{orig}}$. For $m > m_0$, we propose the following ansatz for the optimal evolution of ψ_{targ}:

$$\psi_{\mathrm{targ}}(m) = \begin{cases} \psi_1 \times \dfrac{m - m_0}{m_1 - m_0} & \text{for } m_0 < m < m_1 \\ \psi_1 & \text{for } m \geq m_1. \end{cases} \tag{36}$$

The growth of ψ_{targ} is chosen to be linear for simplicity, and the phase shifter $m = m_1$ defines where ψ_{targ} reaches ψ_1 for the first time.

The expression (36) can be regarded as a *functional form*, with every value of the parameter m_1 yielding a different function $\psi_{\mathrm{targ}}(m)$.

D. Sideband suppression

Sideband instability is a known issue of the FEL. It was first predicted theoretically [16] and observed experimentally [17] in the 1980s.

The origin of sideband instability is the synchrotron oscillations during the FEL interaction. In the longitudinal phase space (ψ, η), trapped electrons orbit around the

stable centroid of the bucket, thus oscillating back and forth in ψ at an angular frequency Ω given by Eq. (8). These oscillations give rise to a longitudinal modulation of amplitude and phase in the optical pulse.

The modulation manifests itself in the FEL spectrum as sidebands at parasitic wavelengths. The wavelength offset of these sidebands from the desired central wavelength λ is given by [16]

$$\frac{\Delta\lambda}{\lambda} = \pm\frac{\lambda_u}{L_{\rm sync}}, \tag{37}$$

where $L_{\rm sync} = 2\pi/\Omega$ is the synchrotron period.

When the sidebands are amplified, a significant fraction of optical power is drawn from the central wavelength to the parasitic wavelengths. This degrades the spectral purity and the efficiency of the FEL.

In the steady-state model, the FEL efficiency is determined solely by the fraction of the electron beam's power that is converted into optical power. In the time-dependent model, the FEL efficiency is determined also by the power ratio between the central wavelength and the sidebands. Even with a high optical power extracted from the electron beam, the FEL can still be inefficient if much of the optical power is channelled to the sidebands instead of the central wavelength.

For undulator tapering, sideband growth can be significantly detrimental to the amplification of the central wavelength, especially when the post-saturation undulator section is multiple synchrotron periods long. This is discussed in Refs. [10], [18] and [19].

While synchrotron oscillations are responsible for the sideband growth, the phase jump method has the potential to suppress the sideband growth by disrupting the synchrotron oscillations.

In the longitudinal phase space, a complete orbit within the bucket corresponds to a full period of synchrotron oscillation. In the in-bucket microbunch deceleration cycle depicted in Fig. 3, the trajectory of the particle from position 2 to position 3 is a portion of a complete orbit. In every cycle, the orbit is disrupted by the applied phase jump, which brings the particle from position 1 to position 2.

Provided that the undulator segment length $L_{\rm segm}$ satisfies the requirement (22), the particle will never manage to make a complete orbit after the initial saturation.

V. TIME-DEPENDENT SIMULATION

A. Case definition

In this section, we conduct a three-dimensional and time-dependent simulation study, using the same simulation code GENESIS [15]. In particular, we apply the ansatz (36) and optimize the phase jumps for the average average particle.

The purpose of this simulation study is two-fold: (i) to demonstrate that the phase jump method remains valid when time-dependent effects are taken into account; and (ii) to compare the phase jump method to undulator tapering in terms of efficiency.

The case chosen for the simulation study is a seeded FEL, using longer undulator segments than in the previous simulation. The longitudinal profile of the electron bunch is a Gaussian function. The main parameters are listed in Table II.

TABLE II. Parameters of the time-dependent simulation.

Parameter	Symbol	Value
Electron beam energy	$\gamma m_e c^2$	16 GeV
Energy spread	σ_γ/γ	1×10^{-4}
Peak current	I_0	4 kA
RMS bunch length	σ_t	1 μm
Normalized emittance	$\varepsilon_{x,y}$	0.3 mm mrad
Average of beta function	$\bar{\beta}_{x,y}$	10 m
Radiation wavelength	λ	1 Å
Seed radiation power	$P_{\rm seed}$	5 MW
Undulator period	λ_u	40 mm
Default undulator parameter	K	2.79
Length of each undulator segment	$L_{\rm segm}$	4 m
Length of each drift section	$L_{\rm drift}$	1 m

To examine the performance of the FEL over a longer distance, we simulate the undulator line from $z = 0$ up to $z = 200$ m.

At $\lambda = 1$ Å, no suitable external laser is available. The seed radiation essentially needs to come from self-seeding. The production mechanism of the seed radiation is beyond the scope of this simulation study. Therefore, we input the seed radiation at $z = 0$ without any regard to how it is produced.

The lattice for strong focusing is in a FODO configuration, with one quadrupole magnet in every drift section. The length of the FODO cell is 10 m. Within the cell, the centres of the two quadrupole magnets are separated by a distance of 5 m. The length of each quadrupole magnet is 80 mm.

The strengths of the quadrupole magnets and the initial twiss parameters are matched self-consistently to give the average beta $\bar{\beta}_{x,y}$ specified in Table II.

B. Optimization results

The initial saturation point is located at $z = 44$ m, i.e. the end of the 9th undulator segment, where the optical pulse energy is 22 μJ.

For the phase jump method, we set $m_0 = 8$ in the ansatz (36), so that the first non-zero phase jump takes place immediately after the 9th undulator segment. Furthermore, we arbitrarily set $\psi_1 = 170^\circ = 2.97$ rad for simplicity. We then scan the parameter m_1 for the highest optical pulse energy at the final saturation, and this optimization process yields $m_1 = 16$. The synchrotron period has a minumum value of 24 m. With the undula-

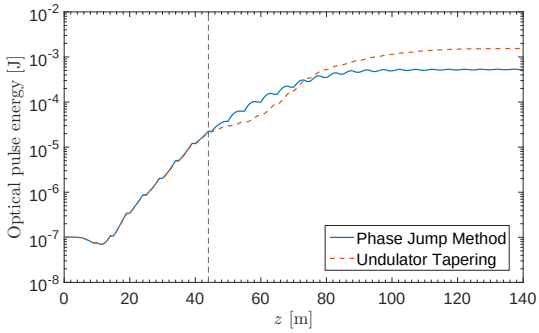

FIG. 10. Result of time-dependent simulation. The optical pulse energy is plotted as a function of the distance z along the undulator line for the optimal phase jumps (blue) and the optimal taper (red). The dashed vertical line indicates the common start point for the phase jump method and the taper. The vertical axis is on a logarithmic scale.

tor segment length of 4 m, the requirement (22) is well satisfied.

For undulator tapering, we use the same start point as for the phase jump method, so as to obtain a fair comparison. Immediately after the 9th undulator segment, the undulator parameter decreases quadratically with every segment, but remains uniform *within* every segment. We then scan the taper strength $\Delta K/K$ for the highest optical pulse energy at the final saturation, and this optimization process yields $\Delta K/K = 8$ %. The taper strength $\Delta K/K$ is defined such that K is the default undulator parameter in resonance with the initial energy of the electron beam, and $K - \Delta K$ is the parameter of the last segment before $z = 200$ m.

C. Evolution of the optical pulse energy

Figure 10 shows the evolution of the optical pulse energy with z for the optimal phase jumps and the optimal taper. The dashed vertical line indicates the initial saturation point, which is the common start point for the phase jump method and the undulator taper.

For the phase jump method, the final saturation occurs at $z = 100$ m. The optical pulse energy at the final saturation is 0.53 mJ, which is 24 times higher than that at the initial saturation. This enhancement in the optical pulse energy shows that the phase jump method remains valid in the presence of time-dependent effects.

For the undulator taper, the final saturation occurs at $z = 130$ m. The optical pulse energy at the final saturation is 1.5 mJ, which is three times the value for the phase jump method.

Comparing the undulator taper and the phase jump method, the former extracts a larger fraction of the electron beam's energy in the chosen case. However, this is true only when the undulator line is long enough for the energy extraction to reach the final saturation.

Immediately after the initial saturation, the phase jump method exhibits a faster growth in optical pulse energy (see Fig. 10). This is because the phase jump method allows particles to decelerate more rapidly in the region immediately following the initial saturation.

For tapering, the *particle trapping region* [11] comes right after the initial saturation point. In this region, a mild taper is needed to capture particles into the shrinking and descending bucket. A milder taper corresponds to a slower deceleration of the trapped particles.

In contrast, the phase jump method does not require such trapping process, as the microbunch deceleration cycle can take place both in and out of the bucket. Particles can be made to decelerate rapidly right after the initial saturation.

D. Evolution of the optical spectrum

Figure 11 illustrates the evolution of the optical spectrum for the optimal taper, with the snapshots at six positions along the undulator line. Figure 12 shows the corresponding snapshots for the optimal phase jumps.

In each snapshot, the spectral power is normalized to that at the central wavelength, to help compare the power ratio between the central wavelength and any sideband. Furthermore, the same binning for $\Delta\lambda/\lambda$ is used in all the snapshots.

In Fig. 11 for the optimal taper, snapshot (d) corresponds to the vicinity of the final saturation. Before the normalization, the absolute power at the central wavelength is 0.12 TW/fm.

In Fig. 12 for the optimal phase jumps, snapshot (c) corresponds to the vicinity of the final saturation. Before the normalization, the absolute power at the central wavelength is 0.14 TW/fm, close to the corresponding value for the optimal taper.

In the FEL interaction, it is the central wavelength that we intend to amplify. At the final saturation, even though the taper extracts more energy from the electron beam, it does not channel more energy to the central wavelength than the phase jumps do.

If we define the FEL efficiency in terms of the absolute spectral power at the central wavelength upon the final saturation, then the phase jump method and undulator tapering are almost equally as efficient in this case.

Between the initial and final saturations, the synchrotron period L_{sync} has a mean value of 29 m for the taper, and 30 m for the phase jumps. The values for the taper and the phase jumps are almost identical. According to Eq. (37), the synchrotron oscillations trigger the growth of sidebands around $\Delta\lambda/\lambda = \pm\, 1.5 \times 10^{-3}$.

For the taper, there is significant growth of sidebands around these wavelengths after the initial saturation (see Fig. 11). In the vicinity of the final saturation, the sideband power even exceeds 40 % of the central wavelength

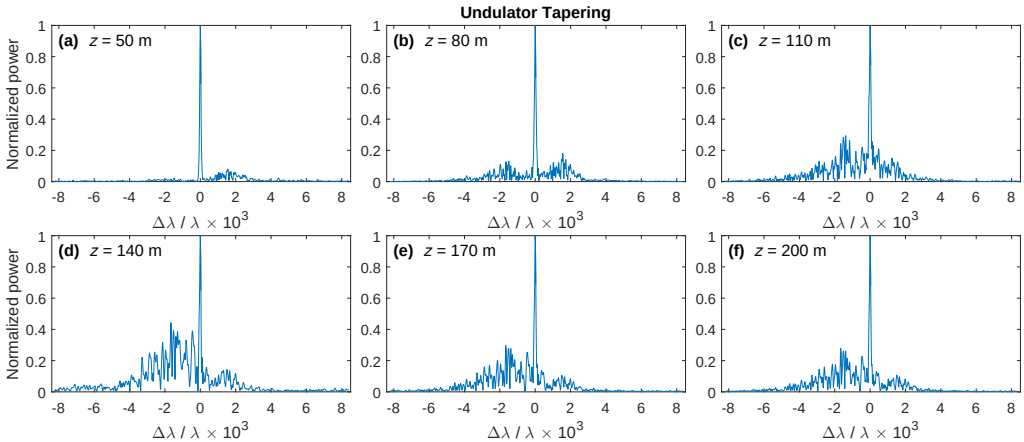

FIG. 11. Result of time-dependent simulation. The evolution of the optical spectrum for the optimal taper is illustrated with the snapshots at six positions along the undulator line.

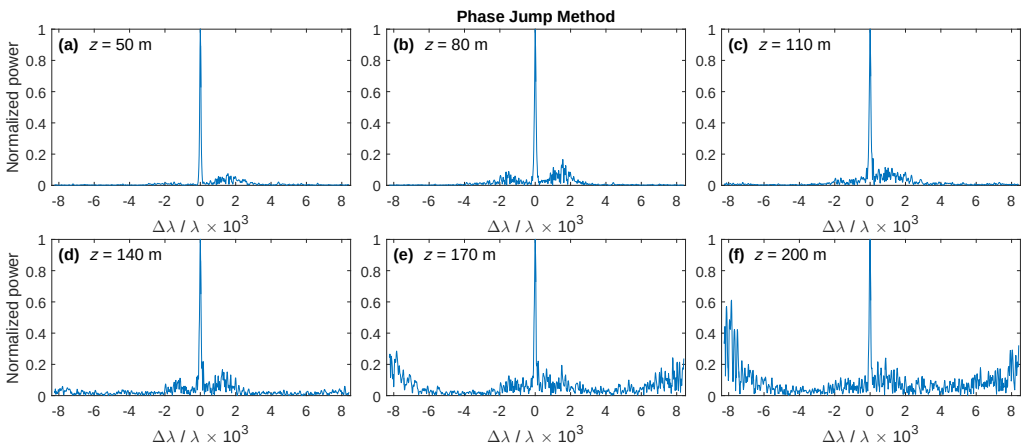

FIG. 12. Result of time-dependent simulation. The evolution of the optical spectrum for the optimal phase jumps is illustrated with the snapshots at six positions along the undulator line.

power [see Fig. 11(d)].

For the phase jumps, there are also sidebands growing around these wavelengths, but the power remains mostly below 20 % of that at the central wavelength (see Fig. 12).

Beyond the final saturation, new sidebands emerge around $\Delta\lambda/\lambda = \pm\, 8\times10^{-3}$ [see Fig. 12(e)–(f)]. However, these new sidebands can be prevented by disengaging all the undulator segments located downstream of the final saturation point.

From these results, it is apparent that the phase jump method is more effective in suppressing the synchrotron sidebands around $\Delta\lambda/\lambda = \pm\ 1.5 \times 10^{-3}$. Out of the energy extracted from the electron beam, a smaller fraction is channelled to the sidebands, and a larger fraction is channelled to the central wavelength.

Hence, if we define the FEL efficiency in terms of the power ratio between the central wavelength and the sideband, then the phase jump method is more efficient than undulator tapering in this case.

E. Phase jumps and the driven oscillator

It is apparent from Eq. (9) that the synchrotron motion in ψ is mathematically equivalent to the simple pendulum, which is a simple harmonic oscillator at small ψ.

The applied phase jumps act as a periodic external driving force, turning the system into a driven oscillator. The period of the driving force is the distance between successive phase shifters, given by $L_{\mathrm{segm}} + L_{\mathrm{drift}}$.

In this driven oscillator, there is a competition between the natural period and the driving period. By disrupting the synchrotron oscillations, the driving force channels power away from the sidebands associated with the natural period, which emerge at optical wavelengths given by Eq. (37). This explains the suppression of these sidebands in Fig. 12.

Beyond the final saturation, the optical field amplitude no longer grows. Furthermore, as the microbunch is out of the bucket, the trajectories in (ψ, η) do not form closed orbits, and synchrotron motion no longer has a natural period. The competition is then dominated by the driving force. In analogy to Eq. (37), the periodic driving force can trigger new sidebands at

$$\frac{\Delta\lambda}{\lambda} = \pm\frac{\lambda_u}{L_{\mathrm{segm}} + L_{\mathrm{drift}}}. \tag{38}$$

With the parameter values in Table II, Eq. (38) predicts the new sidebands to occur at $\Delta\lambda/\lambda = \pm\, 8 \times 10^{-3}$. This agrees with the observation in Fig. 12(e)–(f).

According to Eq. (38), it is, in principle, possible to influence the new sidebands by varying L_{segm} and L_{drift} as functions of z.

VI. COMBINING PHASE JUMPS AND TAPER

In our time-dependent simulation, undulator tapering yields a higher optical pulse energy at the final saturation. However, the phase jump method is more effective in suppressing the synchrotron sidebands, thus channelling a larger fraction of the optical energy to the desired central wavelength. This provides a motivation for combining the strengths of the two techniques.

In a recent simulation study by Duris *et al.* [20], a strong taper is used for the rapid deceleration of electrons, while phase shifters are used for the suppression of synchrotron sidebands.

In that scheme, each phase shift is chosen such that the total slippage in the drift section corresponds to a phase of $2n\pi$ with respect to the central wavelength, and $(2n'+1)\pi$ with respect to the sideband wavelength. Here n and n' are positive integers.

In our phase jump method, the total slippage in each drift section corresponds to a phase of $2n\pi - \psi_{\mathrm{jump}}$ with respect to the central wavelength. The phase shifts used by Duris *et al.* can therefore be seen as a special case of the phase jump method, where $\psi_{\mathrm{jump}} \equiv 0$.

With $\psi_{\mathrm{jump}} \equiv 0$, the phase shifters do not take part in decelerating the particles. The deceleration relies solely on undulator tapering. As a result, there is no out-of-bucket regime. In general, energy can only be extracted from particles which manage to stay within the rapidly shrinking bucket.

In the simulation study by Duris *et al.*, the value of n ranges from 100 to 330. This means that the slippage introduced by a phase-shifting chicane can be as large as 330 times the optical wavelength. If the chicane is not isochronous, then the large dispersion can significantly degrade the bunching and the trapping.

In our phase jump method, however, the requirement on the isochronism of the chicane is far less stringent, as the method does not rely on large slippage to suppress the synchrotron sidebands. Instead, the method disrupts the synchrotron oscillations by the microbunch deceleration cycles.

In our time-dependent simulation, n is chosen to be as small as possible, and is always less than 20. The smallest possible value of n depends on the length of the drift section and the energy of the electron beam.

Beyond this work, a possible subject of further study is the combined use of taper and phase jumps, such that *both* take part in decelerating the particles, and such that the out-of-bucket regime can be exploited.

VII. CONCLUSION

In this article, we have examined the underlying mechanism of the phase jump method for enhancing the efficiency of an FEL. We have developed a new physics model, and supported it with numerical simulations.

Our model expands beyond previous models by proposing the microbunch deceleration cycle. The model also sets out the selection criteria for the target phase in each phase jump, eliminating the need to deduce the required phase jumps from a pre-optimized undulator taper.

In addition, the model opens up the possibility to extract energy from particles outside the ponderomotive bucket, as well as the possibility to suppress the growth of synchrotron sidebands.

In our time-dependent simulation, the phase jump method yields a lower optical pulse energy at the final saturation than undulator tapering. Nonetheless, the fraction of energy channelled to the sidebands is smaller for the phase jump method than for the taper. As a result, the two techniques yield almost identical spectral power at the central wavelength near the final saturation.

If we define the FEL efficiency in terms of the spectral power at the central wavelength, then the phase jump method is just as efficient as the taper in this case.

[1] H. H. Lu, Y. Li, and J. Pflueger, "The Permanent Magnet Phase Shifter for the European X-Ray Free Electron Laser", Nucl. Instrum. Methods Phys. Res., Sect. A **605**, 399 (2009).

[2] B. Diviacco *et al.*, "Phase Shifters for the FERMI @ Elettra Undulators", in *Proceedings of the 2nd International Particle Accelerator Conference, San Sebastian, Spain* (JACoW, Geneva, Switzerland, 2011), p.3278.

[3] H. G. Lee *et al.*, "Design and Fabrication of Prototype Phase Shifter for PAL XFEL", in *Proceedings of the 4th International Particle Accelerator Conference, Busan, Korea* (JACoW, Geneva, Switzerland, 2013), p.3564.

[4] M. Tischer *et al.*, "Phase Shifters for the FLASH2 FEL", in *Proceedings of the 5th International Particle Accelerator Conference, Dresden, Germany* (JACoW, Geneva, Switzerland, 2014), p.2010.

[5] B. W. J. McNeil *et al.*, "Harmonic Lasing in a Free-Electron-Laser Amplifier", Phys. Rev. Lett. **96**, 084801 (2006).

[6] E. A. Schneidmiller, and M. V. Yurkov, "Harmonic Lasing in X-Ray Free Electron Lasers", Phys. Rev. ST Accel. Beams **15**, 080702 (2012).

[7] N. R. Thompson, and B. W. J. McNeil, "Mode Locking in a Free-Electron Laser Amplifier", Phys. Rev. Lett. **100**, 203901 (2008).

[8] A. A. Varfolomeev, T. V. Yarovoi, and P. V. Bousine, "Possible Enhancement of SASE FEL Output Field Intensity Induced by Local Phase Jump", Nucl. Instrum. Methods Phys. Res., Sect. A **407**, 296 (1998).

[9] D. Ratner, Z. Huang, and A. Chao, "Enhancing FEL Power with Phase Shifters", in *Proceedings of the 29th International Free-Electron Laser Conference, Novosibirsk, Russia* (JACoW, Geneva, Switzerland, 2007), p.69.

[10] N. M. Kroll, P. L. Morton, and M. N. Rosenbluth, "Free-Electron Lasers with Variable Parameter Wigglers", IEEE J. Quantum Electronics **17**, 1436 (1981).

[11] Y. Jiao *et al.*, "Modeling and Multidimensional Optimization of a Tapered Free Electron Laser", Phys. Rev. ST Accel. Beams **15**, 050704 (2012).

[12] A. Mak, F. Curbis, and S. Werin, "Model-Based Optimization of Tapered Free-Electron Lasers", Phys. Rev. ST Accel. Beams **18**, 040702 (2015).

[13] P. Schmüser, M. Dohlus, and J. Rossbach, in *Ultraviolet and Soft X-Ray Free-Electron Lasers: Introduction to Physical Principles, Experimental Results, Technological Challenges* (Springer, Berlin, Germany, 2008), p.29.

[14] J. Wu *et al.*, "X-Ray Spectra and Peak Power Control with iSASE", in *Proceedings of the 4th International Particle Accelerator Conference, Shanghai, China* (JACoW, Geneva, Switzerland, 2013), p.2068.

[15] S. Reiche, "GENESIS 1.3: a Fully 3D Time-Dependent FEL Simulation Code", Nucl. Instrum. Methods Phys. Res., Sect. A **429**, 243 (1999).

[16] N. M. Kroll, and M. N. Rosenbluth, in *Free-Electron Generators of Coherent Radiation*, edited by S. F. Jacobs, H. S. Pilloff, M. Sargent, M. O. Scully, and R. Spitzer (Addison-Wesley, Reading, MA, USA, 1980), p.147.

[17] R. W. Warren, B. E. Newman, and J. C. Goldstein, "Raman Spectra and the Los Alamos Free-Electron Laser", IEEE J. Quantum Electronics **21**, 882 (1985).

[18] D. C. Quimby, J. M. Slater, and J. P. Wilcoxon, "Sideband Suppression in Free-Electron Lasers with Multiple Synchrotron Periods", IEEE J. Quantum Electronics **21**, 979 (1985).

[19] C. Emma, K. Fang, J. Wu, and C. Pellegrini, "High Efficiency, Multiterawatt X-Ray Free Electron Lasers", Phys. Rev. Accel. Beams **19**, 020705 (2016).

[20] J. Duris, A. Murokh, and P. Musumeci, "Tapering Enhanced Stimulated Superradiant Amplification", New J. Phys. **17**, 063036 (2015).

PAPER V

FEL operation modes of the MAX IV Short Pulse Facility

A. Mak, F. Curbis, S. Werin.

Proceedings of FEL 2015, Daejeon, Korea, MOP083.

Proceedings of FEL2015, Daejeon, Korea MOP083

FEL OPERATION MODES OF THE MAX IV SHORT PULSE FACILITY

Alan Mak*, Francesca Curbis, Sverker Werin, MAX IV Laboratory, Lund University, Sweden

Abstract

The Short Pulse Facility (SPF) of the MAX IV Laboratory in Lund, Sweden features the production of ultrashort, incoherent x-ray pulses. It is driven by a 3-GeV linac and comprises two 5-metre undulator modules. While the SPF is designed for spontaneous radiation, we explore alternative operation modes in which the SPF functions as a simple free-electron laser (FEL). In this article, we characterize two of them in time-dependent numerical simulations. We perform a sensitivity study on the electron beam parameters and examine the technique of single-step tapering.

INTRODUCTION

The MAX IV facility in Lund, Sweden includes a Short Pulse Facility (SPF) [1] in addition to two storage rings. Commissioning is in progress as of 2015.

The SPF is situated at the end of the 3-GeV injector (see Fig. 1). It consists of two variable-gap, planar undulator modules, with a length of 5 metres each. The injector provides short electron bunches, which enable the SPF to produce incoherent x-ray pulses as short as 100 fs. From the same injector, electrons are also extracted at 1.5 GeV and 3 GeV for the top-up of the two storage rings (see Fig. 1).

In addition, the MAX IV facility was designed to enable future expansion. Two x-ray FELs (shown in grey in Fig. 1) can potentially be constructed as branch lines parallel to the SPF. They are set out in the long-term strategic plan of the laboratory [2]. In one of the branch lines, an extra linac section is envisaged, so as to provide the FEL with an electron energy of 5 – 6 GeV.

While the SPF is designed for spontaneous radiation, we explore alternative operation modes which enable the observation of coherent gain as a result of self-amplified spontaneous emission (SASE). In these operation modes, the SPF functions as a simple FEL, whereby the necessary techniques for a full-fledged FEL can be developed and tested.

To lay the foundation for future experimental work, we investigate two of such operation modes with the simulation code GENESIS [3]. In the first case, we study the sensitivity of the radiation power to the electron beam parameters. In the second case, we study the technique of single-step tapering [4, 5].

THEORETICAL BACKGROUND

Saturation Length and Power

Many properties of a high-gain FEL are characterized by the dimensionless Pierce parameter, which is defined as [6]

$$\rho = \frac{1}{2\gamma}\left(\frac{I}{I_A}\right)^{1/3}\left(\frac{\lambda_w K f_B}{2\sqrt{2}\pi\sigma_x}\right)^{2/3}. \quad (1)$$

Here γ is the electron beam energy normalized to the electron rest energy $m_e c^2$. I is the peak current. $I_A = m_e c^3/e = 17.045$ kA is the Alfvén current. σ_x is the rms radius of the electron beam. λ_w is the undulator period. K is the undulator parameter. $f_B = J_0(\xi) - J_1(\xi)$ is the Bessel factor for planar undulators, with $\xi = K^2/[2(K^2+2)]$.

Using the Pierce parameter, the saturation length can be estimated by the relation

$$L_{\mathrm{sat}} \approx \frac{\lambda_w}{\rho}, \quad (2)$$

and the saturation power by the relation

$$P_{\mathrm{sat}} \approx \rho P_{\mathrm{beam}}, \quad (3)$$

where $P_{\mathrm{beam}} = \gamma m_e c^2 I/e$ is the electron beam power [6]. According to these relations, L_{sat} decreases with ρ, while P_{sat} increases with ρ.

In the SPF, the total undulator length L_w is only 10 m. In order to observe exponential power growth, it is preferable to choose an operation mode with $L_{\mathrm{sat}} < L_w$, so that the exponential growth regime will, in principle, occur completely within the undulator line.

Single-Step Tapering

The purpose of single-step tapering is to enhance the power, and hence the energy extraction efficiency, of an FEL. It involves the use of two undulator segments with different undulator parameters. While the parameter of the first segment is K, the parameter of the second segment is decreased to $K - \Delta K$. A recent work by Li and Jia [5] provides a theoretical estimate of the optimal ΔK, given by

$$\frac{\Delta K}{K} = 2\sqrt{2}\rho\left(1 + \frac{2}{K^2}\right). \quad (4)$$

According to this relation, the optimal ΔK depends on the Pierce parameter ρ.

OPERATION MODES

We study two selected operation modes of the SPF using the simulation code GENESIS [3] in the time-dependent mode. The main parameters are shown in Table 1.

In Table 1, the saturation length L_{sat} and saturation power P_{sat} are estimated by Eqs. (2) and (3). For case A, the parameters are chosen so that the estimated L_{sat} is slightly shorter than the total undulator length L_w. For case B, the parameters are chosen so that the estimated L_{sat} is within the first of the two undulator modules.

In the simulations, there is a break section of 1 m between the two 5-metre-long undulator modules. As in the real facility, no focusing elements are inserted to the break section. The electron beam size in the SPF can be adjusted only by changing the twiss parameters at the entrance.

* alan.mak@maxlab.lu.se

ISBN 978-3-95450-134-2

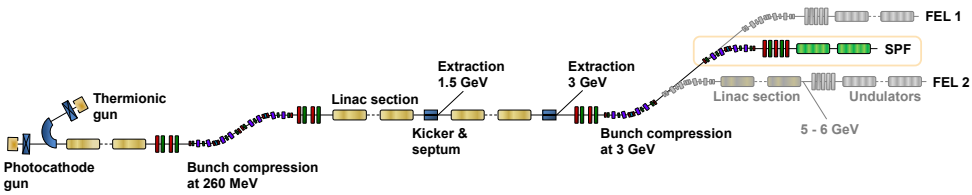

Figure 1: Schematic diagram of the SPF (in highlighted box) and its injector. Two potential FELs foreseen in the long-term strategic plan of the laboratory are shown in grey.

Table 1: Main Parameters of the Two Operation Modes Selected for the Simulation Studies

Parameter	Case A	Case B
Electron beam energy (GeV)	1.8	0.5
RMS bunch length (μm)	8	8
Peak current (kA)	2.5	2.5
Normalized emittance (μm rad)	0.4	0.4
Relative energy spread	1×10^{-4}	1×10^{-4}
Average β function (m)	13	11
Undulator period (mm)	15	15
Undulator parameter K	2.1	1.8
Radiation wavelength (nm)	2	20
Pierce parameter ρ	0.0017	0.0039
Estimated $L_{\rm sat}$ (m)	9	4
Estimated $P_{\rm sat}$ (GW)	7.7	4.8

RESULTS AND DISCUSSIONS

General Results for Case A

The results of the GENESIS time-dependent simulation for case A are summarized in Fig. 2.

Figure 2(a) shows the radiation power as a function of the distance z along the undulator line. Within the first undulator module ($z \leq 5$ m), the radiation does not exhibit any appreciable growth. Exponential growth occurs within the second undulator module ($z = 6 - 11$ m). At the exit of the undulator line ($z = 11$ m), the final power is 2.64 GW. While the estimated saturation length is $L_{\rm sat} = 9$ m, power saturation is not seen within the total undulator length of $L_w = 10$ m.

Figure 2(b) shows the evolution of the beam sizes along the undulator line. The blue and red solid curves correspond to the rms radius of the electron beam in the horizontal and vertical planes, respectively. The green dotted curve corresponds to the rms radius of the optical beam. At $z = 3 - 5$ m, the effect of optical guiding manifests itself in the decrease in optical beam size. In the break section ($z = 5 - 6$ m), the increase in optical beam size is due to vacuum diffraction. In the second undulator module ($z = 6 - 11$ m), the exponential power growth [see Fig. 2(a)] causes strong gain guiding, and hence a rapid decrease in optical beam size. At around $z = 10$ m, the decrease slows down, and the optical beam size approaches a turning point. This reflects the weakening of gain guiding, which is an indication that the radiation power is close to saturation.

Figure 2(c) shows the on-axis field amplitude as a function of z. The field grows monotonically within the undulator modules. In the break section ($z = 5 - 6$ m), there is a small decrease in field amplitude, due to the increase in the optical beam size [see Fig. 2(b)]. At around $z = 10$ m, the growth in field amplitude begins to slow down, as the power is approaching saturation.

Figure 2(d) shows the bunching factor as a function of z. Here the bunching factor is defined as the absolute value of $\langle e^{-i\psi} \rangle$, where the brackets denote the average over all particles, and ψ is the particle phase in the ponderomotive potential. The bunching factor grows with the field amplitude [see Fig. 2(c)], and the growth also begins to slow down at around $z = 10$ m. As the power is approaching saturation, the microbunching is close to fully developed, and the bunching factor reaches 0.35 at $z = 11$ m.

Sensitivity Study on Case A

The emittance, energy spread and peak current listed in Table 1 are stringent requirements on the quality of the electron beam. To quantify the effect of loosening these requirements, we perform a sensitivity study on case A using GENESIS time-dependent simulations. In particular, we probe the reduction in final radiation power (at $z = 11$ m) upon varying the emittance, the energy spread and the peak current, one at a time. The study is summarized in Table 2. The results show that the radiation power is very sensitive to the emittance and the peak current, and is fairly sensitive to the energy spread.

Single-Step Tapering in Case B

Since the SPF is made up of two variable-gap undulator modules, single-step tapering can be implemented by setting the parameters of the first and the second modules to K and $K - \Delta K$, respectively. In case B, the estimated saturation length $L_{\rm sat} = 4$ m is within the first module. By applying a single-step taper, we aim to observe post-saturation power growth in the second module.

The first module is fixed at $K = 1.8$. In GENESIS time-dependent simulations, we vary ΔK and probe the final radiation power at the exit of the second module ($z = 11$ m). The results are summarized in Fig. 3.

ISBN 978-3-95450-134-2

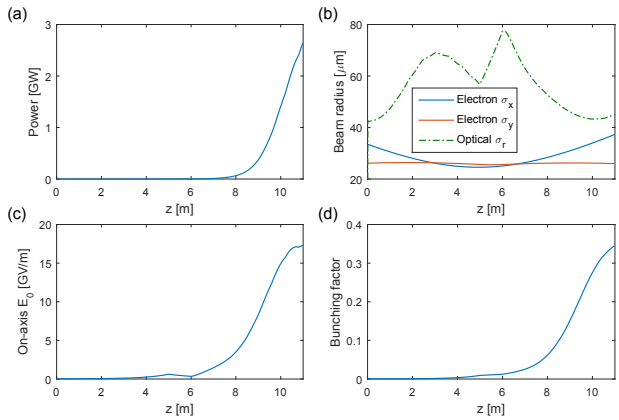

Figure 2: Simulation results for case A. The following quantities are plotted as functions of the distance z along the undulator line: (a) the radiation power; (b) the rms radii of the electron beam (solid curves) and the optical beam (dotted curve); (c) the field amplitude on axis; (d) the bunching factor.

Table 2: Results of the Sensitivity Study on Case A

Normalized emittance (μm rad)	**Final power (GW)**	**Percentage power decrease**
0.4	2.64	-
0.6	0.70	73.6%
0.8	0.13	95.0%
Relative energy spread	**Final power (GW)**	**Percentage power decrease**
1×10^{-4}	2.64	-
3×10^{-4}	1.82	31.3%
5×10^{-4}	1.06	59.9%
Peak current (kA)	**Final power (GW)**	**Percentage power decrease**
2.5	2.64	-
1.8	0.74	72.1%
1.2	0.09	96.7%

Without any tapering ($\Delta K/K = 0$), the final power is 2.58 GW. With single-step tapering, the final power is maximized at $\Delta K/K = 1.4\%$. The maximized final power is 3.51 GW, which is 36% higher than the final power in the no-taper scenario. In comparison, the theoretical estimate of the optimal $\Delta K/K$, given by Eq. (4), is 1.8%.

In Fig. 4, we compare the evolution of various quantities in the simulations of the optimized taper ($\Delta K/K = 1.4\%$) and no taper ($\Delta K/K = 0$).

As seen in Figure 4(a), the radiation power grows exponentially between $z = 3$ m and 5 m. Saturation is reached at the end of the first undulator module ($z = 5$ m), which is a little further than the estimated 4 m. The saturation power is 2.58 GW, which is lower than the estimated 4.8 GW. Without tapering, the power remains at the same level subsequently. With the optimized single-step taper, the power continues to grow after the 1-metre break section, and reaches final saturation at around $z = 7$ m in the second module.

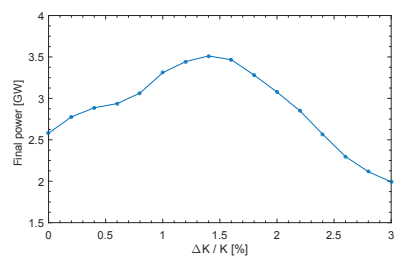

Figure 3: Simulation results for single-step tapering in case B. The final radiation power at the exit of the undulator line is plotted as a function of the step size $\Delta K/K$.

In Figure 4(b), the decrease in optical beam size between $z = 3$ m and 5 m matches the regime of the exponential power growth, due to gain guiding. After the exponential regime, the optical beam size increases again, due to the absence of gain guiding.

In Figure 4(c), the on-axis field amplitude reaches its maximum at $z = 5$ m. Beyond the power saturation, the curve for optimized taper shows an additional bump at $z = 6 - 8$ m over the curve for no taper.

In Figure 4(d), the bunching factor also reaches its maximum at $z = 5$ m. Beyond the power saturation, the optimized taper yields a smaller bunching factor than in the case of no taper. This can be attributed to the detrapping of particles during the deceleration of the ponderomotive bucket in phase space.

ISBN 978-3-95450-134-2

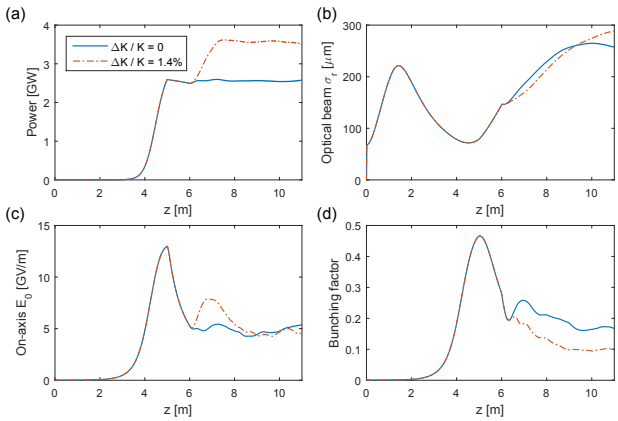

Figure 4: Simulation results for optimized taper ($\Delta K/K = 1.4\%$) and no taper ($\Delta K/K = 0$) in case B. The following quantities are plotted as functions of z: (a) the radiation power; (b) the rms radius of the optical beam; (c) the field amplitude on axis; (d) the bunching factor.

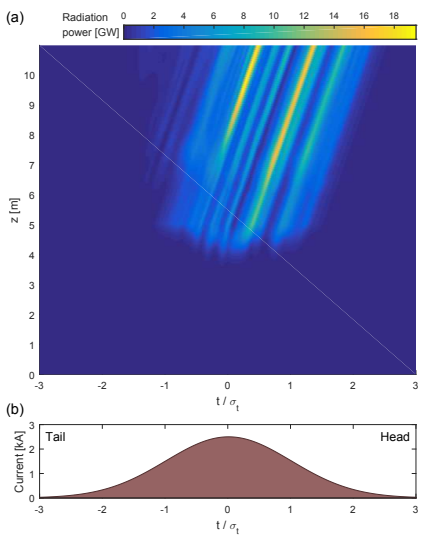

Figure 5: Simulation results for the optimized taper ($\Delta K/K = 1.4\%$) in case B. (a) Radiation power of different slices within the electron bunch. (b) The longitudinal profile of the electron bunch.

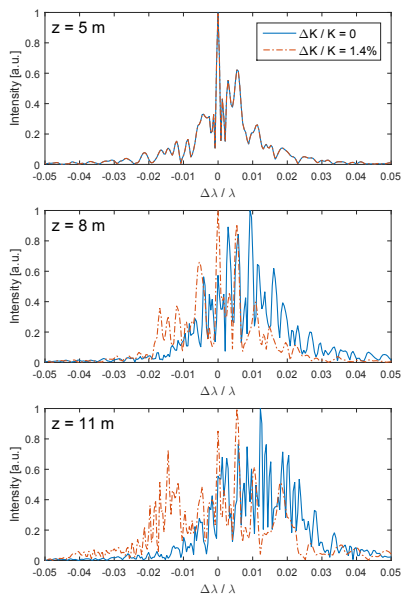

Figure 6: Spectral intensity spectra for optimized taper ($\Delta K/K = 1.4\%$) and no taper ($\Delta K/K = 0$) at $z = 5$ m, 8 m and 11 m.

Radiation Properties of Case B

As the simulations are performed in the time-dependent mode, we can also compare the radiation power at different slices within the electron bunch. This comparison is made in Fig. 5(a) for the case of optimized taper ($\Delta K/K = 1.4\%$). The colour scale shows the radiaion power. The vertical axis shows the distance z along the undulator line. The horizontal axis shows the longitudinal position t within the electron bunch, normalized to the rms bunch length σ_t. Meanwhile, the longitudinal profile of the electron bunch is shown in Fig. 5(b).

ISBN 978-3-95450-134-2

From Fig. 5(a), we see that the radiation is the most intense in the second undulator module ($z = 6-11$ m). Furthermore, it is the central part of the electron bunch ($-\sigma_t \leq t \leq 2\sigma_t$) that contributes significantly to the average radiation power shown in Figure 4(a). Towards the head and the tail of the bunch, the contribution is much smaller.

In Fig. 6, we compare the spectral intensity distributions for the scenarios of optimized taper ($\Delta K/K = 1.4\%$) and no taper ($\Delta K/K = 0$). At $z = 5$ m, the radiation power has just reached saturation, there is very little difference in the two spectral intensity distributions.

Beyond the saturation point, the single-step taper sustains the radiation at the central wavelength, and the central spike is still seen in the spectral intensity distribution at $z = 8$ m and 11 m (see Fig. 6). But in the no-taper scenario, the original resonant condition is no longer maintained after the saturation point. As a result, the radiation power shifts towards longer wavelength in the spectral intensity distributions for $z = 8$ m and 11 m (see Fig. 6).

Another observation in the spectral intensity distribution is the growth of sidebands (see Fig. 6). For the optimized taper, at $z = 11$ m, sidebands are seen around $\Delta\lambda/\lambda = 0.018$ and -0.014. The sideband at $\Delta\lambda/\lambda = 0.005$ even surpasses the central spike in intensity. The growth of the sidebands can be attributed to synchrotron oscillations [7].

CONCLUSION AND OUTLOOK

In this article, we have discussed two operation modes of the SPF, referred to as case A and case B. With the use of time-dependent simulations in GENESIS, we have demonstrated that these operation modes lead to exponential power growth within the length of the undulator line. In these operation modes, the SPF functions as a simple FEL.

In case A, we have performed a sensitivity study, quantifying the effect on the radiation power after loosening the requirements on the quality of the electron beam.

In case B, we have applied the technique of single-step tapering, and compared the optimal step size $\Delta K/K$ obtained in our simulations to that given by theoretical estimation in Li and Jia [5]. With the simulation results, we have examined the radiation properties, which include the evolution of the spectral intensity distribution along the undulator line.

Beyond this article, we envision to test the two FEL operation modes experimentally at the SPF. The experience of operating the SPF as a simple FEL shall provide insight into the laboratory's future development of a full-fledged FEL.

REFERENCES

[1] S. Werin et al., "Short Pulse Facility for MAX-lab", Nucl. Instrum. Methods Phys. Res., Sect. A **601**, 98 (2009).

[2] F. Curbis et al., "Towards an X-Ray FEL at the MAX IV Laboratory", in Proceedings of the 36th International Free-Electron Laser Conference, Basel, Switzerland, 549 (2014).

[3] S. Reiche, "GENESIS 1.3: a Fully 3D Time-Dependent FEL Simulation Code", Nucl. Instrum. Methods Phys. Res., Sect. A **429**, 243 (1999).

[4] D. A. Jaroszynski et al., "Free-Electron Laser Efficiency Enhancement, Gain Enhancement, and Spectral Control Using a Step-Tapered Undulator", Phys. Rev. Lett. **74**, 2224 (1995).

[5] H. Li, Q. Jia., "Optimization of Single-Step Tapering Amplitude and Energy Detuning for High-Gain FELs", Chinese Physics C **39**, 018101 (2015).

[6] Z. Huang, K.-J. Kim, "Review of X-Ray Free-Electron Laser Theory", Phys. Rev. ST Accel. Beams **10**, 034801 (2007).

[7] R. W. Warren, J. C. Goldstein, "The Generation and Suppression of Synchrotron Sidebands", Nucl. Instrum. Methods Phys. Res., Sect. A **272**, 155 (1988).

ISBN 978-3-95450-134-2